



A G H

**AKADEMIA GÓRNICZO-HUTNICZA IM. STANISŁAWA STASZICA W KRAKOWIE
WYDZIAŁ FIZYKI I INFORMATYKI STOSOWANEJ**

KATEDRA ODDZIAŁYWANIA I DETEKCJI CZĄSTEK

Praca dyplomowa

Measurement of the exclusive production of strange particles K_S^0 and Λ^0 in proton-proton diffraction collisions at $\sqrt{s} = 510$ GeV in the STAR experiment at RHIC

Pomiar ekskluzywnej produkcji cząstek dziwnych K_S^0 oraz Λ^0 w zderzeniach dyfrakcyjnych proton-proton przy energii $\sqrt{s} = 510$ GeV w eksperymencie STAR na RHIC

Autor: Patrycja Ada Malinowska
Kierunek studiów: Fizyka Techniczna
Opiekun pracy: prof. dr hab. inż. Mariusz Przybycień

Kraków, 2024

Abstract

At the Relativistic Heavy Ion Collider (RHIC) at Brookhaven National Laboratory (BNL), the beams of protons might collide at the maximum center-of-mass energy $\sqrt{s} = 510$ GeV. These collisions were used in the STAR experiment to study the Central Exclusive Production of strange hadrons. This thesis presents the first results on producing $K_S^0 \bar{K}_S^0$ or $\Lambda^0 \bar{\Lambda}^0$ hadron pairs in proton-proton diffraction. The diffractively scattered forward protons were tagged in the Roman Pot detectors, and the centrally produced pairs of strange hadrons, $K_S^0 \bar{K}_S^0$ or $\Lambda^0 \bar{\Lambda}^0$, were reconstructed in the central detector. The main objective of the analysis was to confirm the possibility of measuring the exclusive production of strange hadrons pairs in diffraction at RHIC and estimate the efficiency of the Time-of-Flight detector. A clear signal of $K_S^0 \bar{K}_S^0$ pairs is observed in the data. Production of $\Lambda^0 \bar{\Lambda}^0$ pairs was also confirmed but with much smaller statistics due to the significantly higher mass of the Λ^0 baryons and lower efficiency of its reconstruction. In addition, the efficiencies of the selection criteria that can be further used in cross-section calculation were determined.

Streszczenie

W Relatywistycznym Zderzaku Ciężkich Jonów (RHIC) w Brookhaven National Laboratory (BNL), wiązki protonów mogą zderzać się przy maksymalnej energii dostępnej w układzie środka masy równej $\sqrt{s} = 510$ GeV. Te zderzenia zostały wykorzystane w eksperymencie STAR do zbadania centralnej ekskluzywnej produkcji dziwnych hadronów. Niniejsza praca dyplomowa przedstawia pierwsze uzyskane rezultaty produkcji par hadronów $K_S^0 \bar{K}_S^0$ lub $\Lambda^0 \bar{\Lambda}^0$ w dyfrakcyjnym oddziaływaniu proton-proton. Dyfrakcyjnie rozproszone protony były zarejestrowane przez detektory Roman Post, a centralnie wyprodukowane pary $K_S^0 \bar{K}_S^0$ lub $\Lambda^0 \bar{\Lambda}^0$ zostały zrekonstruowane przez detektory centralne eksperymentu STAR. Głównym celem analizy jest potwierdzenie możliwości pomiaru ekskluzywnej centralnej produkcji par dziwnych hadronów w procesie dyfrakcji przy energiach dostępnych na akceleratorze RHIC i oszacowanie wydajności detektora czasu przelotu. Wyraźny sygnał produkcji par $K_S^0 \bar{K}_S^0$ jest obserwowany w danych. Produkcja par $\Lambda^0 \bar{\Lambda}^0$ została również potwierdzona ale z mniejszą statystyką wynikającą ze znacznie większej masy barionu Λ^0 i mniejszej wydajności jego rekonstrukcji. Ponadto zostały wyznaczone wydajności kryteriów selekcji, które w przyszłości mogą zostać wykorzystane do policzenia przekroju czynnego.

Acknowledgments

I sincerely thank my supervisor, Prof. Mariusz Przybycień, for the knowledge provided during our collaboration. I want to thank you for your time, discussions and guidance provided, which resulted in this thesis. Your thoroughness and meticulousness have influenced my work ethic and will remain with me in my future academic career. Your enthusiasm and assistance in understanding the various aspects of particle physics have been an important element in my decision on my future path, for which I thank you again. I would also like to thank Dr Leszek Adamczyk, who always found time to explain the analysis I conducted. Your knowledge and experience were invaluable. Thank you for your patience and valuable guidance, which helped me to develop my research skills and understand the complexity of the analysis in the experiment. I would also like to thank my loved ones for their support throughout my thesis.

Podziękowania

Pragnę serdecznie podziękować mojemu promotorowi, prof. Mariuszowi Przybycienniowi za przekazaną wiedzę podczas naszej współpracy. Dziękuję za poświęcony czas, przeprowadzone dyskusje i udzielone wskazówki, co zaowocowało niniejszą pracą magisterską. Pańska rzetelność i skrupulatność wpłynęły na moją etykę pracy i pozostaną ze mną w dalszej karierze naukowej. Pański entuzjazm i pomoc w zrozumieniu różnych aspektów fizyki cząstek elementarnych stanowiły dla mnie ważny elementem w podjęciu decyzji dotyczącej dalszej ścieżki, za co jeszcze raz dziękuję. Pragnę również podziękować dr. Leszkowi Adamczykowi który zawsze znalazł czas na udzielenie wyjaśnień dotyczących prowadzonej analizy. Pańska wiedza i doświadczenie były nieocenione. Dziękuję za cierpliwość i cenne wskazówki, które pomogły mi rozwinąć umiejętności badawcze i zrozumieć złożoność analizy w eksperymencie. Dziękuję również moim najbliższym za okazane wsparcie w trakcie realizacji pracy magisterskiej.

Contents

0 Wstęp	3
1 Theoretical Introduction	4
1.1 Standard Model	4
1.2 Diffractive Physics	6
1.3 Event kinematics	7
1.4 Luminosity and cross section	9
1.5 Monte Carlo simulation	10
1.6 Motivation of the $K_S^0\bar{K}_S^0$ and $\Lambda^0\bar{\Lambda}^0$ measurements	10
2 The Experimental Setup	12
2.1 The Relativistic Heavy Ion Collider	12
2.2 The STAR experiment	13
2.3 The Time Projection Chamber	13
2.4 The Time-Of-Flight detector	15
2.5 Zero degree calorimeter and beam-beam counter	16
2.6 The Roman-Pot System	16
3 Data Analysis and Results	19
3.1 Event Selection for the $K_S^0\bar{K}_S^0$ production	19
3.2 Selection criteria efficiency	32
3.3 Time-of-flight detector efficiency	36
3.4 Physics results for the $K_S^0\bar{K}_S^0$ pair production	51
3.5 The $\Lambda^0\bar{\Lambda}^0$ pair production	54
4 Summary	57
References	58

0 Wstęp

W maju 2023 roku rozpoczęłam działalność naukową w międzynarodowej współpracy eksperymentu STAR w grupie AGH. Moja praca skupiała się na przeprowadzeniu analizy oddziaływań dyfrakcyjnych proton-proton dla energii w układzie środka masy $\sqrt{s} = 510$ GeV. Badanym procesem dyfrakcyjnym była centralna ekskluzywna produkcja par mezonów $K_S^0 \bar{K}_S^0$ oraz par barionów $\Lambda^0 \bar{\Lambda}^0$ poprzez mechanizm wymiany dwóch pomeronów (ang. double-Pomeron exchange). W procesie przygotowawczym zapoznałam się z zasadą działania detektora oraz metodą rekonstrukcji śladów pozostawianych przez naładowane cząstki. Zapoznałam się także ze strukturą danych w eksperymencie STAR oraz nauczyłam się korzystać z klas służących do pisania programu do analizy danych w języku C++ w środowisku ROOT. W trakcie pracy nad analizą miałam również możliwość wstępnego zaznajomienia się z teorią Reggego opisującej dyfrakcyjną fizykę. Od maja 2023 postępy pracy, dyskusje oraz pomysły na dalszy rozwój analizy były regularnie dyskutowane na cotygodniowych spotkaniach grupy AGH oraz na zdalnych spotkaniach z grupą z Politechniki Czeskiej w Pradze (CTU) z którą grupa krakowska bliżej współpracuje w zakresie analizy produkcji cząstek dziwnych w eksperymencie STAR. Postępy mojej pracy prezentowałam także na zebraniach Współpracy STAR:

- STAR Collaboration meeting at American University of Cairo, Egypt, 16–20 października 2023.
- STAR Collaboration meeting at Brookhaven National Laboratory, USA, 18–22 marca 2024,
- STAR Collaboration regional meeting in Prague, Czech Republic, 27-29 maja 2024.

Udział w tych spotkaniach nie tylko pozwolił mi na podzielenie się rezultatami mojej pracy, ale również dał mi możliwość doskonalenia wystąpień publicznych dla międzynarodowej publiczności oraz pozwolił na zapoznanie się z analizami prowadzonymi przez innych członków Współpracy STAR.

Poza wcześniejszej wspomnianą pracą nad centralną ekskluzywną produkcją, przeprowadziłam również analizę wydajności detektora pomiaru czasu przelotu (ang. time-of-flight). Analiza ta zwiększyła moją wiedzę na temat metod wykorzystywanych do tego typu badań, jak również pokazała mi jak ważne jest dokładne zrozumienie rzeczywistego zachowania poszczególnych detektorów w celu uzyskania poprawnych końcowych wyników fizycznych. Owoce mojej pracy są programy komputerowe do analizy danych napisane w C++ które mogą być wykorzystywane i rozwijane także przez inne osoby. Uzyskane przeze mnie wyniki są przedstawione i podsumowane w niniejszej pracy magisterskiej.

1 Theoretical Introduction

1.1 Standard Model

The Standard Model (SM) of particle physics describes the fundamental constituents of matter and their interactions [1, 2]. The twelve matter particles, called fermions, are spin-half particles. The fermions are subdivided into leptons and quarks, with integer and fractional electric charges, respectively. Fermions are grouped into three generations. The first generation consists of *up* and *down* quarks and *electron* and *electron neutrino*, which make up the low energy level of the Universe. The high-energy physics experiments revealed the second and the third generation of fundamental particles, which have the same properties as the first-generation particles but with higher masses. Every fermion particle has its corresponding antiparticle with the same mass and lifetime but an opposite electric charge and magnetic moment. The interactions between fermions are described in terms of particle exchange called bosons. Contrary to fermions, bosons have integer spin. The SM describes three fundamental forces: weak, electromagnetic, and strong. Those forces are described in the modern approach by the Quantum Field Theories. All twelve fermions undergo weak interactions, subject to the exchange of the Z , W^+ , or W^- bosons. The nine fermions with an electric charge undergo electromagnetic interactions by exchanging the photon γ . Quarks are the only fermions that experience strong interaction mediated by gluons g . The Higgs boson is the last element of the SM that was discovered in 2012. The Higgs boson is the 0-spin scalar particle that determines the mechanics of mass acquired by other particles. The summary of the particle content of SM is shown in Fig. 1.

three generations of matter (fermions)			three generations of antimatter (antifermions)			interactions / forces (bosons)	
	I	II	III	I	II	III	
mass charge spin	$\simeq 2.2 \text{ MeV}$ $+2/3$ $1/2$ u up	$\simeq 1.3 \text{ GeV}$ $+2/3$ $1/2$ c charm	$\simeq 173 \text{ GeV}$ $+2/3$ $1/2$ t top	$\simeq 2.2 \text{ MeV}$ $-2/3$ $1/2$ ū antiup	$\simeq 1.3 \text{ GeV}$ $-2/3$ $1/2$ c̄ anticharm	$\simeq 173 \text{ GeV}$ $-2/3$ $1/2$ t̄ antitop	0 0 1 g gluon
QUARKS	$\simeq 4.7 \text{ MeV}$ $-1/3$ $1/2$ d down	$\simeq 96 \text{ MeV}$ $-1/3$ $1/2$ s strange	$\simeq 4.2 \text{ GeV}$ $-1/3$ $1/2$ b bottom	$\simeq 4.7 \text{ MeV}$ $+1/3$ $1/2$ d̄ antidown	$\simeq 96 \text{ MeV}$ $+1/3$ $1/2$ s̄ antistrange	$\simeq 4.2 \text{ GeV}$ $+1/3$ $1/2$ b̄ antibottom	0 0 1 γ photon
LEPTONS	$\simeq 0.511 \text{ MeV}$ -1 $1/2$ e electron	$\simeq 106 \text{ MeV}$ -1 $1/2$ μ muon	$\simeq 1.777 \text{ GeV}$ -1 $1/2$ τ tau	$\simeq 0.511 \text{ MeV}$ $+1$ $1/2$ e positron	$\simeq 106 \text{ MeV}$ $+1$ $1/2$ μ antimuon	$\simeq 1.777 \text{ GeV}$ $+1$ $1/2$ τ antitau	$\simeq 91.2 \text{ GeV}$ 0 1 Z Z boson
	$< 1.0 \text{ eV}$ 0 $1/2$ ν electron neutrino	$< 0.17 \text{ eV}$ 0 $1/2$ ν muon neutrino	$< 18.2 \text{ MeV}$ 0 $1/2$ ν tau neutrino	$< 1.0 \text{ eV}$ 0 $1/2$ ν electron antineutrino	$< 0.17 \text{ eV}$ 0 $1/2$ ν muon antineutrino	$< 18.2 \text{ MeV}$ 0 $1/2$ ν tau antineutrino	$\simeq 80.4 \text{ GeV}$ -1 1 W W boson
							$\simeq 80.4 \text{ GeV}$ $+1$ 1 W W boson
							SCALAR BOSONS
							GAUGE BOSONS
							VECTOR BOSONS

Figure 1: Particle content of the Standard Model. The quarks and leptons are divided into three generations of matter and antimatter. Also, the gauge bosons responsible for their interactions and the Higgs boson are shown. Figure taken from [3].

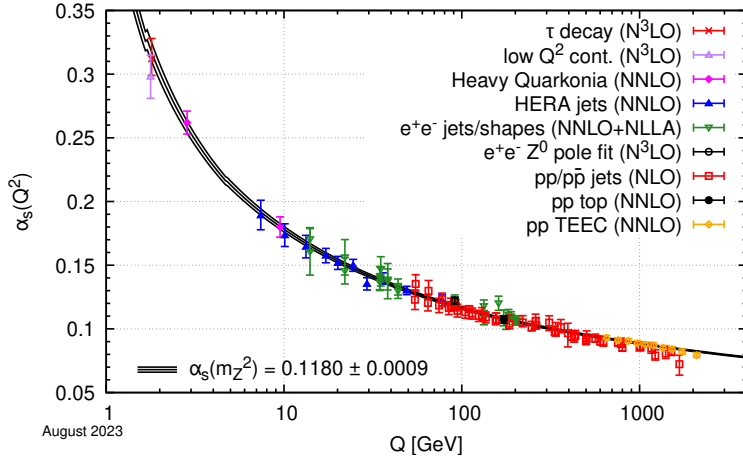


Figure 2: Summary of measurements of α_s as a function of the energy scale Q compared to the running of the coupling. Figure taken from [6].

The Quantum Field Theory describing the strong interaction between the quarks and gluons is called Quantum Chromodynamics (QCD) [4,5]. The strong interactions occur solely between quarks and gluons. The gluons are electrically neutral and massless bosons with $J = 1^-$ spin-parity and mediate the strong force. The QCD distinguishes three colour charges subjected to the interaction: red, green, blue, and their anti-colours. Quarks carry one of the following colour charges, and anti-quarks carry anti-colours. Gluons carry colour and anti-colour charge. This feature of gluons carrying colour charge allows them to interact strongly also with each other and is responsible for the peculiar effects of QCD. There are eight independent gluon states. The QCD quark-antiquark potential V_s as a function of distance r is expressed by:

$$V_s(r) = -\frac{4}{3} \frac{\alpha_s}{r} + kr \quad (1)$$

where α_s is the strong coupling constant and $k \approx 1$ GeV/fm. A recent summary of the measurements of α_s as a function of energy scale is shown in Fig. 2. This running coupling constant is of the order of unity at $Q \approx \Lambda_{\text{QCD}} = 200 - 300$ MeV, making applying perturbative QCD at low momentum transfers impossible. On the other hand, at high energy scales (Q of the order of few GeV), $\alpha_s \ll 1$ and in this regime, the perturbative methods in QCD can be applied. The first term in Eq. (1) comes from the single-gluon exchange and dominates at small distances. The second term expresses the hypothesis of colour confinement, the theoretical explanation for the lack of observation of free quarks at large scales. The bound state of the quarks and anti-quarks are called hadrons. Hadrons are subdivided based on the number of the valence quarks:

- mesons - built up from a quark-antiquark pair.
- baryons - built up from three quarks states.

It should be noted that more exotic states of hadronic matter, like tetraquarks or pentaquarks, have also recently been confirmed experimentally.

1.2 Diffractive Physics

The hadronic interactions can be subdivided into soft and hard processes [7, 8]. The soft processes energy scale is of the order of the hadron size $R \sim 1$ fm. The four-momentum transfer t is proportional to the inverse of the squared R , $|t| \sim 1/R^2$. The differential cross-section as a function of t is given by exponential dependency $d\sigma/dt \sim e^{-R^2|t|}$. For low values of $|t|$, perturbative QCD does not apply to the description of those processes. On the contrary, the perturbative QCD can describe the hard processes. For the hard processes, we can distinguish two energy scales. The first, like for the soft processes, is of the order hadron size, and the other is for large transfer momentum greater than ~ 1 GeV. The relation between the cross-section and the momentum transfer is logarithmic or powerlike.

The hadronic diffraction is a process defined as a reaction without exchanging the quantum numbers between colliding particles at high energies. Diffractive processes are characterized by a large rapidity gap between the diffractively scattered beam particles and the produced final state. It is convenient to describe diffraction processes within the traditional framework of Regge theory, which was developed before QCD. High-energy interactions are described in terms of an object known as the Reggeon. For diffraction, that object is colourless and holds the quantum numbers of the vacuum. That object is called the Pomeron. In perturbative QCD, the Pomeron can be approximated as a pair of oppositely coloured gluons. Diffractive-like $p+p$ processes can be further subdivided into distinct classes:

- Elastic scattering - both incident particles remain intact after the collision:

$$p + p \rightarrow p' + p' \quad (2)$$

- Single diffractive dissociation - one of the incident particles remains intact, while the other dissociates in a low mass system:

$$p + p \rightarrow X + p' \quad (3)$$

- Double diffractive dissociation - both of the incoming particles dissociate into low mass systems:

$$p + p \rightarrow X + Y \quad (4)$$

- Double Pomeron exchange with central production - both protons remain intact after the interaction. As a result of the Pomeron-Pomeron interaction, a final state is produced at the central values of the pseudorapidity:

$$p + p \rightarrow p' + X + p' \quad (5)$$

The above-described processes are depicted in Fig. 3. From left to right, elastic scattering, single diffraction dissociation (SDD), double diffraction dissociation (DDD), and double Pomeron exchange (DPE) with central production are shown.

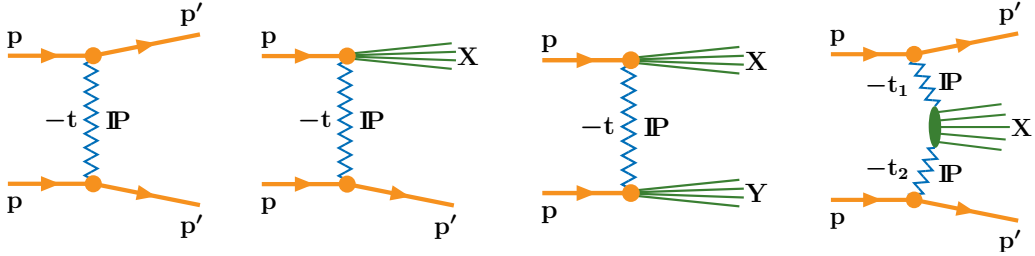


Figure 3: The Feynman diagrams of diffractive processes in proton-proton collisions. From left: elastic scattering, single diffraction dissociation, double diffraction dissociation, double Pomeron exchange with central production.

1.3 Event kinematics

This section presents the main kinematic variables used to describe the CEP of $K_S^0 \bar{K}_S^0$ and $\Lambda^0 \bar{\Lambda}^0$ pairs in STAR. STAR uses a right-handed coordinate system with the origin at the nominal interaction point (IP) in the centre of the detector and the z -axis along the beam pipe. The x -axis points from the IP to the outside of the RHIC ring, and the y -axis points upward. Cylindrical coordinates (r, φ) are used in the transverse plane, φ being the azimuthal angle around the beam pipe. Let us denote the initial state four-momenta of the incoming protons by $P^i = [E^i, p_x^i, p_y^i, p_z^i]$, where $i = E, W$ denote the side of the incident protons: East (negative z) and West (positive z) side of the STAR detector, respectively. The energy available in the centre-of-mass system for the production of the new final-state particles is given by the squared root of the relativistic invariant s defined as:

$$s = (P^E + P^W)^2 = (E^E + E^W)^2 - (\vec{p}^E + \vec{p}^W)^2 \quad (6)$$

In the case of head-on proton collisions, cosine between proton's momenta in Eq. (6) equals -1 . Additionally, considering that for a highly relativistic particle of mass m , the conditions $|\vec{p}| \gg m$ and $E \approx |\vec{p}|$ are satisfied, we obtain:

$$s = 4E^E E^W \quad (7)$$

In the CEP process, the final-state system consists of two intact protons with four momenta $P'^i = [E'^i, p_x'^i, p_y'^i, p_z'^i]$, where $i = E, W$, and a pair of hadrons, which may be produced in a resonant or non-resonant way (see Fig. 5).

We define the relative losses of energy of diffractively scattered beam protons as:

$$\xi^i = \frac{E^i - E'^i}{E^i}, \quad i = E, W \quad (8)$$

Other kinematical observables needed to describe the intact protons are the four-momenta transfers squared at the proton vertices:

$$t^i = (P^i - P'^i)^2, \quad i = E, W \quad (9)$$

The laboratory reference system is also the center-of-mass system for counter-rotating proton beams of equal energy. Therefore, both beam protons have energy $\sqrt{s}/2$, and using Eq. (8) one can express the energy of the centrally produced pair as:

$$E^{\text{pair}} = (\xi^E + \xi^W) \frac{\sqrt{s}}{2} \quad (10)$$

Additionally, neglecting the scattered protons' transverse momenta (compared to the longitudinal ones), the longitudinal momentum of the pair can be approximated by:

$$p_z^{\text{pair}} \approx (\xi^E - \xi^W) \frac{\sqrt{s}}{2} \quad (11)$$

Equations (10) and (11) allow us to express the invariant mass of the pair using the relative energy losses of the beam protons:

$$(m^{\text{pair}})^2 \approx (E^{\text{pair}})^2 - (p_z^{\text{pair}})^2 = s \xi^E \xi^W \quad (12)$$

In the case of resonant production, the energy, momentum, and mass of the pair given by Eqs. (10),(11),(12) also refer to a resonance decaying into the observed pair, and therefore relevant quantities will be denoted below also with an index \mathcal{R} .

In High Energy Physics (HEP), a commonly used quantity is rapidity, y , as its difference between two frames of references is invariant under Lorentz transformation along the beamlime, i.e. z -coordinate. The rapidity of a particle with four-momentum $P = [E, p_x, p_y, p_z]$ is defined as:

$$y = \frac{1}{2} \ln\left(\frac{E + p_z}{E - p_z}\right) \quad (13)$$

Let us compare the rapidity in the prime (boosted) and non-prime (laboratory) frames of reference:

$$\begin{aligned} y' &= \frac{1}{2} \ln \left[\frac{E' + p'_z}{E' - p'_z} \right] = \frac{1}{2} \ln \left[\frac{\gamma(E - \beta p_z) + \gamma(p_z - \beta E)}{\gamma(E - \beta p_z) - \gamma(p_z - \beta E)} \right] \\ &= \frac{1}{2} \ln \left[\frac{E + p_z}{E - p_z} \right] + \frac{1}{2} \ln \left[\frac{1 - \beta}{1 + \beta} \right] = y + \frac{1}{2} \ln \left[\frac{1 - \beta}{1 + \beta} \right] \end{aligned} \quad (14)$$

As one can see, the difference, $y' - y$, is constant and depends only on the two frames' relative velocity, β . For a highly energetic particle, we apply relativistic approximation and express the z -component of the momentum as $p_z = E \cos(\theta)$, where θ is the polar angle. The Eq. (13) can be then approximated with pseudorapidity, η :

$$y \approx \eta = -\ln\left(\tan\frac{\theta}{2}\right) \quad (15)$$

In the CEP process, the rapidity of a resonance (or of a pair of particles it decays into) can be expressed in terms of relative energy losses of forward-scattered protons by substituting Eqs. (10) and (11) into Eq. (13):

$$y_{\mathcal{R}} = \frac{1}{2} \ln\left(\frac{\xi^E}{\xi^W}\right) \quad (16)$$

By solving the system of Eqs. (12) and (16) for ξ^E and ξ^W , we can express the relative energy losses of protons in terms of invariant mass and rapidity of the centrally produced resonance particle:

$$\xi^E = \frac{m_{\mathcal{R}}^2}{\sqrt{s}} e^{-y_{\mathcal{R}}}, \quad \xi^W = \frac{m_{\mathcal{R}}^2}{\sqrt{s}} e^{y_{\mathcal{R}}} \quad (17)$$

Simultaneous measurement of the centrally produced hadron pair and intact beam protons constitute an over-constrained system and enable using Eqs. (12), (16), and (17) for checking kinematic correlations that can help in identifying the signal of interest. STAR experiment allows for such an over-constrained measurement using the central detector and the Roman Pot system (see Sec. 2.6).

1.4 Luminosity and cross section

The centre-of-mass energy \sqrt{s} introduced in the previous chapter provides information on the ability to produce heavy particles in a collision and depends on the colliding particles' energies. Another essential characteristic of a particle collider is its instantaneous luminosity \mathcal{L} , which provides information on the collision rate [2]. The particles in a beam are grouped into bunches. Assuming the normal distribution of the particles in a bunch, the instantaneous luminosity is expressed by the equation:

$$\mathcal{L} = f \frac{n_1 n_2}{4\pi\sigma_x\sigma_y} \quad (18)$$

where f is the collision frequency, n_1 and n_2 are the numbers of the particles in the colliding bunches, σ_x and σ_y are root-mean-square sizes of the bunch in the horizontal and vertical directions. The integral of the instantaneous luminosity over time gives total luminosity L_{tot} :

$$L_{\text{tot}} = \int \mathcal{L}(t) dt \quad (19)$$

The cross-section, σ , measures the underlying quantum mechanical probability of the interaction. The cross-section is expressed in area units and can be seen as the effective cross-sectional area related to the target particle. The derivation of this concept for the bunches moving head-on can be done following Fig. 4. Let the flux

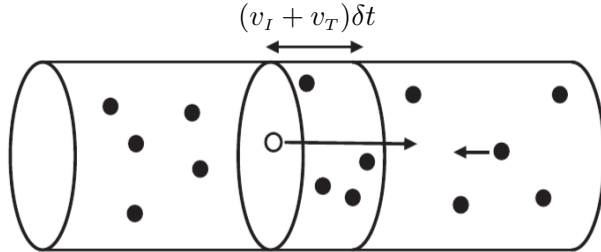


Figure 4: General scheme used for cross-section calculation. Figure adapted from [2].

of the incident particles I be Φ_I . The flux Φ_I expresses the number of the particles I passing the unit area in unit time. The cross-section σ relates the flux of the incident particles with interaction rate r with target particles T :

$$r = \sigma\Phi_I \quad (20)$$

Let us assume that the transverse cross-section area of the bunch is A . Let v_I and v_T denote the velocities of particles I and T . The relative velocity of particles I and T is $v = v_I + v_T$. In infinitesimal time δt , the particle I passes the volume with $\delta N_T = n_T v A \delta t$ target particles, where n_T is the volume density of target particles. If the effective area size of the target particles is σ , then interaction probability dP can be calculated as the:

$$\delta P = \frac{\delta N \sigma}{A} = \frac{n_T A v \sigma \delta t}{A} = n_T v \sigma \delta t \quad (21)$$

Thus, the collision rate:

$$r_I = \frac{\delta P}{\delta t} = n_T v \sigma \quad (22)$$

The total interaction can be expressed the Φ_I :

$$r = r_I N_I = r_I n_I V = \Phi N_T \sigma \quad (23)$$

where Φ is the flux of the incident particles, which accounts for the relative motion.

The number of the observed events N is related to the cross-section. And total luminosity by the following formula:

$$N = \sigma \cdot L_{\text{tot}} \quad (24)$$

1.5 Monte Carlo simulation

In the analysis for the $K_S^0 \bar{K}_S^0$ pairs production, Monte Carlo (MC) samples obtained from the Dime MC event generator [9, 10] were used. The Dime MC is a Fortran-based class that implements unweighted events of the central exclusive meson production via a double-Pomeron exchange mechanism. We use both the true- and the detector-level MC. The true-level events from the Dime MC that underwent the STAR detector simulation with the GEANT3 framework [11] were embedded in the real data samples to resemble the experimental effects observed in the real data, which would be challenging to simulate otherwise. Such embedded MC samples were reconstructed in the same as the real data. The information added to the true level after the detector simulation and reconstruction step is called the detector-level MC. Due to the lack of the simulation of RP detectors' responses in the current analysis, the true values of the scattered protons' momenta were blurred by adding the Gaussian noise based on the previous studies of the STAR experiment.

At the time of writing this thesis, there was no MC available for the CEP of baryon pairs.

1.6 Motivation of the $K_S^0 \bar{K}_S^0$ and $\Lambda^0 \bar{\Lambda}^0$ measurements

Production and decay of the long-lived K_S^0 and Λ^0 particles to two charged hadrons can be used to study fragmentation models of strange quarks that are important for modelling underlying-event dynamics. In recent years, a number of the measurements of the K_S^0 and Λ^0 production was conducted in e^+e^- collisions at LEP [12–16], in ep collisions at HERA [17–20], at $p\bar{p}$ collisions at CDF [21] and in pp and heavy ion collisions at RHIC [22–24] and the LHC [25–30] collider experiments as well as at fixed target experiments e.g. at NA61/SHINE [31]. However, there are no measurements of those particles in diffractive processes. This work addresses the lack of measurements in the energy range attained by the RHIC collider and measured in the STAR experiment.

The CEP can be subdivided into exclusive non-resonant and resonant production, as well as inclusive production. Those processes are illustrated in the diagrams in Fig. 5. This work focuses on the CEP processes. In Quantum Mechanics, one has to square the sum of amplitudes for the processes with identical initial and final states to calculate a cross-section. These amplitudes can be complex and, therefore, interfere positively or negatively. In the case of the study performed in this thesis, these concern resonant and non-resonant production diagrams. In particular, many different resonances decaying, respectively, into $K_S^0 \bar{K}_S^0$ or $\Lambda^0 \bar{\Lambda}^0$ pairs can contribute to the observed cross-section at the amplitude level.

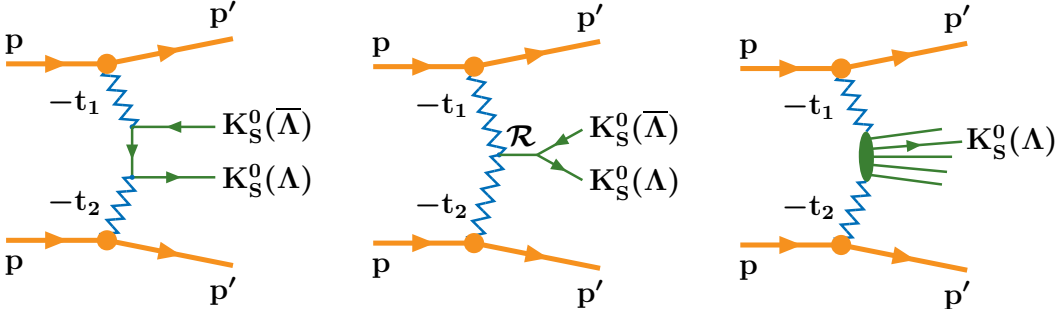


Figure 5: (left) Non-resonant and (middle) resonant mechanisms of CEP of $K_S^0\bar{K}_S^0$ and $\Lambda^0\bar{\Lambda}^0$ pairs. (right) Central inclusive production of K_S^0 and Λ^0 hadrons.

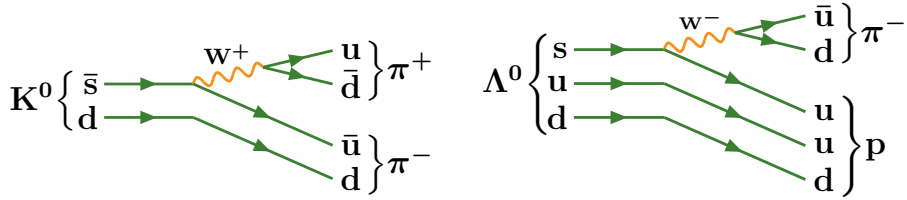


Figure 6: Schematic views of the most probable (with highest branching ratios) decay channels of K_S^0 and Λ^0 .

The K_S^0 and Λ^0 hadrons are neutral and can be observed only by measuring their decay into charged daughter particles. K_S^0 particle consists of the anti-strange and down quarks, while Λ^0 from the strange, up, and down valence quarks. The decay schemes are presented in Fig. 6. Approximately 69.2% of the K_S^0 mesons decay into the oppositely charged pions $K_S^0 \rightarrow \pi^+ + \pi^-$, while 63.9% of Λ^0 baryons decay into a proton and pion $\Lambda^0 \rightarrow p + \pi^-$ [6]. Both decays proceed via weak interaction (W boson exchange), the only interaction that does not conserve the flavour quantum number. It is worth mentioning their mean lifetimes to get some impression about the distances between the production and decay vertices of K_S^0 and Λ^0 particles. They are equal $\tau = 0.895 \times 10^{-10}$ s (corresponding to $c\tau = 2.68$ cm) and $\tau = 2.63 \times 10^{-10}$ s (corresponding to $c\tau = 7.89$ cm), for the K_S^0 and Λ^0 , respectively.

2 The Experimental Setup

2.1 The Relativistic Heavy Ion Collider

The Relativistic Heavy Ion Collider (RHIC) [32–34] is the second largest collider in the world with a circumference of 3.8 km, located at Brookhaven National Laboratory (BNL) in New York State. The uniqueness of the collider lies in the possibility of colliding two polarized proton beams or a polarized proton beam with a heavy ion beam. The overview of the RHIC complex is shown in Fig. 7. The accelerator chain comprises six major components: Electron Beam Ion Source (EBIS), Linear Accelerator (LINAC), Booster, Alternating Gradient Synchrotron (AGS), transfer beamline AtR, and the RHIC collider. The proton particles come from the hydrogen ions produced in the Optically Pumped Polarized H⁻ Ion Source (OPPIS). Hydrogen ions are accelerated in a LINAC and strip injected to the Booster [35]. The RHIC collider has six interaction points whose positions are determined based on the clock description. The northmost interaction point marks noon. The clockwise direction is defined in the eastern direction from the northmost interaction point. Two collider rings are labelled "Blue" and "Yellow" for the clockwise and counter-clockwise beams. Rings consist of six arcs of length approximately equal to 356 m with eleven FODO (Focus-Drift-Defocus-Drift) cells, with a modified half-cell at the ends. The FODO cell has two dipole magnets 9.45 m long and two composite units, each with a 0.75 m long sextupole, 1.11 m long quadrupole, and 0.50 m long corrector assembly. The total number of superconducting magnets equals 1740. The beams in a given arc are separated by 90 cm in the horizontal plane. The *DX* and *D0* dipoles direct the beam to the head-on collision in the centre of the 277 m long intersections. The *DX* and *D0* magnets are approximately 10 m and 23 m from the IPs. The final focus is done with three quadrupole magnets. The RHIC collider can accelerate different species of ions within a range of atomic masses from $A = 1$ (proton) to $A = 200$ (gold). The maximum possible centre-of-mass energy in proton-proton collisions can reach $\sqrt{s} = 510$ GeV and 200 GeV per nucleon pair in gold-gold collisions. The

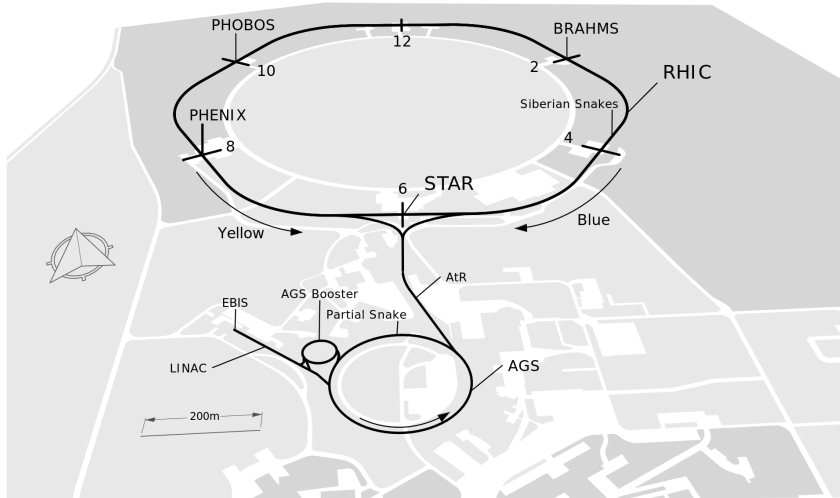


Figure 7: The general scheme of the RHIC complex. Figure taken from [55].

instantaneous luminosity are equal to: $2.5 \cdot 10^{31} \text{ cm}^{-2}\text{s}^{-1}$ and $1.4 \cdot 10^{31} \text{ cm}^2\text{s}^{-1}$ for gold-gold and proton-proton collisions, respectively.

2.2 The STAR experiment

The main scope of the RHIC facility is the investigation of the quark-gluon plasma formation and its properties. The Solenoidal Tracker at RHIC (STAR) experiment is one of the four heavy-ion physics experiments that started in 1999 [33, 36, 37]. Today, the only other active experiment is sPHENIX, the successor of the PHENIX experiment. The STAR detector is located at 6 o'clock of the RHIC collider [38]. The overview of the STAR detector is shown in Fig. 8.

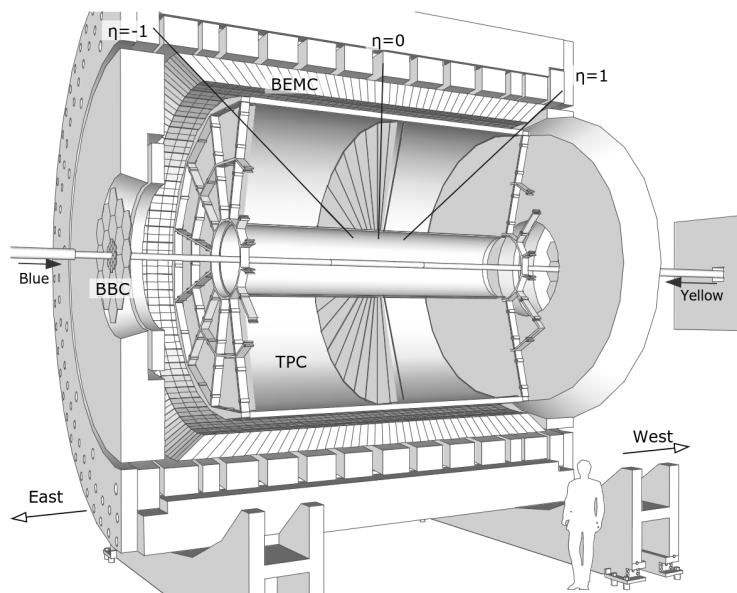


Figure 8: The overview on the STAR detector. Figure taken from [55].

In the analysis of the STAR data presented in this thesis, mainly three subdetectors were used: Time Projection Chamber (TPC), Time-Of-Flight detector (TOF), and Roman Pot (RP) system. Zero-degree calorimeter (ZDC) and Beam Beam Counter (BBC) detectors were used to trigger the CEP events. A detailed description of these detectors is presented in the following sections. The experiment [39] is run by the STAR Collaboration, which currently consists of 74 institutions from 15 countries, with a total of 756 people involved.

2.3 The Time Projection Chamber

The STAR TPC [40] is the core of the experiment. It is the primary tracking device for momentum measurement and particle identification based on the Bethe-Bloch energy loss dE/dx . The middle high-voltage conductive Central Membrane (CM) marks the origin of the STAR left-handed coordinate system, with the y -coordinate pointing upward and the x -pointing outside, near which collisions occur - the interaction point (IP). The CM is set at a potential -28 kV , together with concentric field cage cylinders (outer (OFC) and inner (IFC) field cages), and grounded readout

caps provide a uniform electric field of approximately 135 V/cm. The 10% methane in argon mixture is used for particle detection, with a pressure held at 2 mbar above atmospheric pressure. The measured momentum spectrum ranges from 100 MeV/ c to 30 GeV/ c , while particle identification reaches above 1 GeV/ c . The TPC operates in a 0.5 T magnetic field, provided by a solenoidal magnet surrounding the detector, parallel to the electric field. The cross-section circumference of the cylindrical detector is equal to 4 m, and the length is 4.2 m, which enables the detection of the particles within the pseudorapidity region from -1.8 to 1.8 and full azimuthal angle.

The electrons produced in primary ionization flow toward the read-out system built from the Multi-Wire Proportional Chambers (MWPCs) with read-out pads arranged in rows in twelve sectors. Within the vicinity of the anode wires, electrons experience a strong electric field that causes an electron avalanche that amplifies the signal by a factor of 1000 to 3000. Produced ions induce an image charge on the pads that fades away as ions move away from the anode wires. A preamplifier/shaper/waveform digitizer system measures an induced signal. The image charge shared by multiple pads enables the reconstruction of the original position.

The charge measured on adjacent pads with a signal in a given row determines the cluster's x and y positions. The drift time of the secondary electron from the origin to the endcap and an average drift velocity determine the z -position of the cluster. The tracks in an event are reconstructed with the Kalman Filter approach [41]. The algorithm differentiates between global, primary, and secondary tracks. The primary tracks emerge from the main collision vertex, while secondary tracks are the decay products resulting from the interaction of the primary tracks. The tracks are called global when they are fitted in the first pass of the algorithm without a vertex. In this thesis, only global tracks are used.

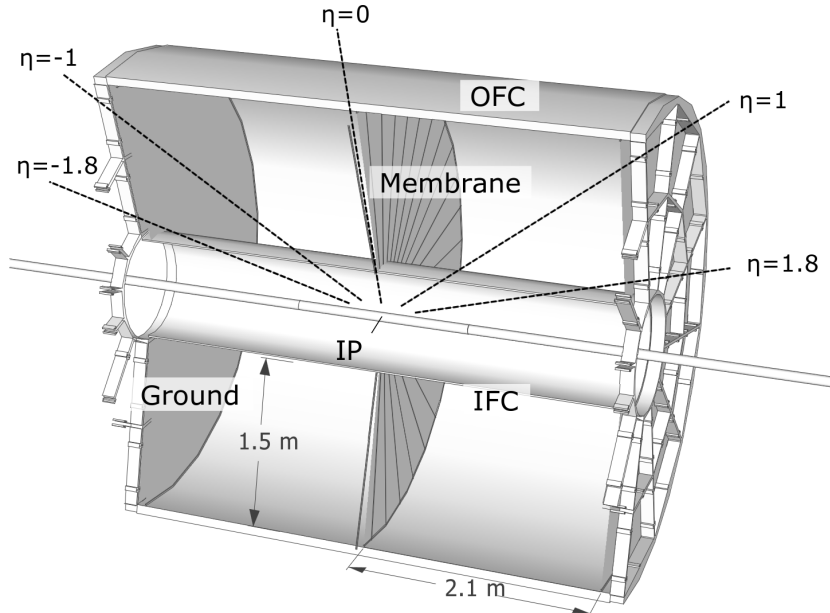


Figure 9: The STAR Time Projection Chamber. Figure adapted from [55].

2.4 The Time-Of-Flight detector

The TPC enables the identification of pions and kaons with momenta lower than approximately $0.7 \text{ GeV}/c$ and protons with momenta up to $1.0 \text{ GeV}/c$ [42–46]. This covers around 70% of the produced charged hadrons in an event. The Time-Of-Flight (TOF) detector was designed and employed in the STAR experiment to overcome this limitation and enhance particle identification. In principle, the TOF detector provides precise time measurement based on the multi-gap resistive plate chambers (MRPCs) technology. MRPC module consists of alternate layers of the glass and gaps filled with feron-butane gas with external graphite electrodes. The applied high voltage between electrodes creates an electric field in each gas gap, which produces a Townsend avalanche when a charged particle passes through. The electrodes, with glass layers as the resistive material, are transparent to the charges generated during this process. The copper read-out pads detect the induced signal from the summation of avalanches created in each gas gap. The TOF detector is built up from 3840 MRPC modules located equally on the 120 trays surrounding the TPC detector (Fig. 10). The Vertex Position Detectors (VPDs) are the scintillator detectors used to determine the collision start time. Those detectors are placed close to the beamline within $\sim 5.7 \text{ m}$ from the centre of the STAR detector on the west and east sides. The start time T_0 is set to:

$$T_0 = (T_E + T_W)/2 - L/c. \quad (25)$$

where T_E and T_W are the times measured by the east and west detector, L is the distance between them, and c is the speed of light. The particle stop time T_s is measured with the TOF detector. We can identify particles by combining the information on the time from TOF and track length from the TPC detector. That measurement extends the $\pi/K/p$ identification to $\sim 1.8 \text{ GeV}$. In CEP, the time measurement with the VPD detector is not applicable as it requires the dissociation remnants of the proton.

In contrast, in CEP, the protons remain intact. Instead of determining the particle type, in the CEP processes, an assumption of the same type of tracks is made, which

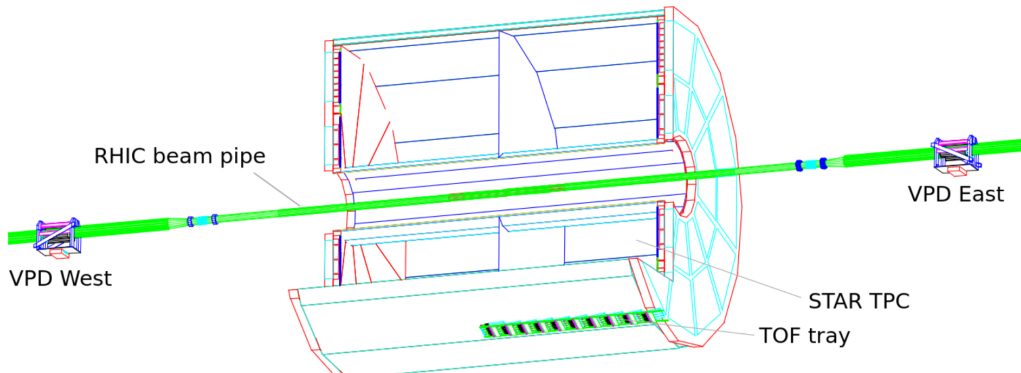


Figure 10: Schematic view of the STAR TOF detector placed outside the TPC. Figure taken from [55].

enables the determination of the particle time by measuring the time difference of the hits and the length of the helical path [55]. The TOF hit is assigned to the TPC track if the extrapolated track matches the hit position.

2.5 Zero degree calorimeter and beam-beam counter

A Zero-Degree Calorimeter (ZDC) and Beam-Beam Counter (BBC) are used as the vertex detector for triggering events [47]. The primary purpose of the ZDC is to measure neutron energy deposited in the lead-fiber calorimeter via measurement of the Cherenkov radiation. By measuring the neutron's energy, the multiplicity of the event can be inferred. ZDC covers the pseudorapidity region $|\eta| > 6.0$. The BBC counter is used as the minimum-bias trigger in $p+p$ collisions. The BBCs cover the pseudorapidity region $2.2 < |\eta| < 5.0$. The BBC is segmented into 18 inner small tiles and 18 outer large tiles, shown in Fig. 11.

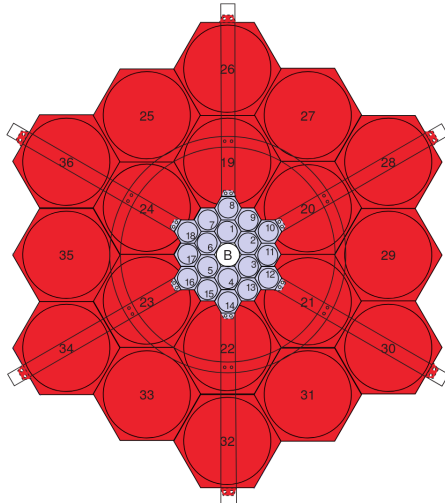


Figure 11: Schematic of the BBC tiles. Figure taken from [55].

2.6 The Roman-Pot System

Apart from the four heavy-ion physics experiments at RHIC, PP2PP was launched in 2003 to measure scattered protons at $\sqrt{s} = 50 - 500$ GeV [48, 49]. The detection system uses silicon (Si) detectors housed in cylindrical movable Roman Pot (RP) vessels. These vessels separate the silicon detectors from the vacuum in the accelerator tube and allow them to be placed up to 15 mm from the beamline. Each RP vessel contains four silicon strip detectors (SSDs) placed alternately in the directions of the x and y . The scintillation detector is placed behind each RP station's Si planes and used as an event trigger.

In 2008, the detection system of the PP2PP was integrated into the STAR experiment, which enabled tagging forward protons. The system's layout, as implemented in the STAR experiment, is shown in Fig. 12. The eight RP stations are placed symmetrically around the IP, below and above the beamline, between dipole magnets DX and $D0$, within an absolute distance of 15.8 m and 17.6 m from the IP. The

naming convention indicates branch: E or W - east or west side of the detector, 1 or 2 - near or far station, U or D - station placed above or below the beamline.

The reconstruction of the RP proton tracks starts with forming the set of strips with the ADC counts above the threshold [50–54]. The ADC counts represent deposited energy in a strip. The adjacent strips with signals above the threshold level are merged into the cluster. A cluster is characterized by the length (number of adjacent strips), total deposited energy, and position that is calculated as the weighted average of the positions of the strips in a cluster, with the weight being energy deposited in a strip. The clusters are matched between the detector planes of the same strip orientation in an RP station by finding the smallest distance between the clusters that do not exceed the length of twice the Si detector strip pitch. If two clusters are matched, the clusters form a hit with the positions calculated as the arithmetic average of the clusters' positions in corresponding planes. In the case of lack of matching, hits correspond to single clusters.

The high-level representations of the signal in the strips of the RP detectors are RP track points and tracks (Fig. 13). The RP track point is an averaged hit between x and y orientations, with assigned x , y , and z positions. If there is more than one hit per detector plane with the same strip orientation, all possible combinations are calculated, meaning that a given RP station can have assigned more than one RP track point. The RP track represents a scattered proton and has assigned complete information on its kinematics. There are two classes of tracks: global and local. Global RP tracks are reconstructed from all possible combinations of the RP track points in near and far stations. In contrast, the local ones are reconstructed within only one station if there is no information in another station. In the following analysis, only global tracks are used.

The momentum reconstruction for the global RP tracks is based on the measurement of the angles between near and far stations θ_x^{RP} and θ_y^{RP} for x and y components, and bending of the proton trajectory in the uniform magnetic field of the DX magnet of length l_{DX} :

$$\theta_x^{\text{RP}} = \frac{x_2 - x_1}{l_{\text{RP}}} \quad \theta_y^{\text{RP}} = \frac{y_2 - y_1}{l_{\text{RP}}} \quad (26)$$

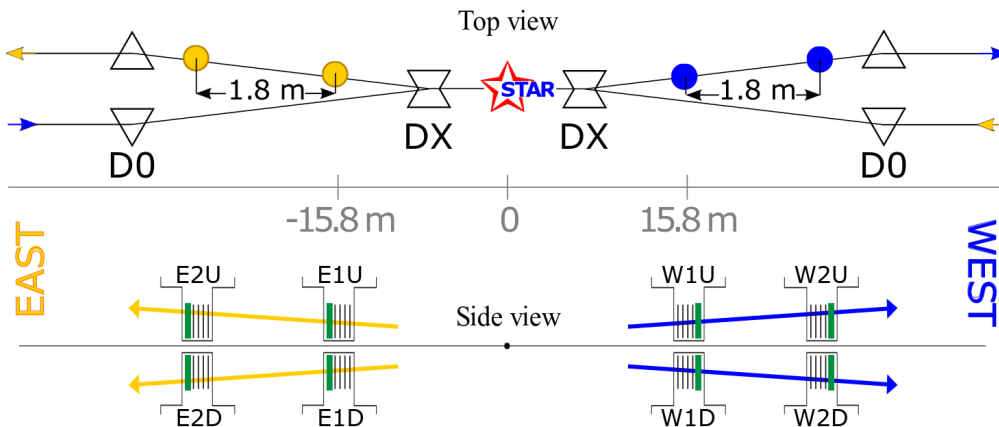


Figure 12: The layout of the Roman Pot system in the STAR experiment in top and side views. Figure taken from [55].

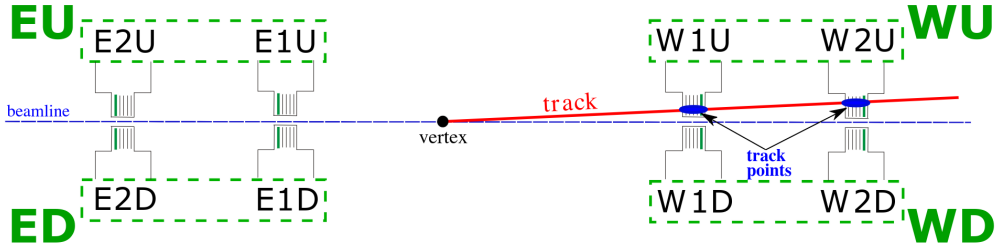


Figure 13: The RP system layout with illustrated RP track and RP track point. Figure taken from [55].

where (x_1, y_1) and (x_2, y_2) are the positions of the RP track points in near and far stations, respectively, and l_{RP} is the distance between those stations. The scattering angle to the beamline can be calculated in the x -direction as:

$$\theta_x = \frac{x_1 - x_{\text{IP}} - (d_2 + \frac{1}{2}l_{\text{DX}})\theta_x^{\text{RP}}}{d_1 - z_{\text{IP}} + \frac{1}{2}l_{\text{DX}}} \quad (27)$$

and similarly for θ_y . The relative loss of the proton's energy, ξ , can be obtained from:

$$\xi = \left(1 + \frac{\alpha_0(d_1 + \frac{1}{2}l_{\text{DX}} - z_{\text{IP}})}{\theta_x^{\text{RP}}(d_1 + l_{\text{DX}} + d_2 - z_{\text{IP}}) - x_1 + x_{\text{IP}}} \right)^{-1} \quad (28)$$

where $x_{\text{IP}}, y_{\text{IP}}, z_{\text{IP}}$ are the coordinates of the interaction point (IP), d_1 is the distance from the centre of the detector to the near face of the DX magnet, and d_2 is the distance between the DX magnet end and beginning of the near RP station. Full derivation of the θ_x and θ_y , and ξ can be found in Ref. [55].

3 Data Analysis and Results

3.1 Event Selection for the $K_S^0 \bar{K}_S^0$ production

The analyzed data come from proton-proton collisions at $\sqrt{s} = 510$ GeV and were collected in 2017 by the STAR experiment at RHIC (Run 17). This section outlines the selection criteria (SC) employed in the analysis and explains their importance in selecting a centrally produced state of the strange hadron pairs. Below are listed all the selection criteria for the $K_S^0 \bar{K}_S^0$ pair production:

1. CEP triggers: CPT2 and CPT2noBBCL.
2. Exactly two RP tracks, one on the west and one on the east side of the IP, of good quality and within the fiducial region:
 - 2.1 at least three out of four planes used for the RP track point reconstruction,
 - 2.2 $0.4 < |p_y| < 0.8$ GeV, $p_x > -0.27$ GeV, $(p_x + 0.6)^2 + p_y^2 < 1.25$ GeV 2 where p_x and p_y are the transverse components of the protons momenta.
3. Four tracks that are taken into consideration to form a $K_S^0 \bar{K}_S^0$ pair must fulfil the following requirements:
 - 3.1 total charge is equal to zero,
 - 3.2 pseudorapidity range is $|\eta| \leq 0.9$,
 - 3.3 transverse momentum $p_T \geq 0.2$ GeV,
 - 3.4 number of hits used for the track reconstruction $N_{\text{fit}}^{\text{hit}} \geq 20$.
4. Exclusive event selection:
 - 4.1 narrow mass window for kaon candidate: $0.48 \leq m_{\pi^+\pi^-} \leq 0.52$ GeV,
 - 4.2 missing transverse momentum $p_T^{\text{miss}} \leq 0.15$ GeV,
 - 4.3 number of TOF clusters: $N_{\text{TOF}}^{\text{cluster}} \leq 2 \cdot N_{\text{TOF}}^{\text{tracks}} + 1$.
5. Geometrical cuts on the tracks forming a K_S^0 candidate:
 - 5.1 distance of the closest approach between the kaon trajectory and the beamline DCA_{beamline} ≤ 2.5 (1.5) cm for kaon formed from two (one) TOF-matched tracks,
 - 5.2 distance of the closest approach between pions: DCA_{daughters} ≤ 2.5 (1.5) cm for kaon formed from two (one) TOF-matched tracks,
 - 5.3 decay length l_{decay} and pointing angle α_p of a kaon candidate fulfill the following requirements:
 - $l_{\text{decay}} \leq 3.0$ cm or $\cos(\alpha_p) \geq 0.925$ for kaons formed from two TPC tracks matched with the TOF detector,
 - $\cos(\alpha_p) \geq 0.95$ for kaons formed from one TPC track matched with the TOF detector.
6. Removing accidental overlap with elastic events (mainly due to pile-up). The definition of the elastic event is following:

- $|p_x^E + p_x^W| < 0.1$ GeV
- $|p_y^E + p_y^W| < 0.1$ GeV
- $|\xi^E| < 0.007$
- $|\xi^W| < 0.007$

If at least one of the above criteria is not fulfilled, the event is accepted as a candidate for the CEP process.

7. Selection cuts making use of the kinematic correlations between centrally produced system and intact protons:

- 7.1 $|m_{KK}/\sqrt{s} - \sqrt{\xi^W \xi^E}| \leq 0.004$
- 7.2 $|y_{KK} - 1/2 \ln(\xi^E/\xi^W)| \leq 0.9$
- 7.3 $|m_{KK}/\sqrt{s} e^{y_{KK}} - \xi^W| \leq 0.004$ and $|m_{KK}/\sqrt{s} e^{-y_{KK}} - \xi^E| \leq 0.004$.

8. Decay vertices positions of the kaon candidates:

- 8.1 average position of the z coordinate of the kaon decay vertices $(vtx_z^{\text{leading}} + vtx_z^{\text{subleading}})/2 \leq 80.0$ cm
- 8.2 distance between decay vertices of the kaons in z direction $|vtx_z^{\text{leading}} - vtx_z^{\text{subleading}}| \leq 15.0$ cm.

9. Angle between pions momenta in the rest frame of the parent K_S^0 candidate $|\cos(\theta^*)| \leq 0.8$.

The analysis is based on the events triggered by the Central Production Triggers: CPT2 and CPT2noBBCL. The trigger logic is defined on the trigger bits named after RP branches: EU, ED, WU, and WD [55]. The bit is set to one if at least one of the four photomultipliers in a branch gives a signal. For the event with two protons, one on the west and one on the east side of the detector, we differentiate between diagonal and anti-diagonal configurations of the protons. In terms of the bits, the diagonal configuration is expressed as $(\text{EU}\&\&\text{WD})||(\text{ED}\&\&\text{WU})$, and anti-diagonal is expressed as $(\text{EU}\&\&\text{WU})||(\text{ED}\&\&\text{WD})$. CPT2 trigger uses either diagonal or anti-diagonal configuration to prevent pile-up events. Furthermore, the CPT2 trigger requires the absence of a hit in the small tiles of the BBC and a lack of a hit in the ZDC detectors on both the west and east sides. In addition, the CPT2 trigger ensures the presence of the hits in the TOF detector. The CPT2noBBCL trigger includes a veto on events with a detected hit in large BBC tiles.

Figure 14 presents the distribution of the trigger signals in the data. The CPT2 triggers are labeled 570701 and 570705, while CPT2noBBCL is labeled 570711. Those triggers constitute the highest fraction of all the trigger signals in the events. There are several other triggers used for different purposes.

The main characteristic of the CEP processes is the presence of intact beam particles scattered into small angles in opposite directions. This is a result of momentum conservation. In the analysis, the presence of two protons is obtained by imposing conditions on exactly two RP tracks, one on the east and one on the west sides of the STAR detector. Figure 15 presents the distribution of the RP branches where RP tracks were reconstructed. As discussed in Sec. 2.6, the RP stations are placed

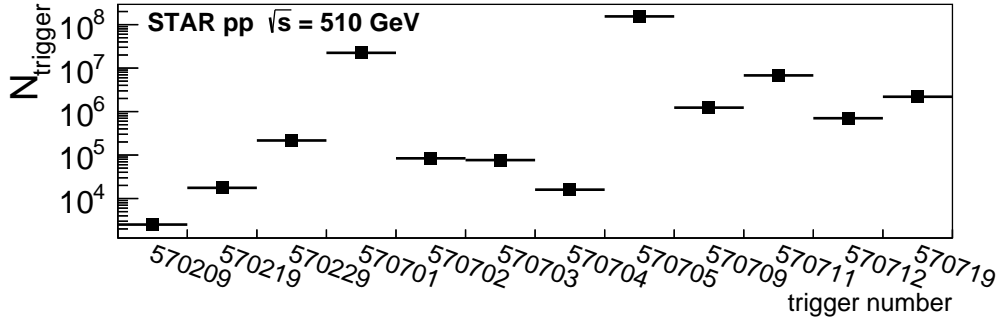


Figure 14: Distribution of the trigger signals in the data from p+p collisions at $\sqrt{s} = 510$ GeV in Run 17. CPT2 triggers are labelled 570701 and 570705, while CPT2noBBCL is labelled 570711.

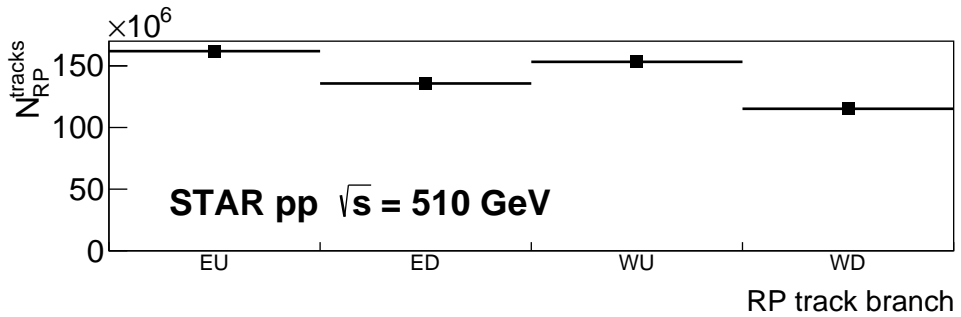


Figure 15: Distribution of the number of the RP tracks reconstructed in a given RP branch. The designations of the RP branch are EU (east up), ED (east down), WU (west up), and WD (west down). For CEP, we demand two RP tracks, one on the west and one on the east.

symmetrically below and above the beamline. The designations of the RP branches are EU (east up), ED (east down), WU (west up), and WD (west down).

The quality condition is also imposed on the RP track point to increase confidence that RP tracks come from intact protons. It requires at least three of the four silicon planes used for the RP track point reconstruction in a given RP station. Figure 16 presents the distribution of the number of planes used for the track point reconstruction. Most RP track points are reconstructed from at least three Si-planes.

Figure 17 presents the two-dimensional distribution of the transverse momenta of the protons measured by the RP detectors. The p_x and p_y components of the transverse momenta were approximated based on the measured angles θ_x and θ_y , assuming that the longitudinal proton momentum is the same before and after the collision:

$$\begin{aligned} p_x &\approx p_z \cdot \theta_x \\ p_y &\approx p_z \cdot \theta_y. \end{aligned} \tag{29}$$

where $p_z = 254.867$ GeV is the momentum of the incoming beam proton in the z direction at the centre of the mass-energy equals $\sqrt{s} = 510$ GeV. The area defined in SC 2.2 employing the p_x and p_y encloses the fiducial region, which is the region

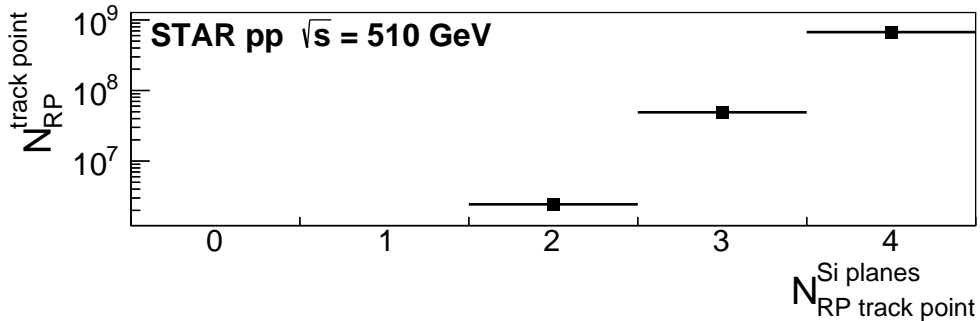


Figure 16: Distribution of the number of silicon planes used for the RP track point reconstruction. We demand at least three planes to form a high-quality RP track representing an intact proton.

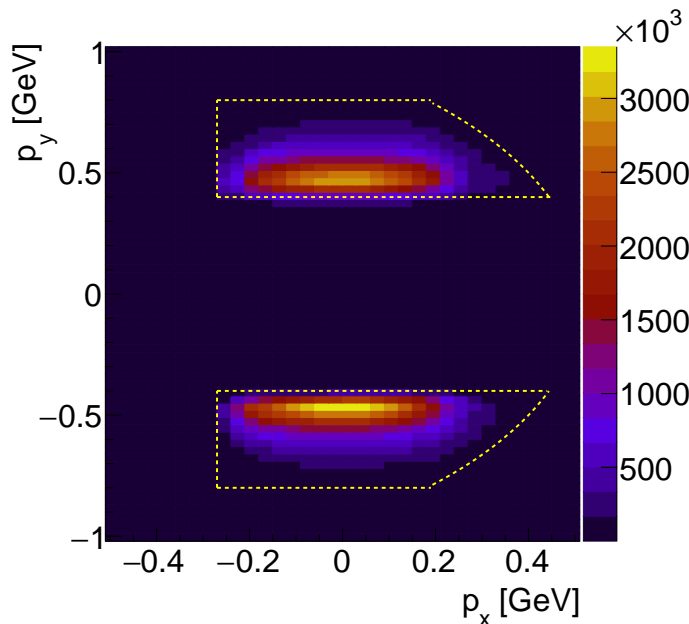


Figure 17: Distribution of the reconstructed transverse momenta of the protons. The yellow dashed line indicates the fiducial region defined by SC 2.2.

of the highest proton detection efficiency in RP detectors, is also drawn in Fig. 17.

The selection criteria SC 1 and SC 2 are crucial in CEP. Therefore, they were applied at the pre-selection stage of the data analysis. In addition, the pre-selected data contain only events with at least two global tracks matched with the TOF detector, as we want the kaon to be formed from at least one TPC track matched with a hit in TOF. From that point, the figures are presented based on the pre-selected data.

Figure 18 presents the distributions of the number of global tracks N^{tracks} in the events. The tracks were divided into two groups: matched and not matched with the TOF detector. The analysis was performed for four cases of the number of global

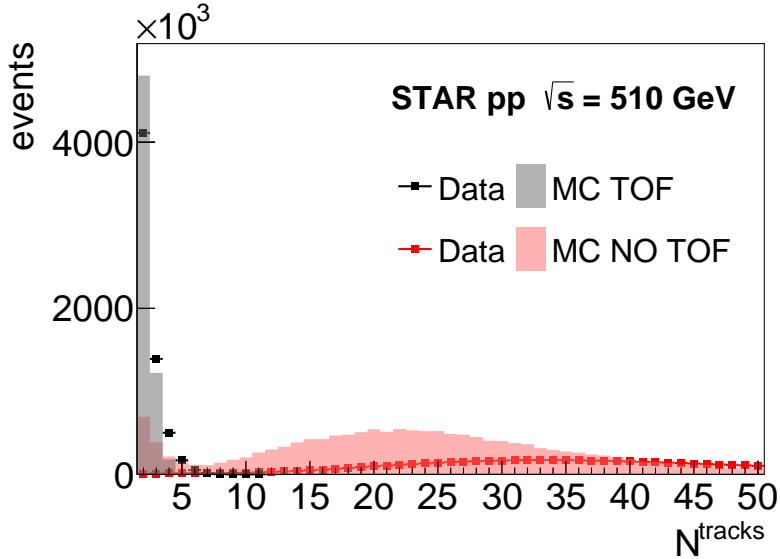


Figure 18: Distribution of the number of global tracks N^{tracks} with the division for tracks matched and not matched with TOF detector. The MC is scaled by the ratio of the number of entries in the data histogram with TOF hits to the number of corresponding entries in the MC histogram. The ratio is equal to 396.9 ± 3.2 .

tracks matched with TOF in an event: $N_{\text{TOF}}^{\text{tracks}} = 2, 3, 4$, and 5 . Our “golden” case is $N_{\text{TOF}}^{\text{tracks}} = 4$. However, to increase the statistics, we consider the TOF detector’s limited efficiency ($N_{\text{TOF}}^{\text{tracks}} = 2$ or 3) or erroneous attribution of a hit to the global track by the matching algorithm ($N_{\text{TOF}}^{\text{tracks}} = 5$). The MC is scaled by the ratio of the number of entries in the data histogram with TOF hits to the number of entries in the MC histogram. The ratio is equal to 396.9 ± 3.2 .

The quality of the global tracks is determined by the transverse momentum p_T , pseudorapidity η , and the number of hits used for the track reconstruction $N_{\text{fit}}^{\text{hit}}$, which are presented in Fig. 19. The distributions are shown separately for each $N_{\text{TOF}}^{\text{tracks}}$ considered and for tracks matched and not matched with the TOF detector. For $p_T < 0.2$ GeV, we can observe a significant drop in the number of events for TOF-matched tracks. Most tracks matched with the TOF detector are within the pseudorapidity range $|\eta| < 0.9$. Due to the STAR detector acceptance restrictions, the tracks must have $p_T > 0.2$ GeV and $|\eta| < 0.9$. The same requirements are put on tracks that are not matched with a TOF hit. The minimum number of hits used for the track reconstruction of both types was chosen to be 20. Each MC histogram was scaled by the ratio of the number of events with $N_{\text{TOF}}^{\text{tracks}} = 4$ in data to the corresponding number in MC. This ratio equals 83.6 ± 1.1 .

A selection criterion on the minimum number of high-quality tracks of the appropriate charge was imposed to form a kaon candidate. All global tracks are assumed to represent pions. For $N_{\text{TOF}}^{\text{tracks}} = 4$, if the event has four high-quality global tracks matched with TOF, their total charge must equal zero. If one of the TOF-matched global tracks does not fulfil one of the good quality requirements (SC 3) - the event is processed as in the case of $N_{\text{TOF}}^{\text{tracks}} = 3$. For the events with $N_{\text{TOF}}^{\text{tracks}} = 3$, if there are three high-quality tracks matched with TOF of the total charge equal to ± 1 , the

event must have at least one high-quality track not matched with TOF of charge equal to ∓ 1 . If the total charge of the TOF-matched tracks equals ± 3 , the event is dismissed. For the case where the event has two high-quality tracks with TOF hit $N_{\text{TOF}}^{\text{tracks}} = 2$, at least one TOF-matched track must be assigned to each kaon candidate. This means that the total charge of high-quality tracks matched with TOF equals $-2, 2$, or 0 . To be a candidate for a CEP of a $K_S^0 \bar{K}_S^0$ pair, the event must contain at least two high-quality tracks that are not matched with TOF, of total charge equal to $2, -2$, and 0 , respectively. In the case of $N_{\text{TOF}}^{\text{tracks}} = 5$, if there are one or two low-quality TOF tracks, the event is processed as the event with four or

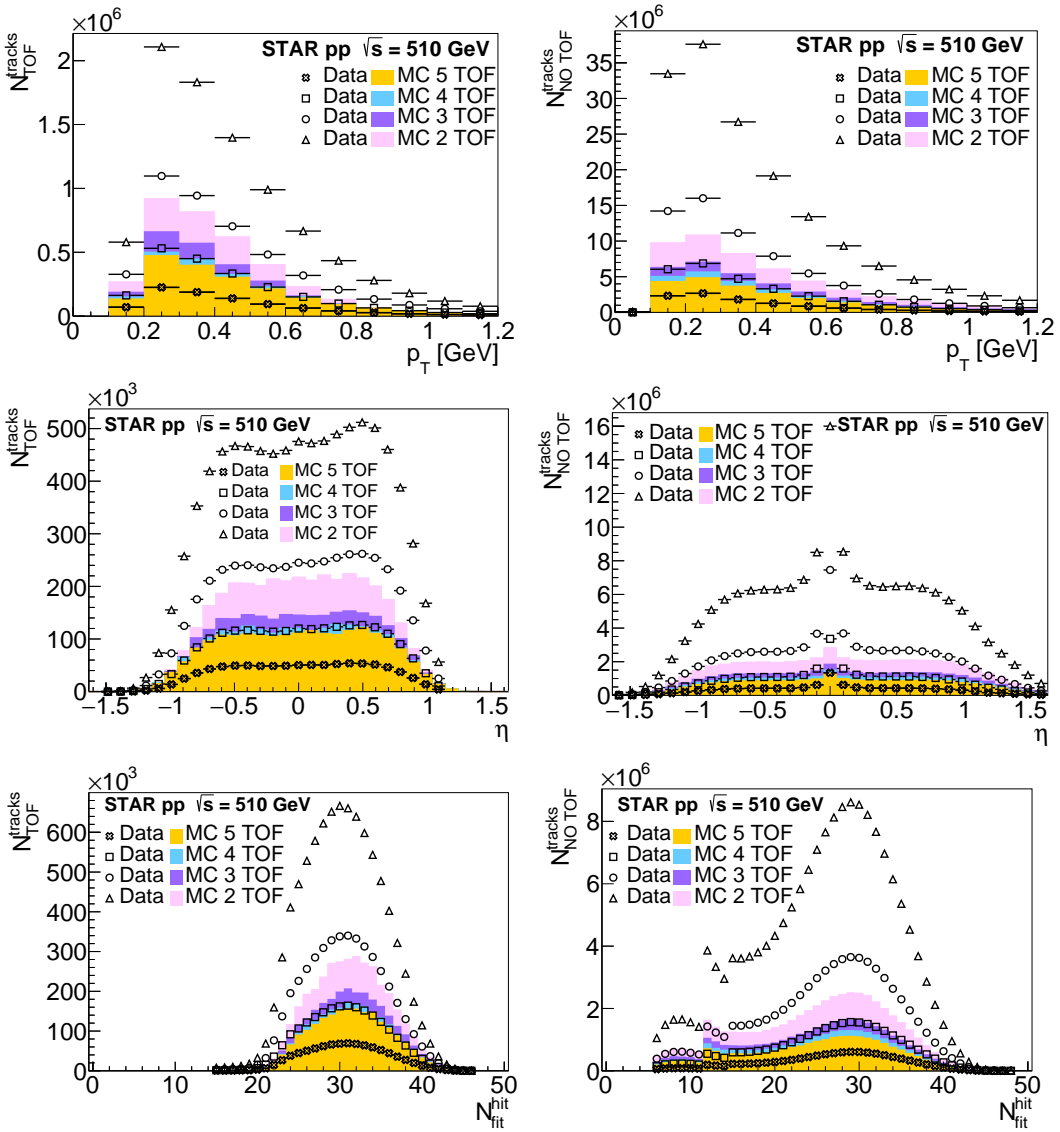


Figure 19: Distributions of the transverse momentum p_T (top), the pseudorapidity η (middle), and the number of hits used for track reconstruction $N_{\text{fit}}^{\text{hit}}$ (bottom), of global tracks matched (left) and not matched (right) with TOF detector. The MC histograms were scaled by the ratio of the number of events with $N_{\text{TOF}}^{\text{tracks}} = 4$ in data and MC (83.56 ± 1.05).

three tracks matched with the TOF detector, respectively. Otherwise, the total sum of charges of TOF-matched tracks must equal ± 1 .

The narrow mass window $m_{\pi^+\pi^-} \in [0.48, 0.52]$ GeV is a chosen kaon mass range used to select the pion pairs, which invariant mass is within a small deviation from PDG value of the kaon mass. For the events with $N_{\text{TOF}}^{\text{tracks}} = 4$, the four opposite high-quality tracks matched with TOF give two possible combinations. The combinations that give the kaon masses closest to the PDG (Particle Data Group) kaon mass were chosen to remove the ambiguity. The kaon with larger p_T was labelled as the “leading”, and the other kaon was labelled “subleading”. A similar approach was taken for the case with $N_{\text{TOF}}^{\text{tracks}} = 2$ and $N_{\text{TOF}}^{\text{tracks}} = 3$, where additional tracks to form kaon candidates were taken from high-quality tracks not matched with TOF. For the $N_{\text{TOF}}^{\text{tracks}} = 2$, the distinction between kaons was made based on the p_T , whereas, for the case with $N_{\text{TOF}}^{\text{tracks}} = 3$, the kaons were distinct based on the number of TOF-matched tracks that form a kaon. The labels for $N_{\text{TOF}}^{\text{tracks}} = 3$ are “2 TOF” and “1 TOF”. For $N_{\text{TOF}}^{\text{tracks}} = 5$, the pair is primarily selected by fulfilling the geometrical cuts (SC 5). If ambiguity continues after applying those cuts to all possible combinations, the combination with the lowest distance to the kaon PDG mass is selected. Figure 20 presents a two-dimensional distribution of the invariant mass of the pion pairs. From top to bottom, plots correspond to the events with $N_{\text{TOF}}^{\text{tracks}} = 5$ to 2. The plots on the left show the data, while the plots on the right show the MC sample. Figure 20 illustrates that we select mostly the events centred around the actual kaon mass for each $N_{\text{TOF}}^{\text{tracks}}$. For all cases, the excess of the events around the PDG value mass of K_S^0 suggests $K_S^0\bar{K}_S^0$ pair production. However, those events are not necessarily exclusive. To isolate the desired final state of four pions and two protons, we impose additional selection criteria SC 4–9.

Figures 21–32 show observables used as selection criteria SC 4–9 in two conventions. The left plots present the given quantity after finding candidates for kaon pairs. The plots on the right are presented in a convention, where all other selection criteria are applied except the one plotted, as listed at the beginning of this section. Normalization of the MC sample on the left plots was done to the number of the events with four good quality tracks $N_{\text{TOF}}^{\text{good tracks}} = 4$ (good track is defined by the SC 3.2–3.4). The data-to-MC ratio of those events equals 74.9 ± 1.6 . For the righplots, the MC was scaled to the number of events with four good quality tracks $N_{\text{TOF}}^{\text{good tracks}} = 4$ with the missing transverse momentum $p_T^{\text{miss}} \leq 0.15$ GeV. The data-to-MC ratio of those events equals 0.184 ± 0.054 . From that point, the “TOF” in the legends denotes high-quality tracks matched with the TOF detector.

The most important measure of the exclusivity of the event is the missing transverse momentum p_T^{miss} , which is the total transverse momentum of all final state particles: two protons and two centrally produced kaons:

$$p_T^{\text{miss}} = \sqrt{(p_x^E + p_x^W + p_x^{\text{leading}} + p_x^{\text{subleading}})^2 + (p_y^E + p_y^W + p_y^{\text{leading}} + p_y^{\text{subleading}})^2}. \quad (30)$$

Labels “leading” and “subleading” refers to the $N_{\text{TOF}}^{\text{good tracks}} = 2, 4$, and 5. For the $N_{\text{TOF}}^{\text{good tracks}} = 3$ the labels are replaced by “2 TOF” and “1 TOF”.

Distribution of p_T^{miss} is shown in Fig. 21. The application of all the other selection criteria suppresses the background and reveals the surplus of events for low values of p_T^{miss} for the case with $N_{\text{TOF}}^{\text{tracks}} = 4$ and 3. That surplus of the events around the

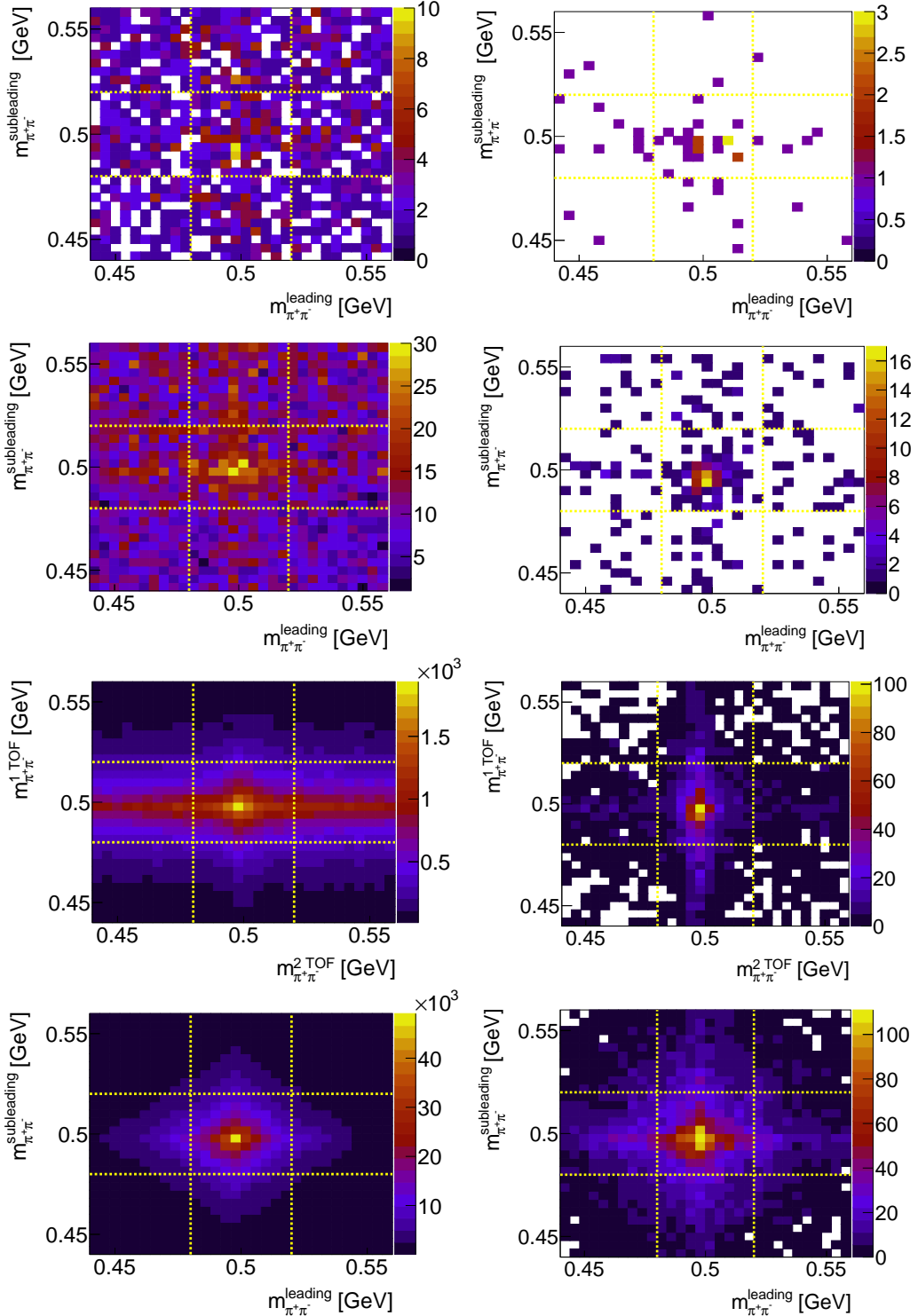


Figure 20: Two-dimensional distributions of the invariant masses of the pion pairs. The left-hand side plots illustrate data, while the right-hand side plots the MC sample. From top to bottom, plots correspond to the events with $N_{\text{TOF}}^{\text{tracks}} = 5$ to 2. All plots show characteristic excess around the mass of the kaon candidates. MC is not normalized to the data.

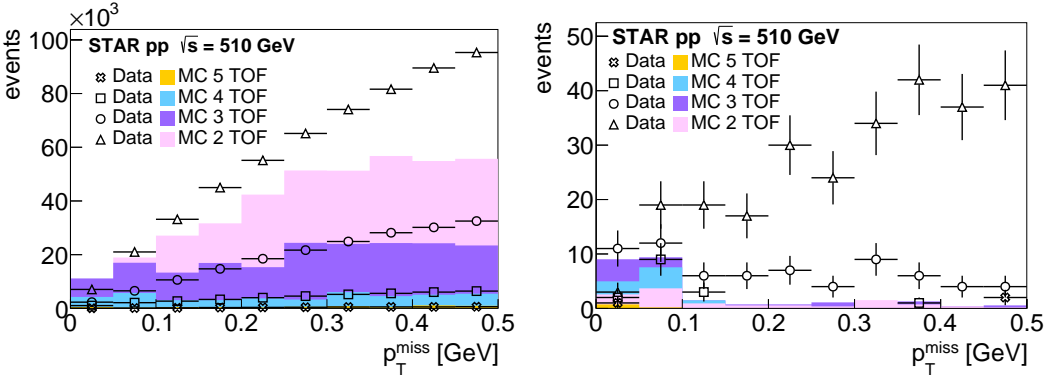


Figure 21: Distributions of p_T^{miss} after finding kaon pair candidate (left) and after applying all other selection criteria (right). We demand $p_T^{\text{miss}} \leq 0.15$ GeV. All MC histograms on the left are scaled to the number of the events in data with $N_{\text{TOF}}^{\text{good tracks}} = 4$ (data-to-MC ratio: 74.9 ± 1.6), and on the right to the number of events with $N_{\text{TOF}}^{\text{good tracks}} = 4$ and $p_T^{\text{miss}} \leq 0.15$ GeV (data-to-MC ratio: 0.184 ± 0.054).

near-zero values of the total transverse momentum is characteristic of CEP due to momentum conservation. A relatively large background is still present for the events with $N_{\text{TOF}}^{\text{tracks}} = 2$. The maximum allowed value of p_T^{miss} was set to 0.15 GeV. For the events with $N_{\text{TOF}}^{\text{tracks}} = 5$ only one event remains within $p_T^{\text{miss}} \leq 0.15$ GeV range.

Although we consider the events with the specific number of the global tracks matched with the TOF detector $N_{\text{TOF}}^{\text{tracks}}$, an event can contain hits not assigned to the TPC tracks by the matching algorithm. We construct the cluster in the TOF detector by merging the hits registered in adjacent MRPC modules in a given tray. The distribution of the $N_{\text{TOF}}^{\text{cluster}}$ is presented in Fig. 22. To preserve events with the additional signal that might be the noise, we set the requirement on the number of the TOF clusters as $N_{\text{TOF}}^{\text{cluster}} \leq 2 \cdot N_{\text{TOF}}^{\text{tracks}} + 1$.

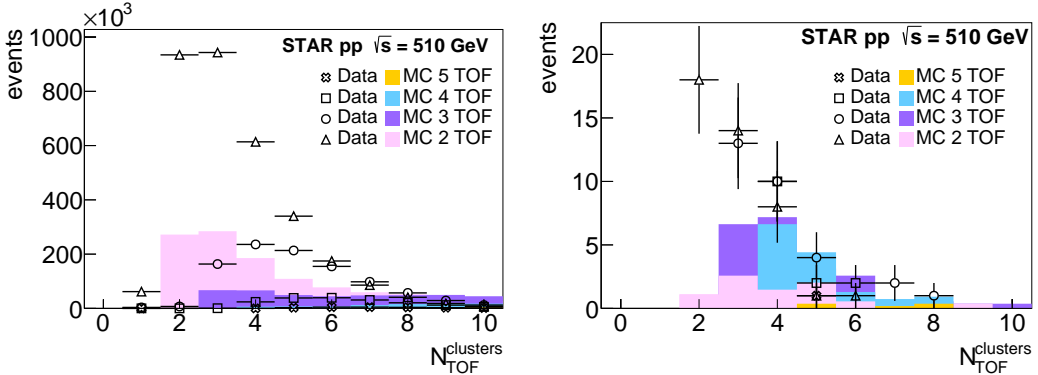


Figure 22: Distributions of the number of the TOF clusters $N_{\text{TOF}}^{\text{cluster}}$ after finding kaon candidates (left), and after applying all other selection criteria (right). We require $N_{\text{TOF}}^{\text{cluster}} \leq 2 \cdot N_{\text{TOF}}^{\text{tracks}} + 1$. All MC histograms on the left are scaled to the number of events in data with $N_{\text{TOF}}^{\text{good tracks}} = 4$ (data-to-MC ratio: 74.9 ± 1.6), and on the right to the number of events with $N_{\text{TOF}}^{\text{good tracks}} = 4$ and $p_T^{\text{miss}} \leq 0.15$ GeV (data-to-MC ratio: 0.184 ± 0.054).

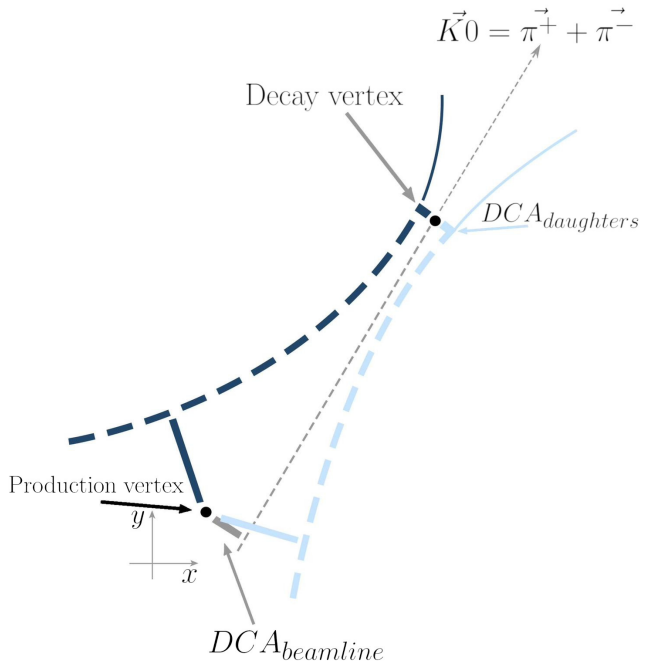


Figure 23: Graphical representation of geometrical quantities used for the reconstruction of the decay and production vertices of the K_S^0 candidate.

As addressed in Sec. 2.3, the analysis is done for the global tracks that do not contain particle origin information. The reason behind using the global tracks instead of the primary ones with reconstructed vertices lies in the problem of erroneous combining two decay vertices of the kaons into one, which leads to complications in the data analysis and decreases the number of potential signal events. The position of the production and decay vertices of the kaon can be reconstructed based on the position of the beamline in a given event. Figure 23 presents a transverse plane with pion trajectories. The pions are moved along their helices to the distance of the closest approach (DCA_{daughters}). The middle point of the line joining points of their DCA_{daughters} is assumed to be the position of the decay vertex of the kaon. The sum of pions momenta at the points of closest approach gives the kaon momentum and the line along which the kaon candidate was moving (\vec{K}^0), as the presence of the magnetic field does not impact the neutral particle. We can determine the position of the production vertex, assuming it lies on the beamline, within the distance of the closest approach to the line going through \vec{K}^0 vector (DCA_{beamline}). The distributions of the DCA_{beamline} and DCA_{daughters} are shown in Figs. 24 and 25, respectively. We require that the DCA_{daughters} and DCA_{beamline} be lower than 2.5 cm for the kaon formed from two TOF-matched tracks and lower than 1.5 cm for the kaon formed from only one TOF-matched track. The position of the production and decay vertices determine the decay length l_{decay} , and the pointing angle α_p . The decay length is the distance between decay and production vertices, while the α_p is an angle between the vector that goes through both vertices and the \vec{K}^0 vector. The distribution of l_{decay} and $\cos(\alpha_p)$ are show in Fig. 26. For the kaon formed from two TOF-matched

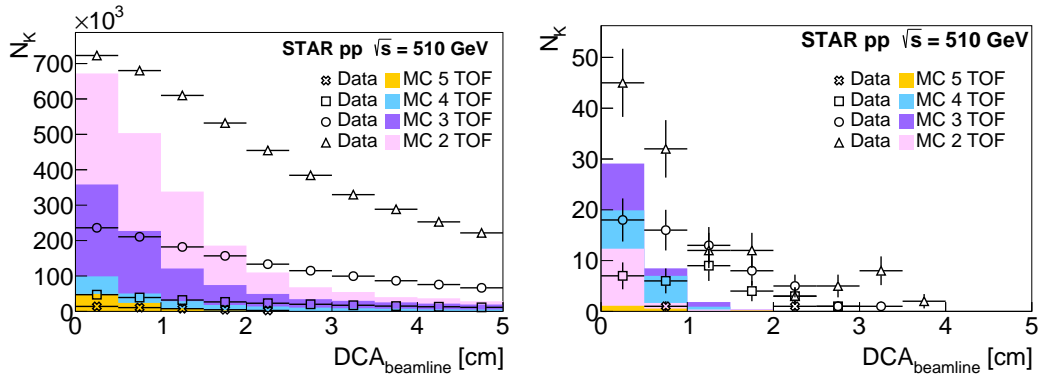


Figure 24: Distributions of $DCA_{beamline}$, after finding kaon candidates (left), and after applying all other selection criteria (right). MC histograms on the left are scaled to the number of the events in data for the case with $N_{TOF}^{good\ tracks} = 4$ (data-to-MC ratio: 74.9 ± 1.6), and on the right to the number of events with $N_{TOF}^{good\ tracks} = 4$ and $p_T^{\text{miss}} \leq 0.15$ GeV (data-to-MC ratio: 0.184 ± 0.054).

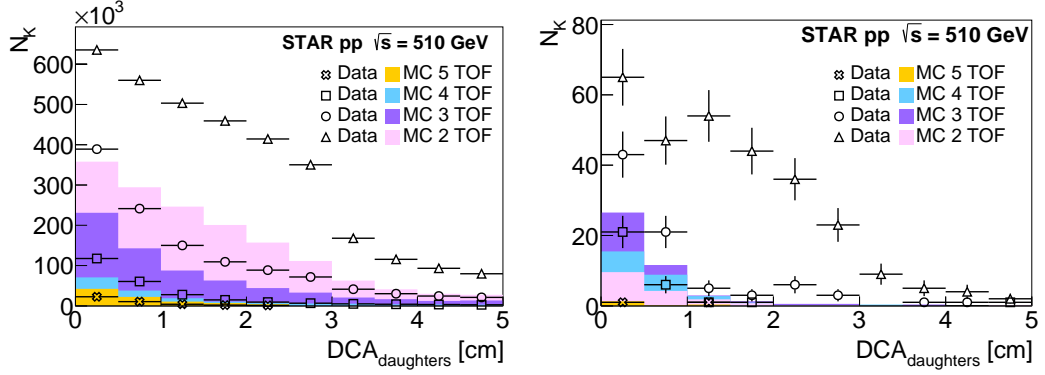


Figure 25: Distributions of $DCA_{daughters}$, after finding kaon candidates (left), and after applying all other selection criteria (right). MC histograms on the left are scaled to the number of the events in data for the case with $N_{TOF}^{good\ tracks} = 4$ (data-to-MC ratio: 74.9 ± 1.6), and on the right to the number of events with $N_{TOF}^{good\ tracks} = 4$ and $p_T^{\text{miss}} \leq 0.15$ GeV (data-to-MC ratio: 0.184 ± 0.054).

tracks, we select data with $\cos(\alpha_p) \geq 0.925$ or $l_{\text{decay}} < 3.0$ cm, while for the case with one TOF track the condition is $\cos(\alpha_p) \geq 0.95$.

Due to relatively small four-momenta transfers at proton vertices in the CEP process at RHIC and finite measurement resolutions of scattered proton momenta, an accidental overlap of elastic proton-proton scattering with an activity in the central detector may mimic the CEP process. A large cross-section for the elastic scattering makes such accidental overlaps a significant background to the process studied in this thesis. To reduce this background, we remove events from the data sample with protons scattered approximately back-to-back (i.e., resembling the topology of elastic scattering).

Elastic scattering is defined based on four-momentum conservation as explained in SC 6. The event is considered a candidate for CEP if at least one of the conditions in SC 6 is unsatisfied. Figure 27 presents the distributions of the x and y coordinates

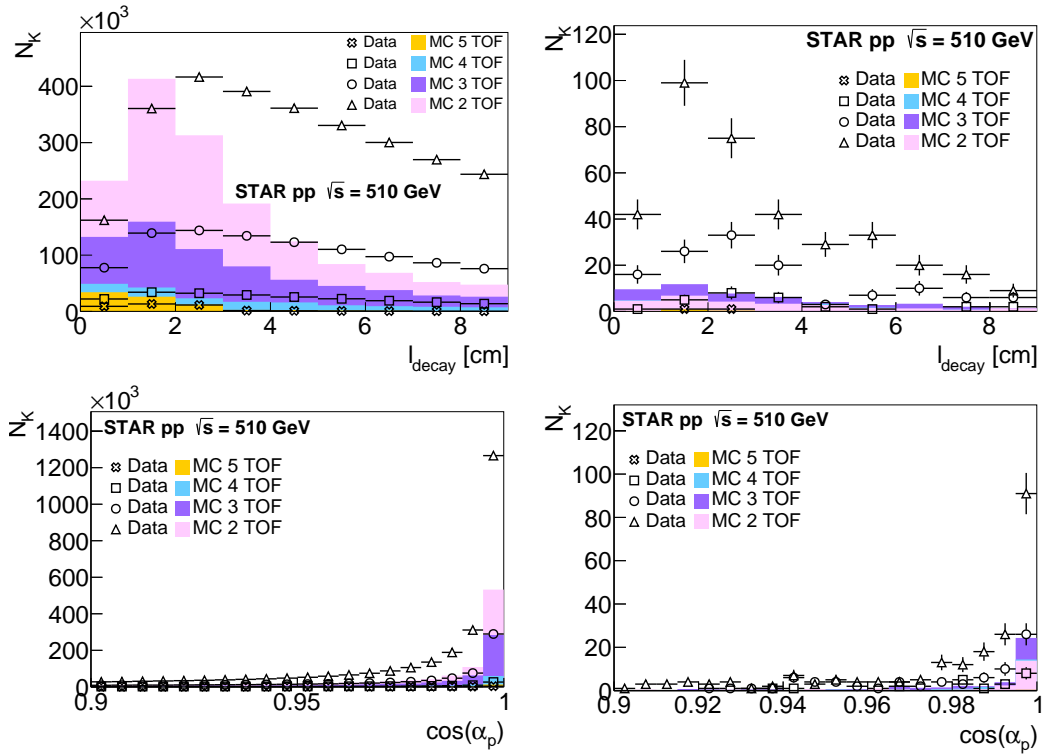


Figure 26: Distributions of the decay length l_{decay} (top) and the cosine of the pointing angle $\cos(\alpha_p)$ (bottom) after finding kaon pairs (left), and after applying all other selection criteria (right). MC histograms on the left are scaled to the number of the events in the data for the case with $N_{\text{TOF}}^{\text{good tracks}} = 4$ (data-to-MC ratio: 74.9 ± 1.6), and on the right to the number of events with $N_{\text{TOF}}^{\text{good tracks}} = 4$ and $p_T^{\text{miss}} \leq 0.15$ GeV (data-to-MC ratio: 0.184 ± 0.054).

the protons' total momentum and their relative energy losses ξ^E and ξ^W .

The kinematic relations introduced in Sec. 1.3 can be used as the experimental constraints due to the possibility of the simultaneous measurement of the intact protons and centrally produced system. Equations (12), (16), and (17) were used in the analysis. We use the correlation selection criteria introduced in SC 7, which should be centred around zero for the CEP processes. Their distributions are shown in Figs. 28 – 30.

The SC 8 are related to the position of kaon decay vertices. The top diagrams in Fig. 31 show the average position z of the decay vertices of leading and sub-leading kaons. The average position should satisfy the requirement $(\text{vtx}_z^{\text{leading}} + \text{vtx}_z^{\text{subleading}})/2 \leq 80.0$ cm. The bottom graph shows the distance between leading and subleading decay vertices in z direction, which should satisfy the condition $|\text{vtx}_z^{\text{leading}} - \text{vtx}_z^{\text{subleading}}| \leq 15.0$ cm.

The final selection criterion is imposed on the angle between pions in the rest frame of the kaon parent particle θ^* . The condition for that quantity is $|\cos(\theta^*)| \leq 0.8$.

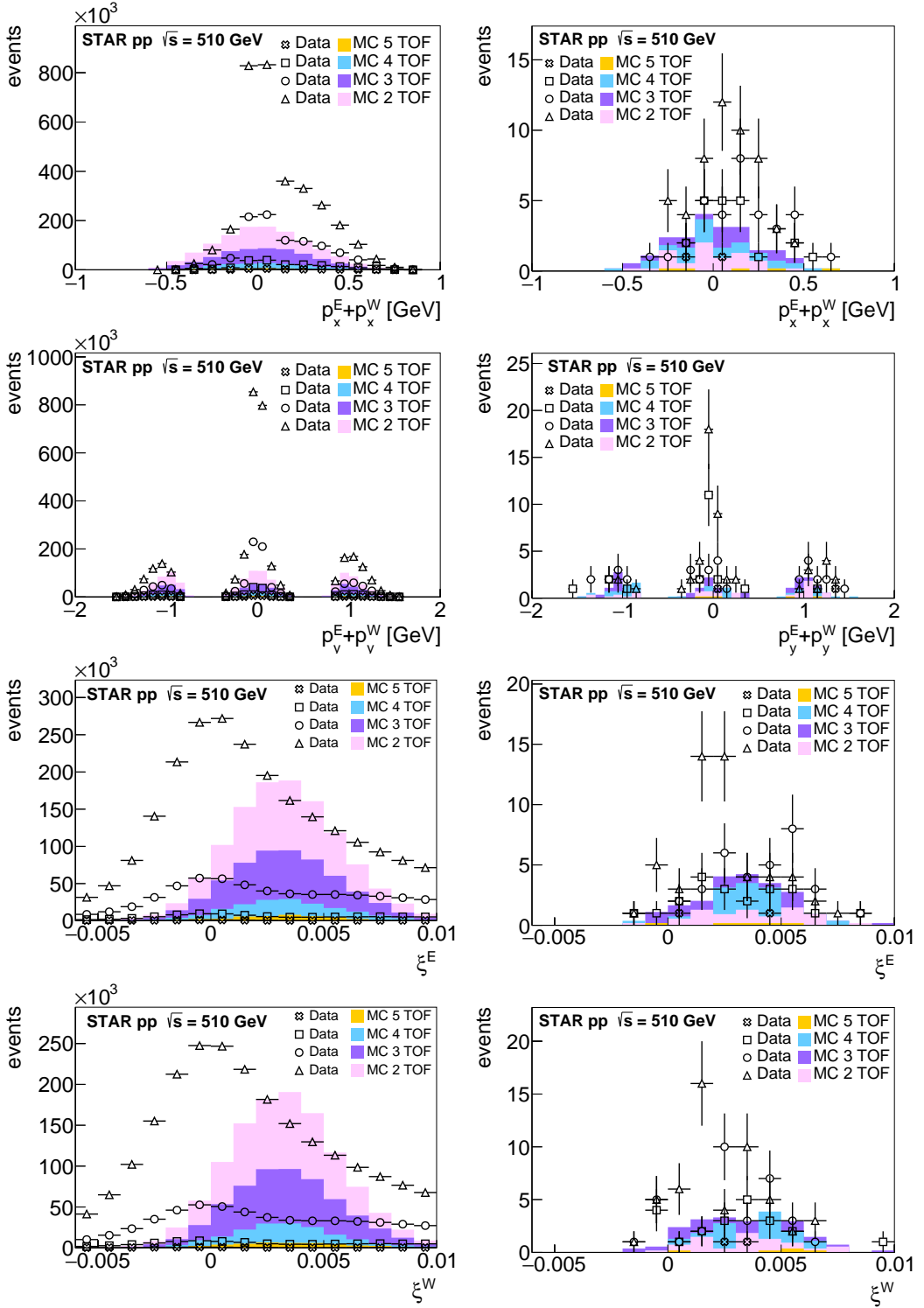


Figure 27: Distributions of the sum of the x -component (top), y -component (second from top) of the protons momenta, the relative loss of the momentum ξ^E (third from top), and ξ^W (bottom), after finding kaon pairs (left), and after applying all other selection criteria (right). Not meeting one of the SC 6 conditions results in accepting the event. The MC histograms on the left are scaled to the number of the events with $N_{\text{TOF}}^{\text{good tracks}} = 4$ (data-to-MC ratio: 74.9 ± 1.6), and on the right to the number of events with $N_{\text{TOF}}^{\text{good tracks}} = 4$ and $p_T^{\text{miss}} \leq 0.15$ GeV (data-to-MC ratio: 0.184 ± 0.054).

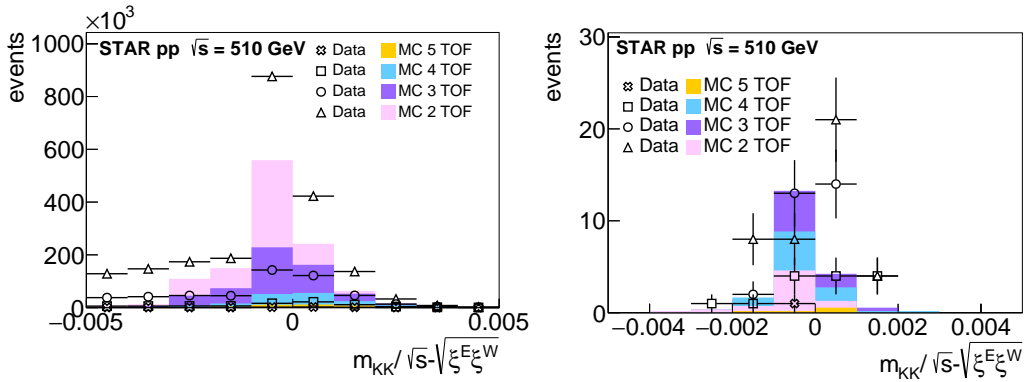


Figure 28: Distributions of the kinematic correlation used in SC 7.1, after finding candidates for the kaon pairs (left) and after applying all other selection criteria (right). MC histograms on the left are scaled to the number of the events in the data for the case with $N_{\text{TOF}}^{\text{good tracks}} = 4$ (data-to-MC ratio: 74.9 ± 1.6), and on the right to the number of events with $N_{\text{TOF}}^{\text{good tracks}} = 4$ and $p_T^{\text{miss}} \leq 0.15 \text{ GeV}$ (0.184 ± 0.054).

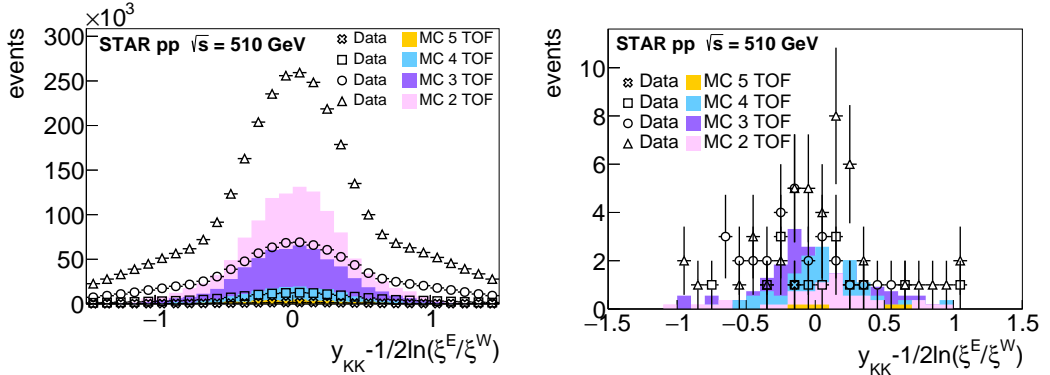


Figure 29: Distributions of the kinematic correlation used in SC 7.2, after finding candidates for the kaon pairs (left), and after applying all other selection criteria (right). MC histograms on the left are scaled to the number of the events in the data for the case with $N_{\text{TOF}}^{\text{good tracks}} = 4$ (data-to-MC ratio: 74.9 ± 1.6), and on the right to the number of events with $N_{\text{TOF}}^{\text{good tracks}} = 4$ and $p_T^{\text{miss}} \leq 0.15 \text{ GeV}$ (0.184 ± 0.054).

3.2 Selection criteria efficiency

In this section, we discuss the efficiency of the applied selection criteria. The calculation was performed on the MC events with four pions from the central exclusive production within the kinematic region defined by the true transverse momentum p_T^{true} and true pseudorapidity η^{true} :

- $p_T^{\text{true}} > 0.2 \text{ GeV}$,
- $|\eta^{\text{true}}| < 0.9$.

True-level pions were matched with the TPC tracks from the detector-level MC

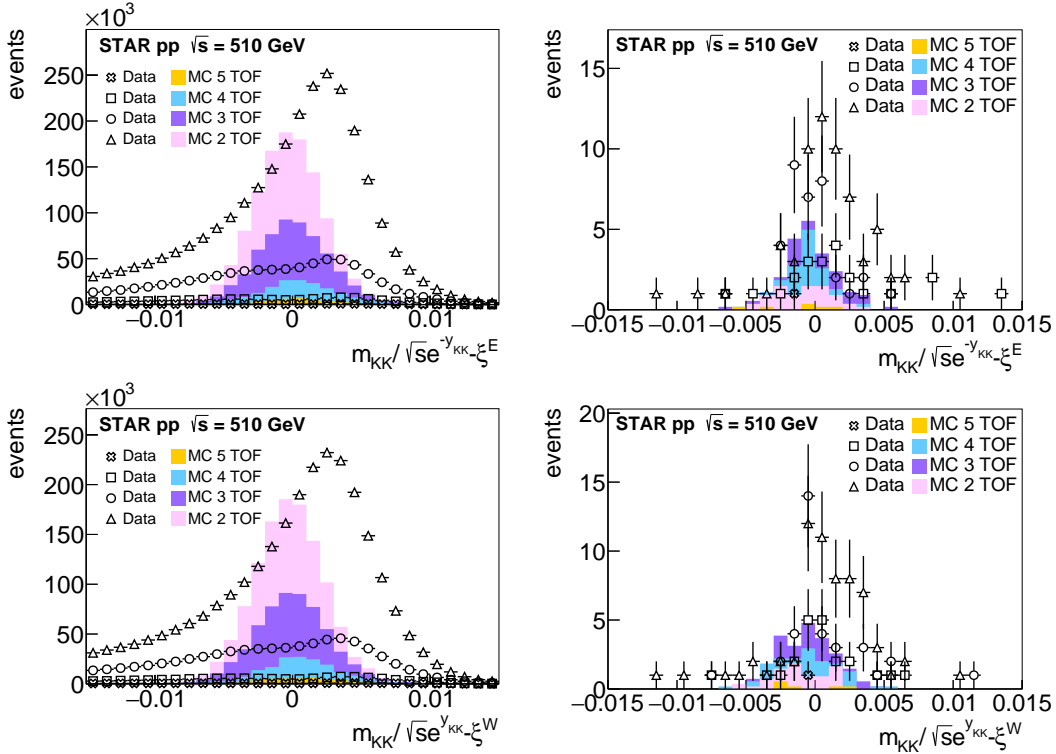


Figure 30: Distributions of the kinematic correlation used in SC7.3, after finding candidates for the kaon pairs (left), and after applying all other selection criteria (right). MC histograms on the left are scaled to the number of the events in the data for the case with $N_{\text{TOF}}^{\text{good tracks}} = 4$ (data-to-MC ratio: 74.9 ± 1.6), and on the right to the number of events with $N_{\text{TOF}}^{\text{good tracks}} = 4$ and $p_T^{\text{miss}} \leq 0.15 \text{ GeV}$ (0.184 ± 0.054).

simulation based on the smallest distance δ in $\eta - \phi$ space:

$$\delta = \sqrt{(\eta^{\text{true}} - \eta^{\text{det}})^2 + (\phi^{\text{true}} - \phi^{\text{det}})^2} \quad (31)$$

with the labels det and true denoting the values at the detector and the true level of the pseudorapidity η and azimuthal angle ϕ , respectively. The matching is accepted provided the value of the δ is sufficiently small: $\delta \leq 0.15$, and the matched TPC tracks fulfil the following requirements:

- pseudorapidity range: $|\eta^{\text{det}}| \leq 0.9$
- transverse momentum: $p_T^{\text{det}} \geq 0.2 \text{ GeV}$
- at least 20 hits for TPC track reconstruction $N_{\text{hit}}^{\text{fit}} \geq 20$

Figure 33 presents the examples of the event topologies in $\eta - \phi$ space. The TPC tracks matched with TOF are marked as black circles, true level pions are purple disks, and TPC tracks matched with true particles are marked as red crosses. The yellow stars indicate intact protons, while the green circles the TPC tracks not matched with a hit in TOF. The top image shows an ideal matching where four TOF-matched tracks are assigned to the true level pions. The middle image illustrates an

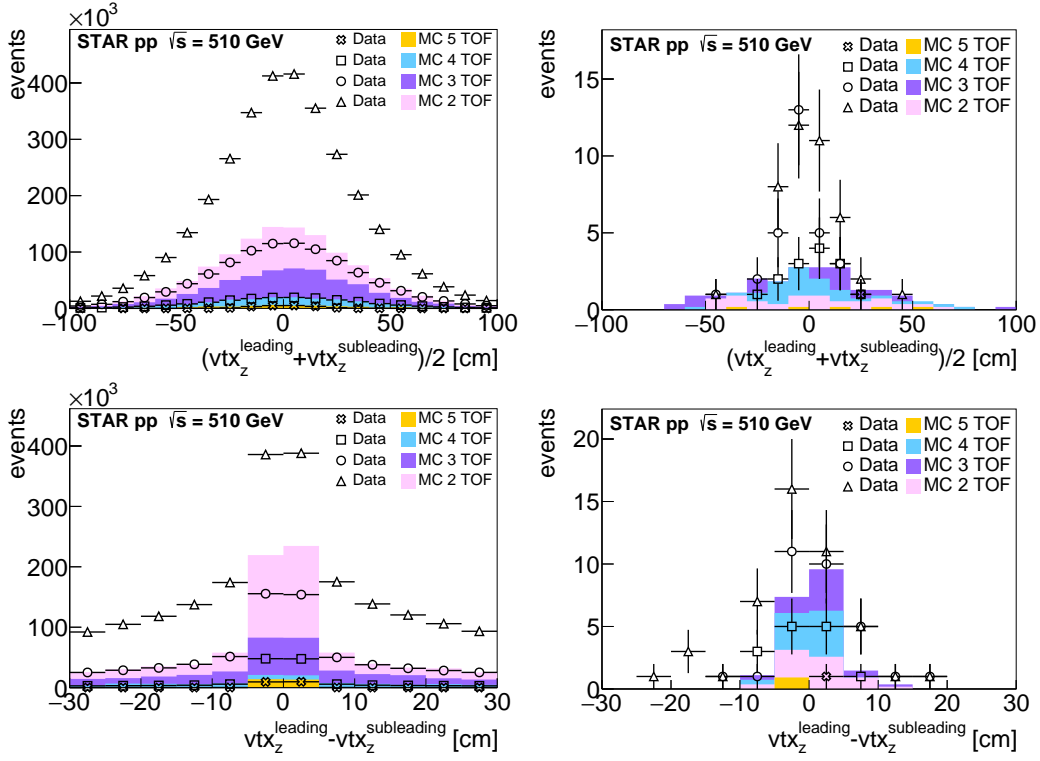


Figure 31: Distributions of the mean position (top), and difference (bottom) of the decay vertices of kaons, after finding kaon candidates (left), and after applying all other selection criteria (right). MC histograms on the left are scaled to the number of the events with $N_{\text{TOF}}^{\text{good tracks}} = 4$ (data-to-MC ratio: 74.9 ± 1.6), and on the right to the number of events with $N_{\text{TOF}}^{\text{good tracks}} = 4$ and $p_T^{\text{miss}} \leq 0.15$ GeV (data-to-MC ratio: 0.184 ± 0.054).

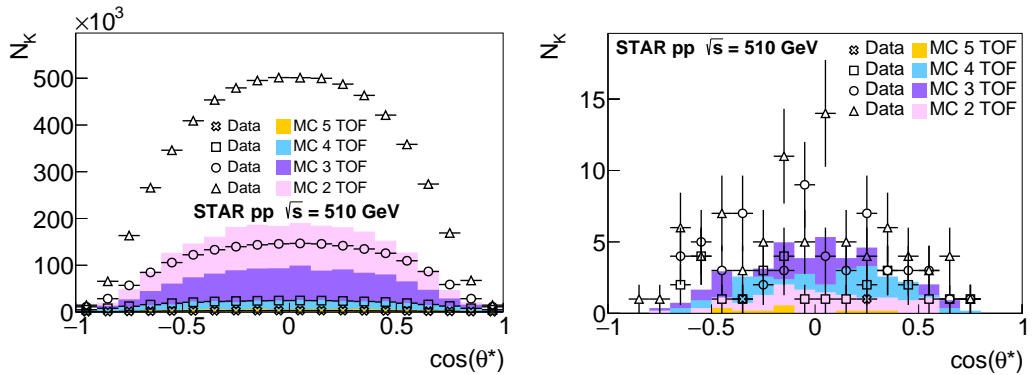


Figure 32: Distributions of the angle between pions in the rest frame of the parent kaon after finding kaon candidates (left), and after applying all other selection criteria (right). MC histograms on the left are scaled to the number of the events in the data for the case with $N_{\text{TOF}}^{\text{good tracks}} = 4$ (data-to-MC ratio: 74.9 ± 1.6), and on the right to the number of events with $N_{\text{TOF}}^{\text{good tracks}} = 4$ and $p_T^{\text{miss}} \leq 0.15$ GeV (0.184 ± 0.054).

example where one of the four matched TPC tracks does not have a hit in the TOF detector. The bottom plot depicts an example where only two tracks were matched to the true level pions. The remaining were not matched to true particles as there were no TPC tracks of good quality within the distance of $\delta \leq 0.15$. Events of that kind are not considered when determining the efficiency of the selection criteria.

The events with signals above the threshold in large BBC tiles were dismissed to simulate the trigger. After the matching procedure, we are left with $N_m = 604 \pm 25$ events that are further used in calculating the selection criteria efficiency ϵ . The efficiency was determined for three cases of the TOF tracks $N_{\text{TOF}}^{\text{tracks}} = 2, 3$, and 4 matched to the true pions from central exclusive production. The efficiency for the given selection criterion is calculated as the ratio between the number of events that passed the given requirement $N_p(N_{\text{TOF}}^{\text{tracks}})$ to the number of the events after the matching procedure N_m . The efficiency ϵ is given by:

$$\epsilon = \frac{N_p(N_{\text{TOF}}^{\text{tracks}})}{N_p(N_{\text{TOF}}^{\text{tracks}}) + N_n(N_{\text{TOF}}^{\text{tracks}})}, \quad (32)$$

where $N_n(N_{\text{TOF}}^{\text{tracks}}) = N_m - N_p(N_{\text{TOF}}^{\text{tracks}})$. The uncertainties for N_p and N_n were taken as the corresponding square roots. The uncertainty of the efficiency is calculated as follows:

$$u(\epsilon) = \frac{\sqrt{(N_p \cdot u(N_n))^2 + (N_n \cdot u(N_p))^2}}{N_p + N_n}. \quad (33)$$

Figure 34 presents the distributions of the invariant mass $m_{\pi^+\pi^-}$, missing transverse momentum p_T^{miss} , and number of TOF clusters $N_{\text{TOF}}^{\text{cluster}}$ with applied selection criteria SC 4. The total number of events that passed the N_p or not the N_n selection criterion with calculated uncertainties is presented in Tab. 1.

The geometrical quantities: DCA_{beamline}, DCA_{daughters}, l_{decay} , and $\cos(\alpha_p)$ are illustrated in Fig. 35 with SC 5. The summary of numbers of the events that pass N_p or do not pass N_n for the given criterion with calculated efficiencies and uncertainties are listed in Tab. 2.

Figure 36 presents the sum of the momenta of the protons for x and y coordinate and relative losses of the protons with illustrated elastic SC 6. If at least one of the elastic requirements is not fulfilled, an event will be accepted as a potential CEP process. Table 3 presents the summarized number of events that passed anti-elastic selection with efficiencies. The distributions of the kinematic correlations with SC 7 are shown in Fig. 37 and Tab. 4. SC 8 and 9 are presented in Fig. 38 and Tab. 5.

The summary plot of all discussed selection criteria is presented in Fig. 39. The selection criteria are most efficient for the case of three TOF tracks matched with true-level pions. The lowest efficiency was attained for the case with four TOF tracks, apart from the selection on the l_{decay} and $\cos(\alpha_p)$ where the lowest efficiency was obtained for two TOF tracks.

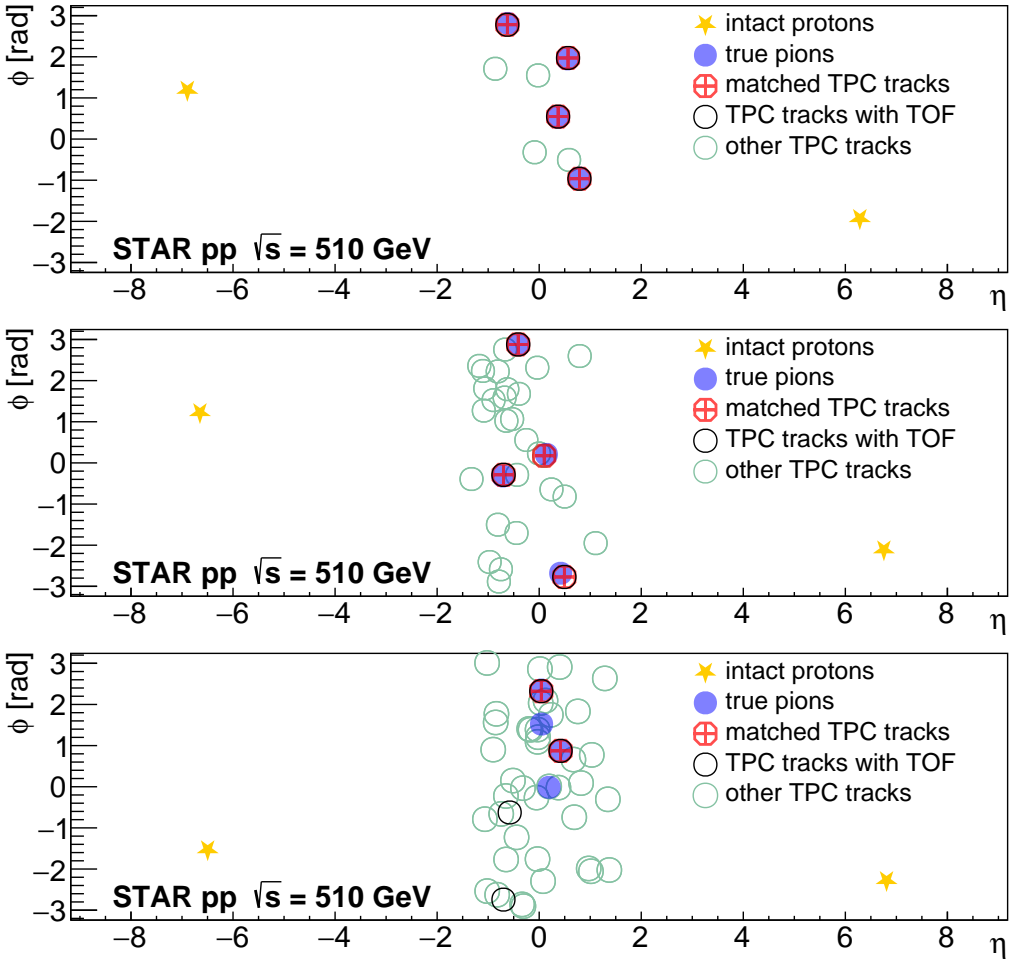


Figure 33: Examples of the MC event’s $\eta - \phi$ phase space illustrate true-level pions and TPC track matching. Yellow stars mark intact protons, and purple disks mark true-level pions, whose decay results from the true K_S^0 mesons formed in CEP. Purple disks mark true pions, red crosses indicate global tracks matched with true level, black circles TPC tracks with TOF hit, and green circles mark TPC tracks not assigned to the TOF hit. The top and middle images present cases where four TPC tracks were matched with true-level particles. In the top image, all matched tracks have the TOF hit, while in the middle image, only three. The bottom image presents a case dismissed from the efficiency calculation, where only two TPC tracks were matched with true-level pions.

3.3 Time-of-flight detector efficiency

This section presents the methods and results of estimating the TOF detector efficiency. The efficiency obtained separately from the data and detector-level MC was determined with the *tag-and-probe* method, and results were compared with the efficiency obtained directly based on the true-level MC.

The tag-and-probe method is a data-driven (i.e., detector-level) technique used to determine efficiency. The *tag* denotes a reference object, and a *probe* is an object that may or may not possess the feature under investigation. In our analysis, the

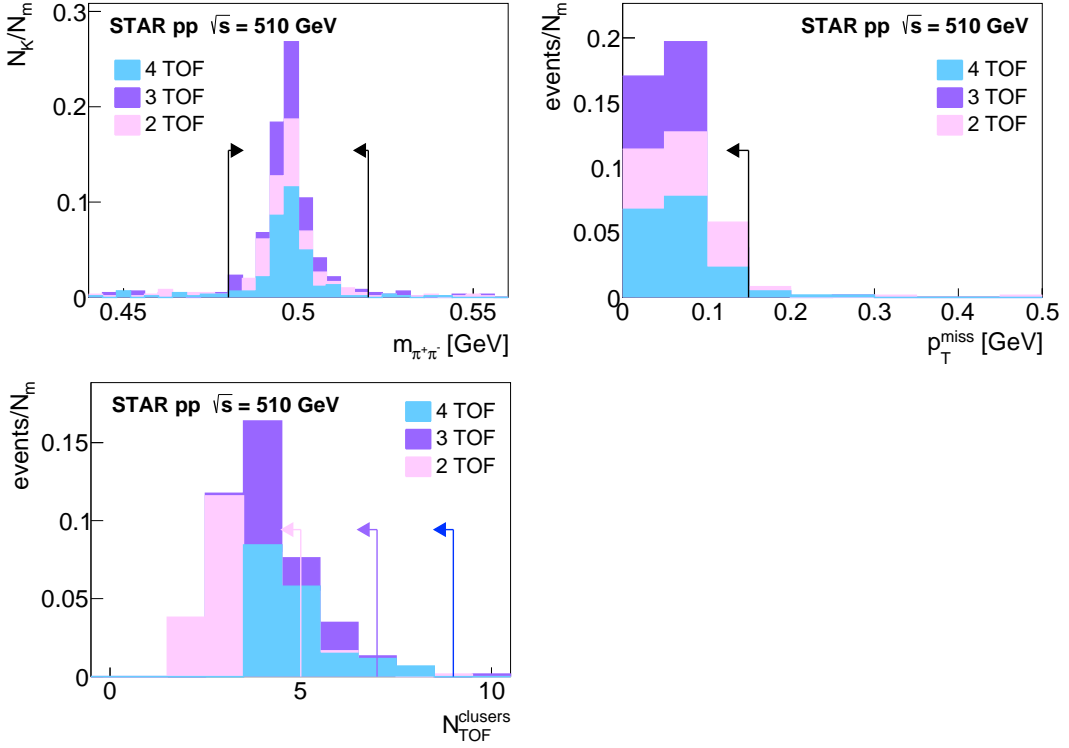


Figure 34: Distribution of the invariant mass $m_{\pi^+\pi^-}$ (top left), missing transverse momentum p_T^{miss} (top right), and $N_{\text{TOF}}^{\text{cluster}}$ (bottom left) with applied SC 4.

cut	$N_{\text{TOF}}^{\text{tracks}}$	N_p	$u(N_p)$	N_n	$u(N_n)$	ε	$u(\varepsilon)$
$m_{\pi^+\pi^-}$ (SC 4.1)	4	88	9.381	516	22.716	0.146	0.014
	3	202	14.213	402	20.050	0.334	0.019
	2	141	11.874	463	21.517	0.233	0.017
p_T^{miss} (SC 4.2)	4	102	10.100	502	22.405	0.169	0.015
	3	245	15.652	359	18.947	0.406	0.020
	2	181	13.454	423	20.567	0.300	0.019
$N_{\text{TOF}}^{\text{cluster}}$ (SC 4.3)	4	106	10.296	498	22.316	0.175	0.015
	3	246	15.684	358	18.921	0.407	0.020
	2	178	13.342	426	20.640	0.295	0.019

Table 1: The number of events that pass N_p or not pass the selection criteria SC 4, with the calculated efficiencies and uncertainties for different values of $N_{\text{TOF}}^{\text{tracks}}$.

feature under investigation is a TOF hit assignment to the TPC track. By the tag, we understand the TPC track with TOF hit, while the probe is another (expected based on the process under study) TPC track that may or may not have a TOF match. Tag and probe tracks form a kaon. The efficiency is defined as the number of kaons formed from two TPC tracks with TOF (N_K^{TOF}) to the total number of K_S^0 candidates with at least one TOF-matched track. If the probe has a TOF hit, the pair is taken into account twice by interchanging the tag-probe roles. The formula

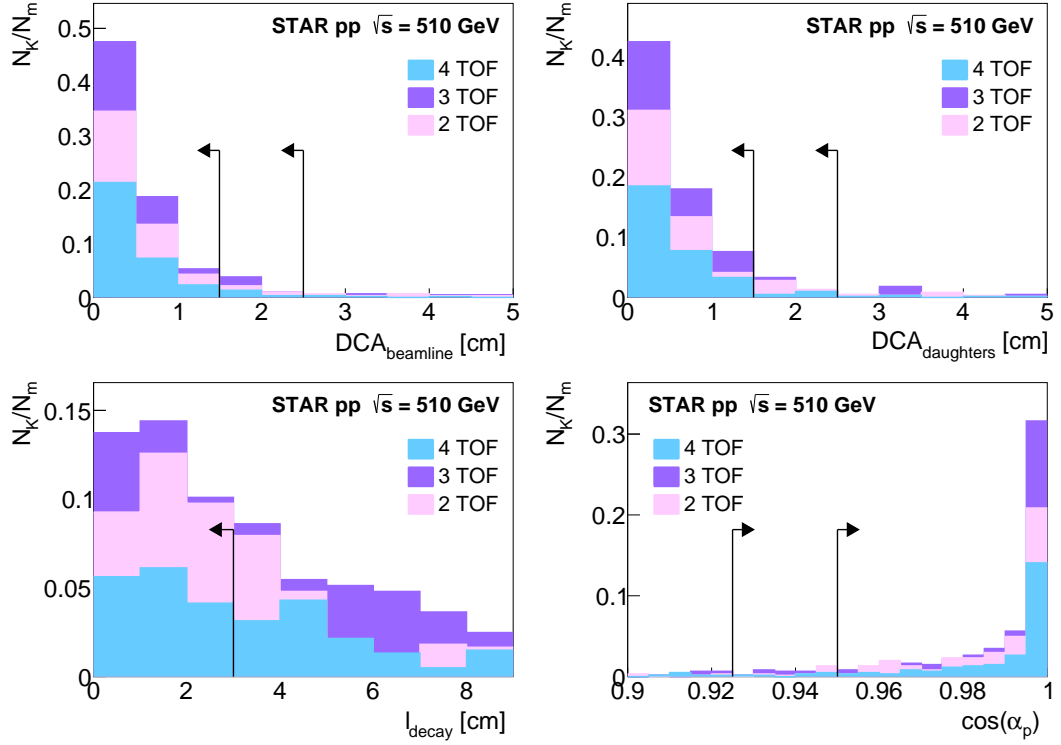


Figure 35: Distribution of the DCA_{beamline} (top left), $DCA_{\text{daughters}}$ (top right), l_{decay} (bottom left), and $\cos(\alpha_p)$ with indicated SC 5.

cut	$N_{\text{TOF}}^{\text{tracks}}$	N_p	$u(N_p)$	N_n	$u(N_n)$	ε	$u(\varepsilon)$
DCA _{beamline} (SC 5.1)	4	94	9.695	510	22.583	0.156	0.015
	3	197	14.036	407	20.174	0.326	0.019
	2	137	11.705	467	21.610	0.227	0.017
DCA _{daughters} (SC 5.2)	4	78	8.832	526	22.935	0.129	0.014
	3	163	12.767	441	21.000	0.270	0.018
	2	115	10.724	489	22.113	0.190	0.016
$l_{\text{decay}}, \cos(\alpha_p)$ (SC 5.3)	4	87	9.327	517	22.738	0.144	0.014
	3	126	11.225	478	21.863	0.209	0.017
	2	69	8.307	535	23.130	0.114	0.013

Table 2: The number of events that passed criterion N_p or did not pass the criterion N_n according to SC 5, with the calculated efficiency and uncertainties for different values of $N_{\text{TOF}}^{\text{tracks}}$.

gives the efficiency ε :

$$\varepsilon = \frac{N_K^{\text{2 TOF}}}{N_K^{\text{2 TOF}} + N_K^{\text{1 TOF}}}, \quad (34)$$

where $N_K^{\text{1 TOF}}$ denotes the kaons decayed into pions with one TOF hit. The TPC tracks used in the efficiency analysis must have fulfilled the nominal quality conditions as stated in SC 3.2, SC 3.3 and SC 3.4. The formed kaon had to meet the

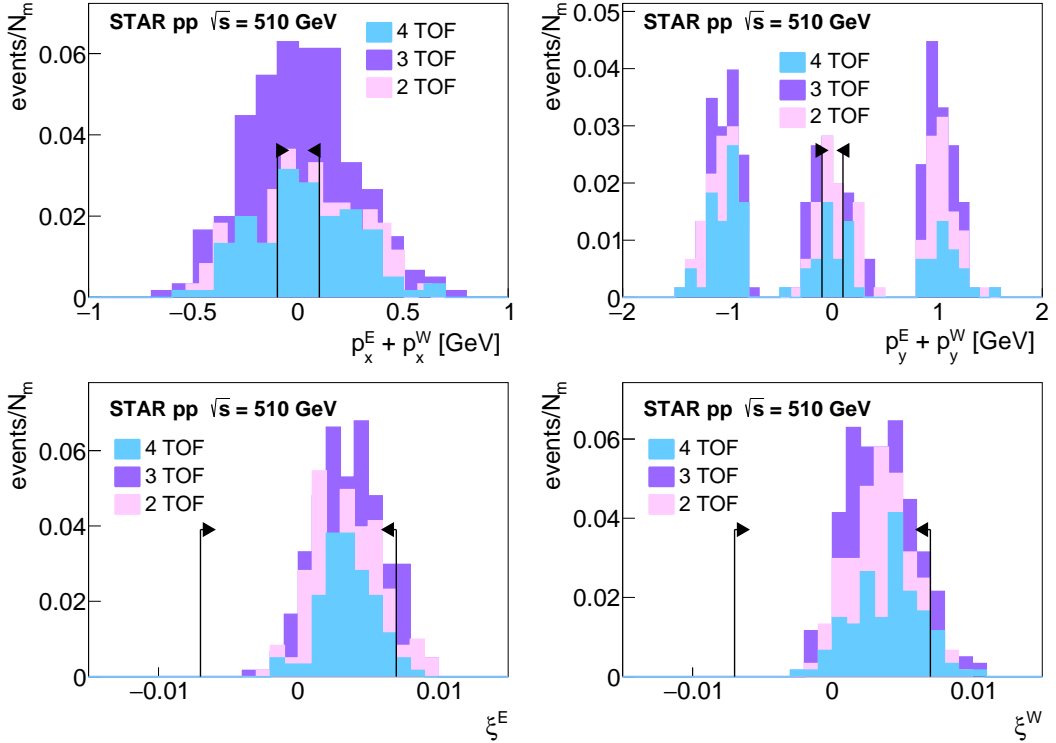


Figure 36: Distributions of the $p_x^E + p_x^W$ (top left), $p_y^E + p_y^W$ (top right), ξ^E (bottom left), and ξ^W (bottom right) with applied SC 6. The event is accepted if at least one of those requirements is not fulfilled.

$N_{\text{TOF}}^{\text{tracks}}$	N_p	$u(N_p)$	N_n	$u(N_n)$	ε	$u(\varepsilon)$
4	102	10.100	502	22.405	0.169	0.015
3	242	15.556	362	19.026	0.401	0.020
2	181	13.454	423	20.567	0.300	0.019

Table 3: The number of events that passed the selection criterion N_p or did not pass the criterion N_n according to anti-elastic SC 6, with the calculated efficiencies and uncertainties for different values of $N_{\text{TOF}}^{\text{tracks}}$.

following conditions:

- lowest distance between daughters $\text{DCA}_{\text{daughters}} < 1.0 \text{ cm}$,
- lowest distance between kaon trajectory to the beamline $\text{DCA}_{\text{beamline}} < 1.0 \text{ cm}$,
- z -coordinate of the decay vertex $|\text{vtx}_z| < 80 \text{ cm}$,
- transverse distance of the decay vertex to the beamline, $\sqrt{\text{vtx}_x^2 + \text{vtx}_y^2} < 3 \text{ cm}$.

The efficiency was determined as a function of the probe transverse momentum p_T^{probe} , probe pseudorapidity η^{probe} , and time (estimated utilizing the fill number). The number of kaons was taken from the fit to the invariant mass of the pion pairs (Figs. 40-45). The kaon signal was fitted with a Gaussian function, while the background

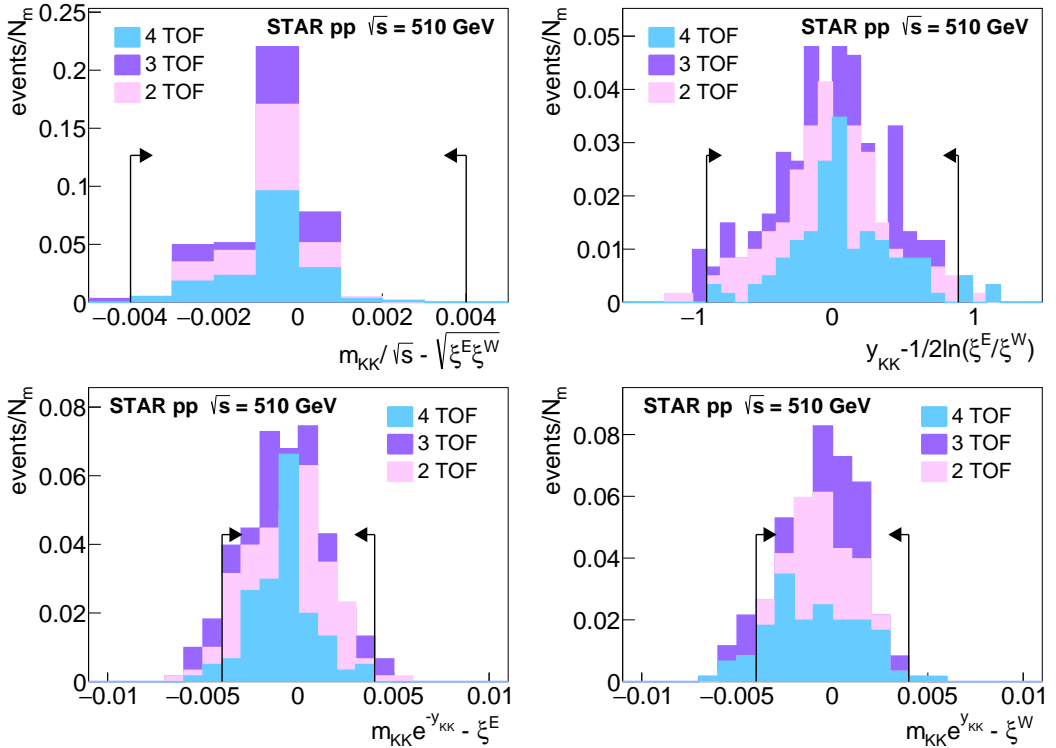


Figure 37: Distribution of the kinematic correlations with indicated SC 7

cut	$N_{\text{TOF}}^{\text{tracks}}$	N_p	$u(N_p)$	N_n	$u(N_n)$	ε	$u(\varepsilon)$
$m_{KK}/\sqrt{s} - \sqrt{\xi^W \xi^E}$ (SC 7.1)	4	104	10.198	500	22.361	0.172	0.015
	3	245	15.652	359	18.947	0.406	0.020
	2	183	13.528	421	20.518	0.303	0.019
$y_{KK} - 1/2 \ln(\xi^E/\xi^W)$ (SC 7.2)	4	87	9.327	517	22.738	0.144	0.014
	3	210	14.491	394	19.849	0.348	0.019
	2	148	12.166	456	21.354	0.245	0.018
$m_{KK}/\sqrt{s} e^{\pm y_{KK}} - \xi^{W(E)}$ (SC 7.3)	4	107	10.344	497	22.293	0.177	0.016
	3	248	15.748	356	18.868	0.411	0.020
	2	186	13.638	418	20.445	0.308	0.019

Table 4: The number of events that passed the selection criterion on N_p or did not pass the criterion on N_n according to SC 7, with the calculated efficiency and uncertainty for different values of $N_{\text{TOF}}^{\text{tracks}}$.

was fitted with a linear function. The number of the kaons was taken as an integral of the Gaussian, $N = A\sigma\sqrt{2\pi}$, where A denoted the amplitude, and σ the width of the Gaussian fit. The uncertainty for N is $u(N) = u(A)N/A$, where uncertainty on the amplitude $u(A)$ was taken from the fit. The uncertainty on the efficiency $u(\varepsilon)$ was calculated as:

$$u(\varepsilon) = \frac{\sqrt{(N_K^{1\text{TOF}} \cdot u(N_K^{2\text{TOF}}))^2 + (N_K^{2\text{TOF}} \cdot u(N_K^{1\text{TOF}}))^2}}{N_K^{1\text{TOF}} + N_K^{2\text{TOF}}} \quad (35)$$

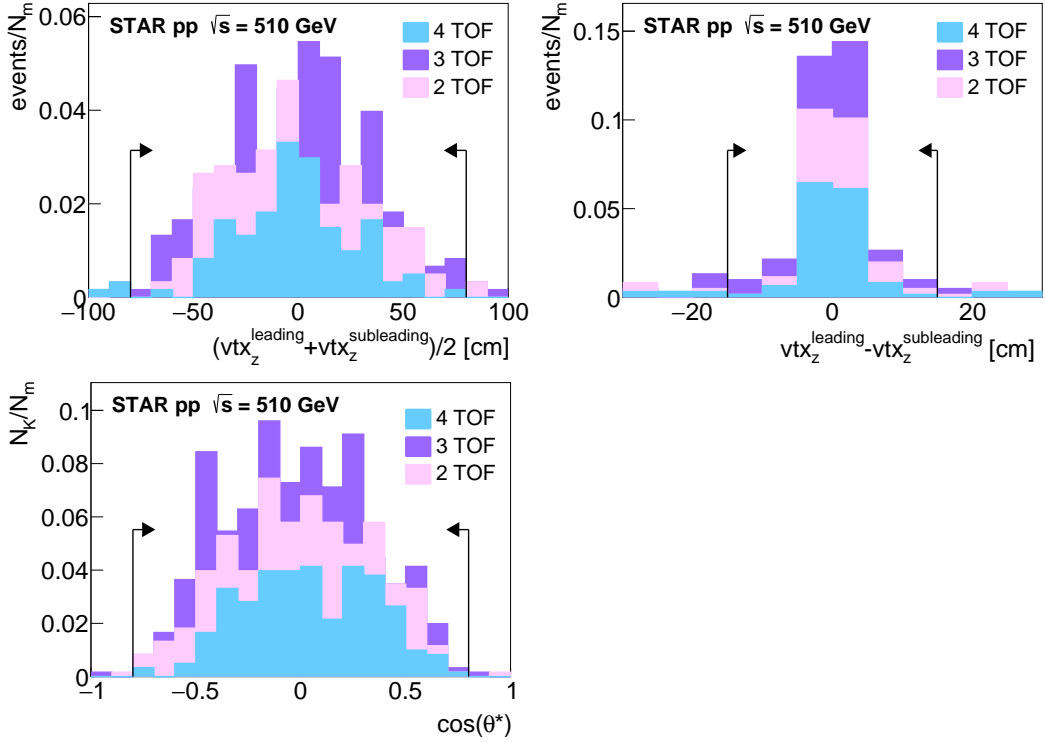


Figure 38: Distribution of the mean (top left) and the difference (top right) of the z position of the K_S^0 decay vertices with applied SC 8. The bottom left plot presents the distribution of θ^* with applied SC 9.

cut	$N_{\text{TOF}}^{\text{tracks}}$	N_p	$u(N_p)$	N_n	$u(N_n)$	ε	$u(\varepsilon)$
$\frac{1}{2}(vtx_z^{\text{leading}} + vtx_z^{\text{subleading}})$ (SC 8.1)	4	104	10.198	500	22.361	0.172	0.015
	3	245	15.652	359	18.947	0.406	0.020
	2	183	13.528	421	20.518	0.303	0.019
$vtx_z^{\text{leading}} - vtx_z^{\text{subleading}}$ (SC 8.2)	4	87	9.327	517	22.738	0.144	0.014
	3	210	14.491	394	19.849	0.348	0.019
	2	148	12.166	456	21.354	0.245	0.018
$\cos(\theta^*)$ (SC 9)	4	107	10.344	497	22.293	0.177	0.016
	3	248	15.748	356	18.868	0.411	0.020
	2	186	13.638	418	20.445	0.308	0.019

Table 5: The number of events that pass selection criterion on N_p or does not pass on N_n , SC 8 and SC 9, with the calculated efficiencies and uncertainties for different values of $N_{\text{TOF}}^{\text{tracks}}$.

The efficiency as a function of the transverse momentum of the probe was determined in the range $0.2 \leq p_T^{\text{probe}} < 1.2$ GeV. Figures 40 and 41 present the distributions of the invariant mass for different ranges of the p_T^{probe} , respectively, for the data and MC. The numerical values of the number of kaons, efficiencies, and their

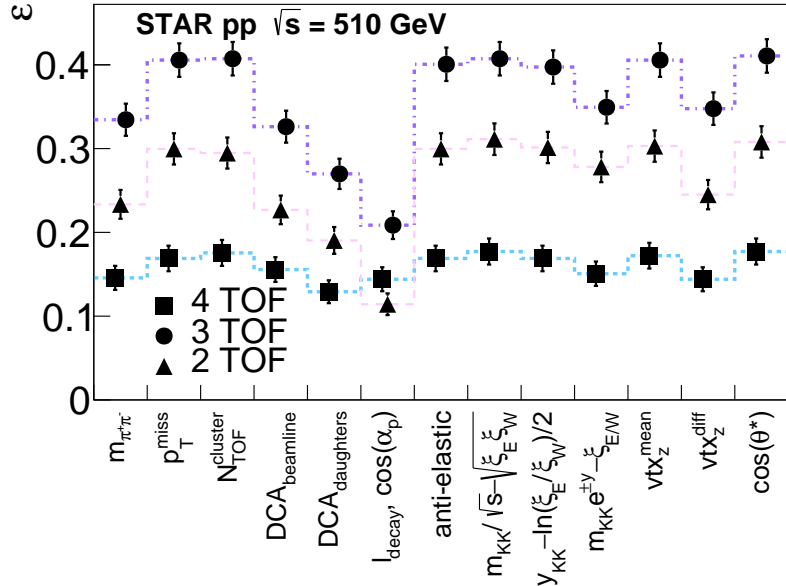


Figure 39: The efficiency ε of the selection criteria for high-quality global tracks matched with the true-level decay products of the K_S^0 formed in CEP for different numbers of tracks with TOF hit among the matched tracks.

uncertainties were summarized in Tables 6 and 7.

The efficiency as a function of the pseudorapidity of the probe was obtained for $-0.9 \leq \eta^{\text{probe}} < 0.9$. The invariant mass distributions for different ranges of the η^{probe} are presented in Figs. 42 and 43 for the data and MC, respectively. The numerical values of the number of kaons, efficiency, and uncertainties are listed in Tables 8 and 9 for the data and MC, respectively.

Finally, the efficiency was calculated as a function of time expressed as the fill number of the RHIC collider. The plots in Figs. 44 and 45 present the invariant mass distributions of the pion pairs for the Data and MC for different fill number ranges. The numerical summary of the number of the kaons and the efficiencies in a given range is presented in Tables 10 and 11.

The tag-and-probe method was compared with the efficiency estimated based on the true-level MC. For that method, the efficiency was calculated for the tracks fulfilling the condition of good quality TPC tracks that are matched with true-level pions based on the matching in $\eta - \phi$ space, requiring $\delta < 0.15$ (for the matching procedure, see Sec. 3.2). The efficiency was calculated for the true region of the production vertex of the pion defined by:

- longitudinal vertex position $|vtx_z^{\text{true}}| < 80$ cm,
- transverse vertex position $vtx_R^{\text{true}} < 3$ cm.

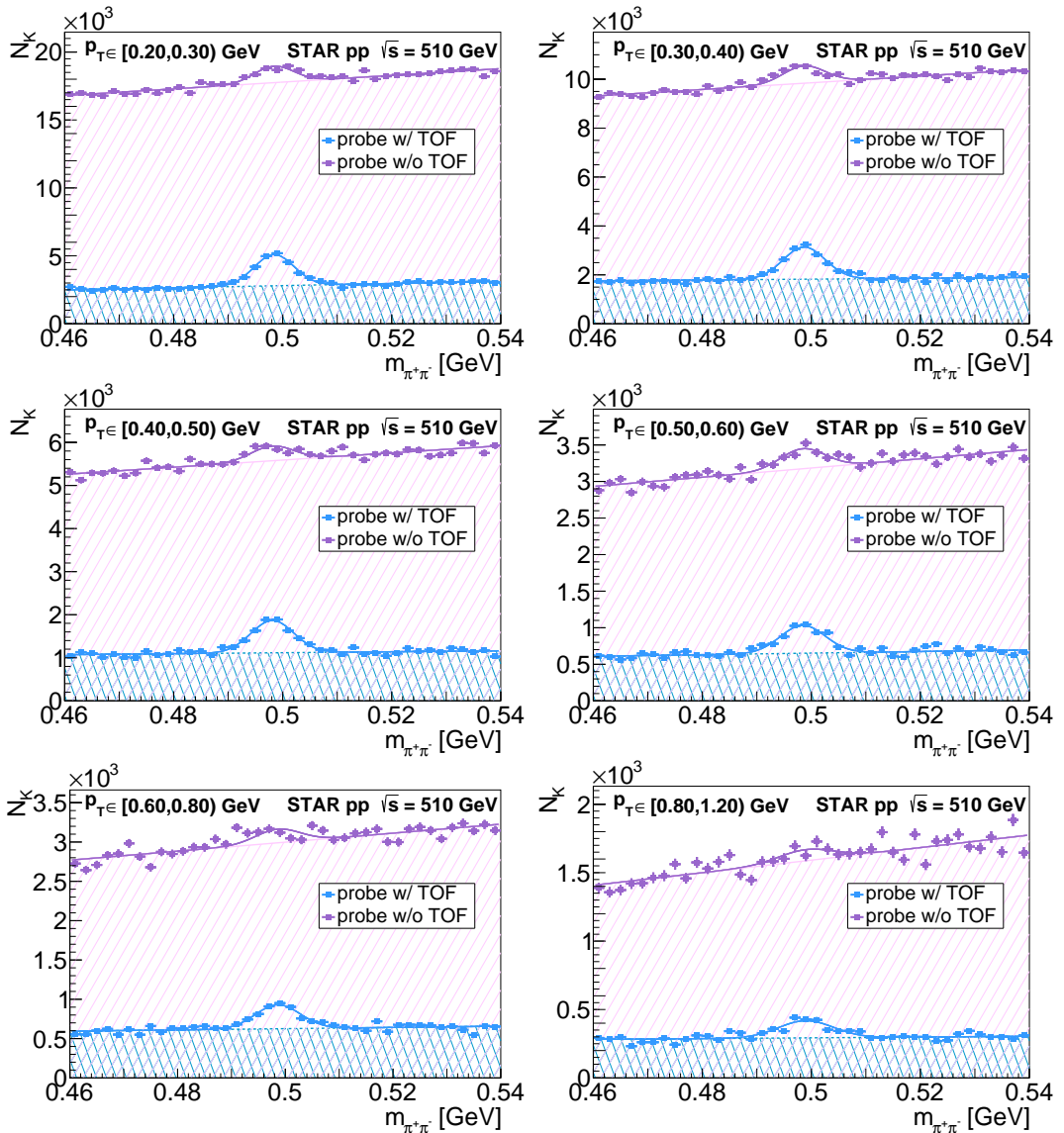


Figure 40: Invariant mass distributions of the $\pi^+\pi^-$ pairs for $0.2 \leq p_T^{\text{probe}} < 1.2 \text{ GeV}$ for the data. The signal is fitted with a Gaussian function, and the background is modelled with a linear function.

p_T [GeV]	$N_K^{2\text{TOF}}$	$u(N_K^{2\text{TOF}})$	$N_K^{1\text{TOF}}$	$u(N_K^{1\text{TOF}})$	ε	$u(\varepsilon)$
[0.2, 0.3)	21.101	0.443	11.094	0.760	0.655	0.016
[0.3, 0.4)	12.727	0.360	6.853	0.572	0.650	0.020
[0.4, 0.5)	7.408	0.279	3.369	0.444	0.687	0.029
[0.5, 0.6)	3.944	0.211	2.835	0.347	0.582	0.032
[0.6, 0.8)	3.183	0.209	1.804	0.336	0.638	0.046
[0.8, 1.2)	1.584	0.164	1.030	0.274	0.606	0.068

Table 6: Number of K_S^0 candidates with two, $N_K^{2\text{TOF}}$, and one, $N_K^{1\text{TOF}}$, hit in TOF, and efficiencies ε with uncertainties for different ranges of the p_T^{probe} for the data.

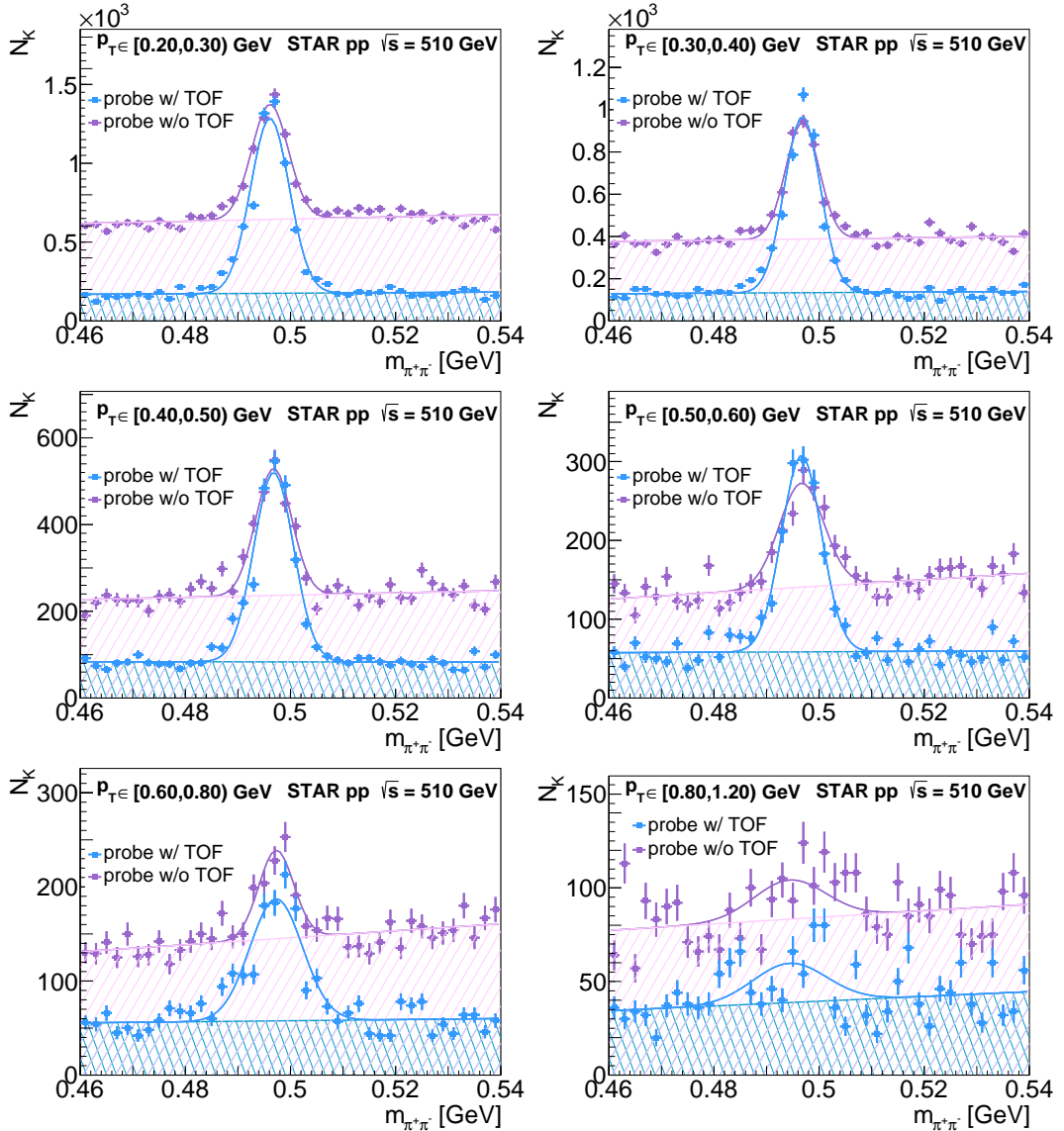


Figure 41: Invariant mass distributions of the $\pi^+\pi^-$ pairs for $0.2 \leq p_T^{\text{probe}} < 1.2 \text{ GeV}$ for the MC. The signal is fitted with a Gaussian function, and the background is modelled with a linear function.

p_T [GeV]	$N_K^{2\text{TOF}}$	$u(N_K^{2\text{TOF}})$	$N_K^{1\text{TOF}}$	$u(N_K^{1\text{TOF}})$	ε	$u(\varepsilon)$
[0.2, 0.3)	10.237	0.215	6.359	0.225	0.617	0.010
[0.3, 0.4)	7.103	0.178	4.386	0.178	0.618	0.011
[0.4, 0.5)	4.150	0.136	2.504	0.133	0.624	0.015
[0.5, 0.6)	2.365	0.104	1.400	0.106	0.628	0.020
[0.6, 0.8)	1.623	0.099	0.783	0.093	0.674	0.029
[0.8, 1.2)	0.368	0.063	0.357	0.086	0.507	0.074

Table 7: Number of K_S^0 candidates with two, $N_K^{2\text{TOF}}$, and one, $N_K^{1\text{TOF}}$, hit in TOF, and efficiencies, ε , with uncertainties for different ranges of the p_T^{probe} for the MC.

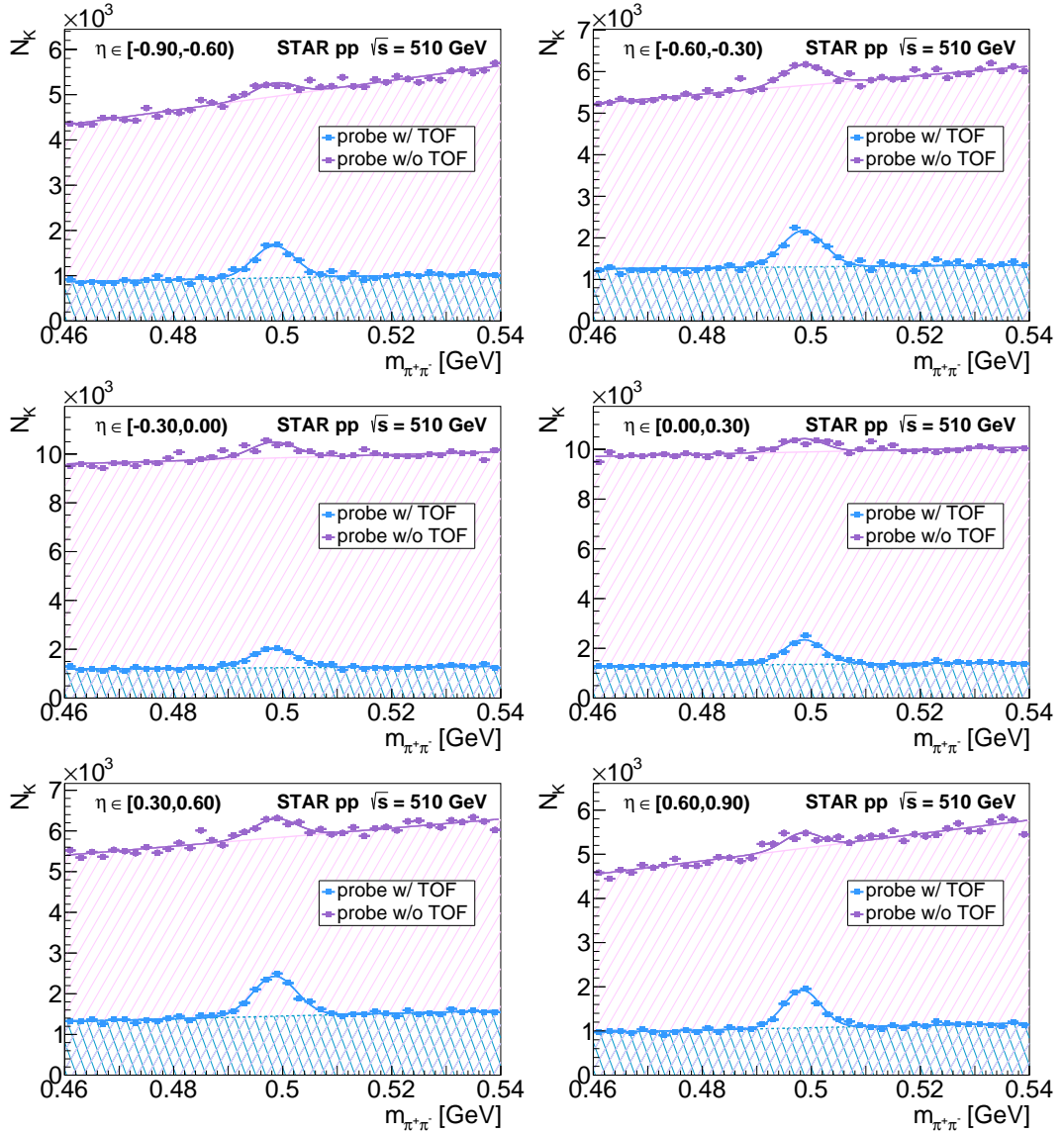


Figure 42: Invariant mass distributions of the $\pi^+\pi^-$ pairs for $-0.9 \leq \eta < 0.9$ for the data. The signal is fitted with a Gaussian function, and the background is modelled with a linear function.

η	$N_K^{2\text{TOF}}$	$u(N_K^{2\text{TOF}})$	$N_K^{1\text{TOF}}$	$u(N_K^{1\text{TOF}})$	ε	$u(\varepsilon)$
[-0.9, -0.6)	6.790	0.260	2.848	0.411	0.704	0.031
[-0.6, -0.3)	8.560	0.301	4.910	0.449	0.635	0.023
[-0.3, 0.0)	8.274	0.301	6.894	0.615	0.545	0.024
[0.0, 0.3)	9.150	0.311	4.932	0.566	0.650	0.027
[0.3, 0.6)	9.894	0.321	4.705	0.461	0.678	0.023
[0.6, 0.9)	7.320	0.264	3.023	0.389	0.708	0.028

Table 8: Number of K_S^0 candidates with two, $N_K^{2\text{TOF}}$, and one, $N_K^{1\text{TOF}}$, hit in TOF, and efficiencies, ε , with uncertainties for different ranges of η^{probe} for the data.

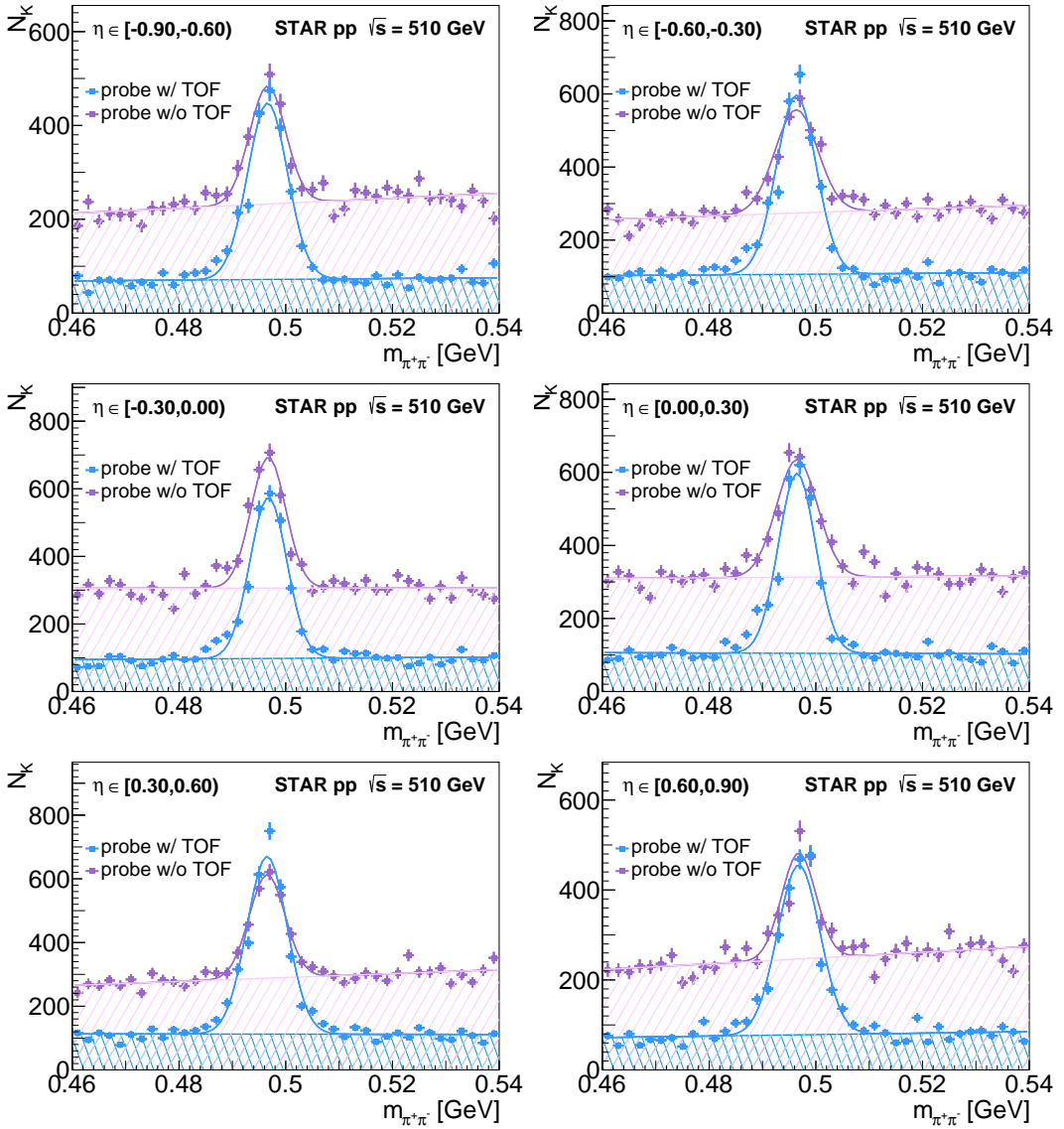


Figure 43: Invariant mass distributions of the $\pi^+\pi^-$ pairs for $-0.9 \leq \eta < 0.9$ for the MC. The signal is fitted with a Gaussian function, and the background is modelled with a linear function.

η	$N_K^{2\text{TOF}}$	$u(N_K^{2\text{TOF}})$	$N_K^{1\text{TOF}}$	$u(N_K^{1\text{TOF}})$	ε	$u(\varepsilon)$
$[-0.9, -0.6)$	3.517	0.124	2.139	0.132	0.622	0.017
$[-0.6, -0.3)$	4.586	0.148	2.845	0.156	0.617	0.015
$[-0.3, 0.0)$	4.128	0.139	3.156	0.153	0.567	0.014
$[0.0, 0.3)$	4.305	0.144	3.112	0.162	0.580	0.015
$[0.3, 0.6)$	5.274	0.155	2.736	0.145	0.658	0.014
$[0.6, 0.9)$	3.757	0.131	1.893	0.129	0.665	0.017

Table 9: Number of the K_S^0 candidates with two, $N_K^{2\text{TOF}}$, and one, $N_K^{1\text{TOF}}$, hit in TOF, and efficiencies, ε , with uncertainties for different ranges of η^{probe} for the MC.

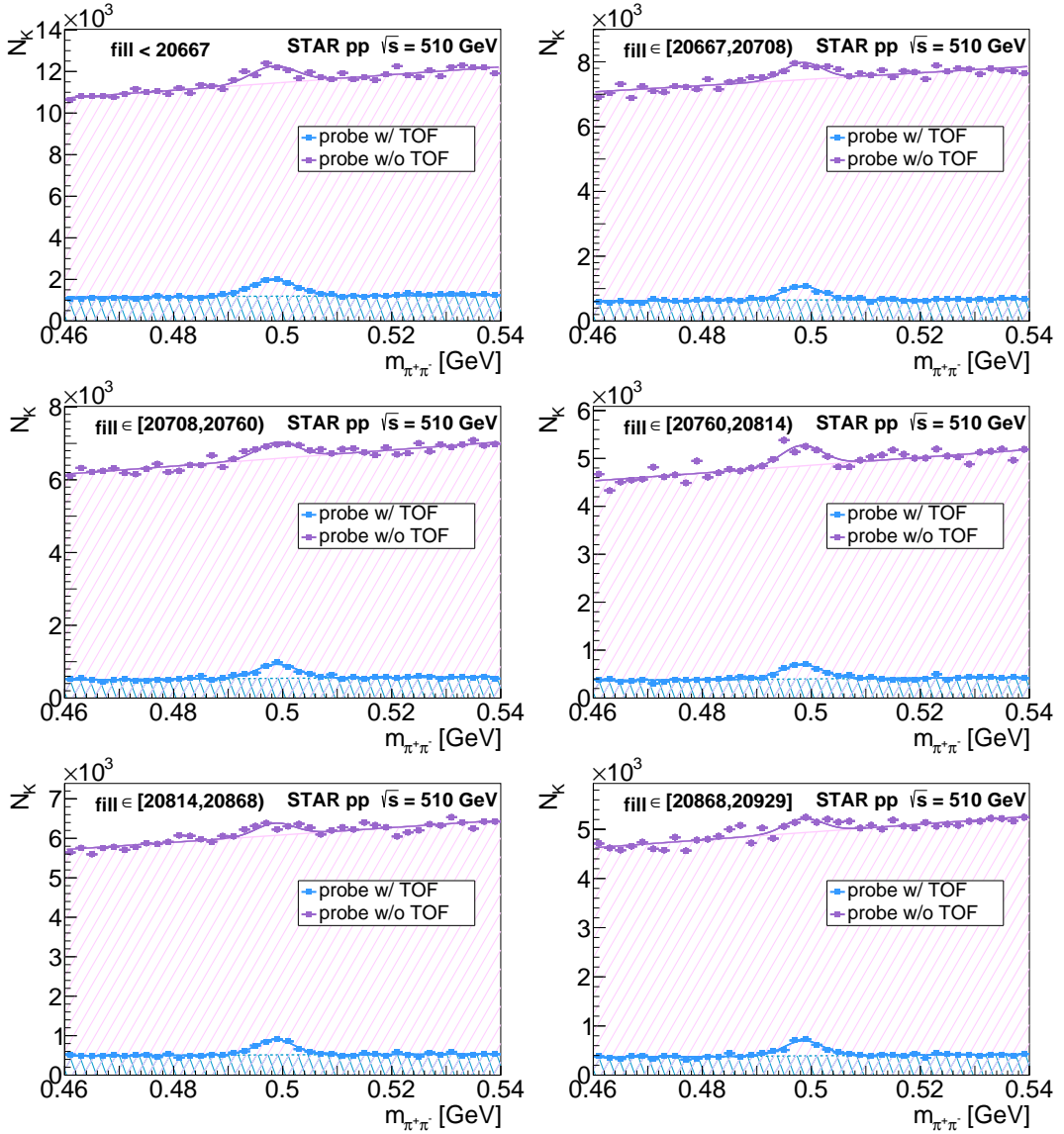


Figure 44: Invariant mass distributions of the $\pi^+\pi^-$ pairs in different ranges of the fill number for the data. The signal was fitted with a Gaussian function and the background with a linear function.

fill	$N_K^{2\text{TOF}}$	$u(N_K^{2\text{TOF}})$	$N_K^{1\text{TOF}}$	$u(N_K^{1\text{TOF}})$	ε	$u(\varepsilon)$
< 20667	8.373	0.298	8.665	0.663	0.491	0.021
[20667, 20708)	3.751	0.202	4.698	0.483	0.444	0.029
[20708, 20760)	3.693	0.200	4.265	0.474	0.464	0.031
[20760, 20814)	2.870	0.175	4.100	0.410	0.412	0.028
[20814, 20868)	3.453	0.180	2.738	0.429	0.558	0.041
[20868, 20929)	2.758	0.167	2.523	0.392	0.522	0.042

Table 10: Number of the kaons with two TOF $N_K^{2\text{TOF}}$, one $N_K^{1\text{TOF}}$ hit in TOF, and efficiencies ε with uncertainties for different ranges of fill number for the data

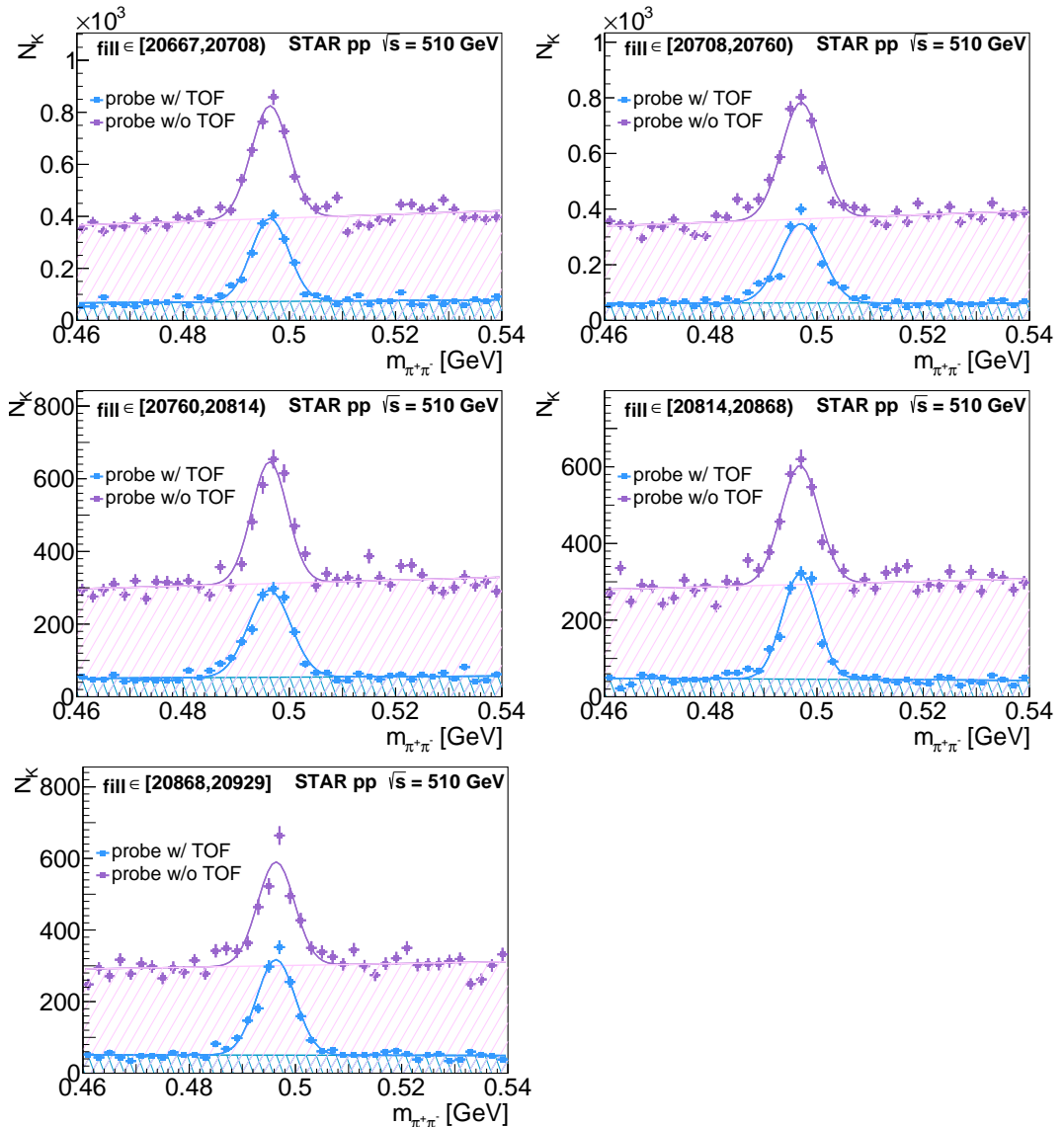


Figure 45: Invariant mass distributions of the $\pi^+\pi^-$ pairs in different ranges of the fill number for the MC. The signal was fitted with a Gaussian function and the background with a linear function.

fill	$N_K^{2\text{TOF}}$	$u(N_K^{2\text{TOF}})$	$N_K^{1\text{TOF}}$	$u(N_K^{1\text{TOF}})$	ε	$u(\varepsilon)$
[20667, 20708)	2.839	0.167	3.845	0.392	0.425	0.015
[20708, 20760)	2.869	0.114	3.889	0.174	0.425	0.015
[20760, 20814)	2.391	0.117	2.815	0.179	0.459	0.017
[20814, 20868)	2.295	0.104	2.785	0.146	0.452	0.017
[20868, 20929)	2.423	0.100	2.527	0.151	0.489	0.019

Table 11: Number of the kaons with two TOF $N_K^{2\text{TOF}}$, one $N_K^{1\text{TOF}}$ hit in TOF, and efficiencies ε with uncertainties for different ranges of fill number for the MC.

The efficiency was calculated as the ratio of the pions with TOF hit to all pions fulfilling the above requirements:

$$\varepsilon = \frac{N_\pi^{\text{TOF}}}{N_\pi^{\text{TOF}} + N_\pi^{\text{no TOF}}}, \quad (36)$$

where N_π^{TOF} denotes pion with hit in the TOF detector, while $N_\pi^{\text{no TOF}}$ without.

Figure 46 presents the distribution of the pion transverse momentum with and without hit in TOF. Tab. 12.

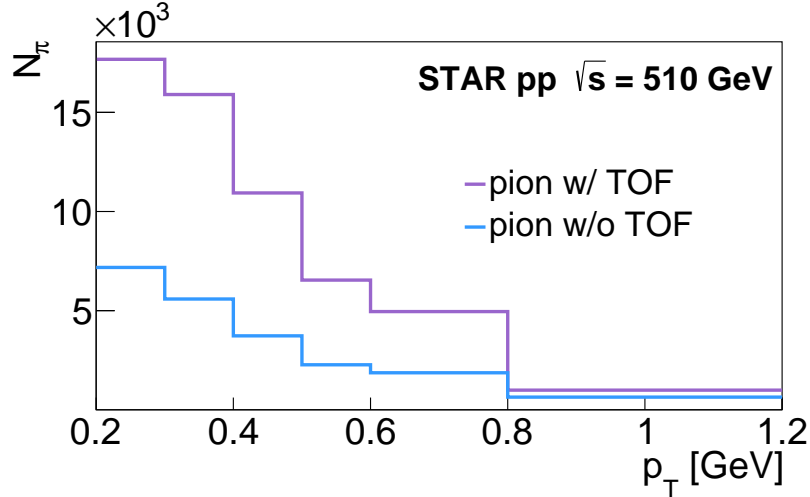


Figure 46: Distributions of the pion transverse momentum with and without hit in the TOF detector for the true-level MC efficiency.

p_T [GeV]	N_π^{TOF}	$u(N_\pi^{\text{TOF}})$	$N_\pi^{\text{no TOF}}$	$u(N_\pi^{\text{no TOF}})$	ε	$u(\varepsilon)$
[0.2, 0.3)	17675	132.947	7179	84.729	0.711	0.003
[0.3, 0.4)	15899	126.091	5587	74.746	0.740	0.003
[0.4, 0.5)	10936	104.575	3729	61.066	0.746	0.004
[0.5, 0.6)	6541	80.876	2270	47.645	0.742	0.005
[0.6, 0.8)	4953	70.378	1867	43.209	0.726	0.005
[0.8, 1.2)	991	31.480	639	25.278	0.608	0.012

Table 12: Number of pions with a TOF hit N_π^{TOF} , without a TOF hit $N_\pi^{\text{no TOF}}$, and efficiencies ε with calculated uncertainties for different ranges of the transverse momentum of the pion for the true-level MC efficiency.

The results for pseudorapidity are presented in Fig. 47 and Tab. 13. Uncertainties for the number of the pions N were taken as $u(N) = \sqrt{N}$, and the uncertainty on the efficiency ε was calculated from the Eq. (35).

Figures 48–50 present the compared efficiencies obtained for the transverse momentum, pseudorapidity, and the fill number. The true level efficiency is higher for the p_T and η compared to the tag-and-probe method for the detector-level MC. The average values are similar for the p_T and η ; however, for the fill number efficiency, we obtained significantly lower values of the efficiency.

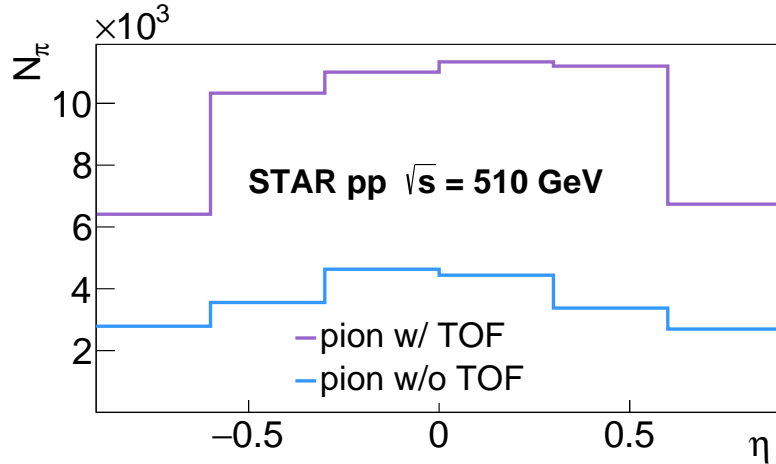


Figure 47: The distribution of the pion pseudorapidity with and without a hit in the TOF detector for the true-level MC efficiency.

η	N_π^{TOF}	$u(N_\pi^{\text{TOF}})$	$N_\pi^{\text{no TOF}}$	$u(N_\pi^{\text{no TOF}})$	ε	$u(\varepsilon)$
[-0.9, -0.6)	6412	80.075	2788	52.802	0.697	0.005
[-0.6, -0.3)	10330	101.637	3556	59.632	0.744	0.004
[-0.3, 0.0)	11010	104.929	4632	68.059	0.704	0.004
[0.0, 0.3)	11342	106.499	4439	66.626	0.719	0.004
[0.3, 0.6)	11205	105.854	3375	58.095	0.769	0.003
[0.6, 0.9)	6737	82.079	2696	51.923	0.714	0.005

Table 13: Number of the pion with TOF N_π^{TOF} , without TOF $N_\pi^{\text{no TOF}}$, and efficiencies ε with calculated uncertainties for different ranges of the pseudorapidity of the pion for the true-level MC efficiency.

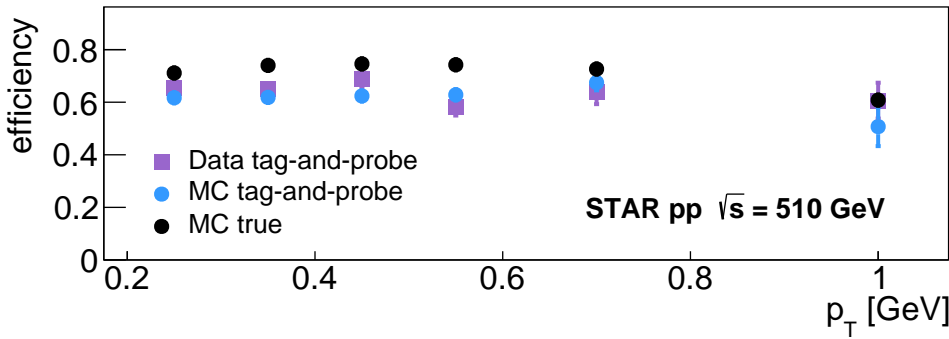


Figure 48: Efficiency of the TOF detector as a function of the transverse momentum. Calculated with the tag-and-probe method for the data and detector-level MC, compared with true-level MC detector efficiency.

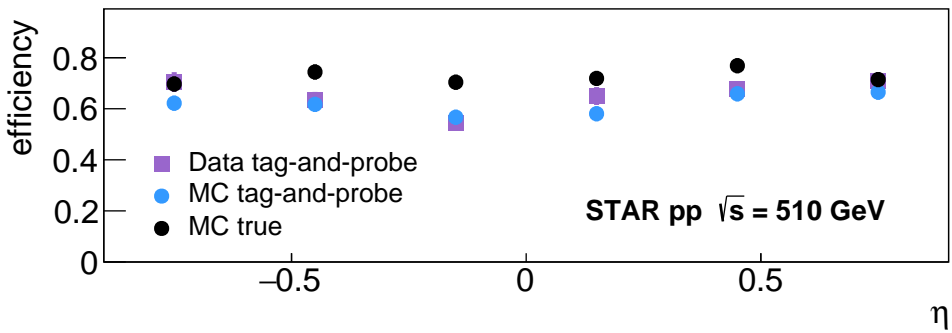


Figure 49: Efficiency of the TOF detector as a function of the pseudorapidity. Calculated with the tag-and-probe method for the data and detector-level MC, compared with true-level MC detector efficiency.

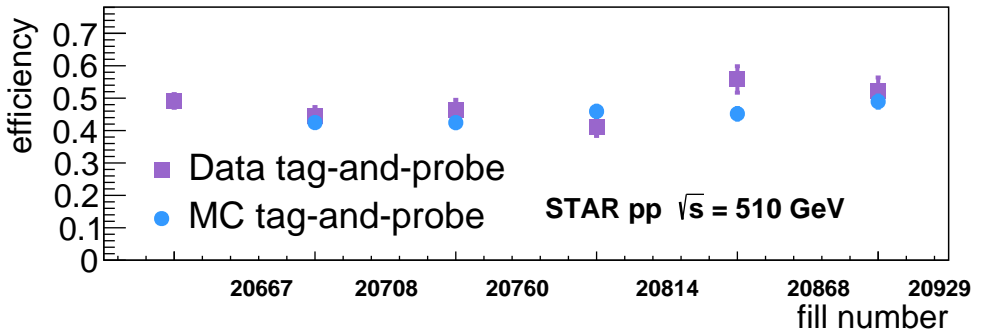


Figure 50: Efficiency of the TOF detector as a function of the time, which is based on the accelerator fill number, calculated for the data and detector-level MC with the tag-and-probe method.

3.4 Physics results for the $K_S^0\bar{K}_S^0$ pair production

The outcomes for different $N_{\text{TOF}}^{\text{tracks}}$ were merged. Figure 51 presents the invariant mass of the $K_S^0\bar{K}_S^0$ after applying all selection criteria outlined and explained in Sec. 3.1. The Dime MC contains only non-resonant continuum production. The data reveals the presence of a resonance. The resonance was fitted with the Gaussian function, while the background was modelled with the linear function. The continuum non-resonant production of the $K_S^0\bar{K}_S^0$ pairs predicted by Dime MC is also shown. The MC is scaled to the data for the $m_{\text{KK}} \geq 1.8$ GeV. The data-to-MC ratio is equal to 0.58 ± 0.16 . The mean value of the Gaussian fit, i.e., the mass of the resonance, equals $m_{\text{KK}} = 1.69 \pm 0.08$ GeV. The possible candidate is the resonance $f_0(1710)$, which isospin and C-parity $J^{PC} = 0^{++}$ is in agreement with the $K_S^0\bar{K}_S^0$ quantum numbers. The PDG mass of the resonance is $m_f = 1.704 \pm 0.012$ GeV. The relative difference $(m_{\text{KK}} - m_f)/m_f = -0.008 \pm 0.047$.

The $K_S^0\bar{K}_S^0$ pair pseudorapidity distribution is shown in Fig. 52(left). The vast majority of the data is concentrated around the $\eta = 0$, meaning the centrally produced particle was moving in the vertical direction in the laboratory reference frame. The MC prediction follows the shape of the data. The transverse momentum of the $K_S^0\bar{K}_S^0$ is shown in Fig. 52(right). The invariant mass distributions of the $K_S^0\bar{K}_S^0$ pairs for two configurations of the scattered protons, opposite signs and the same signs of

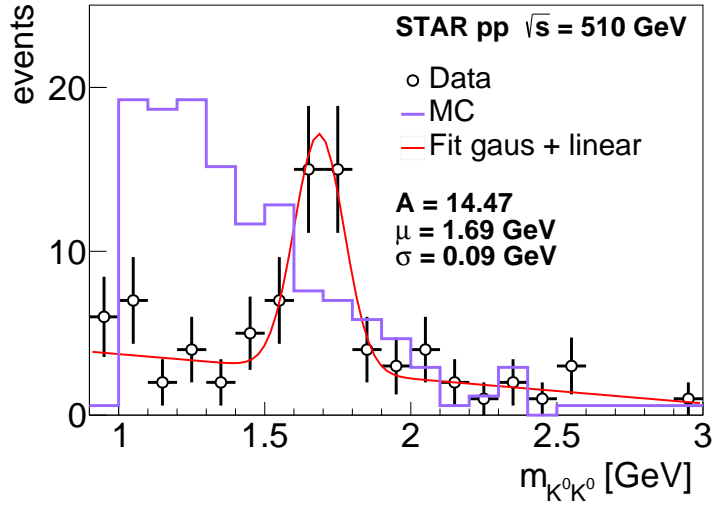


Figure 51: Distribution of the invariant mass of $K_S^0 \bar{K}_S^0$ pairs. The MC is scaled for the $m_{KK} \geq 1.8$ GeV. The data-to-MC ratio is equal to 0.58 ± 0.16 .

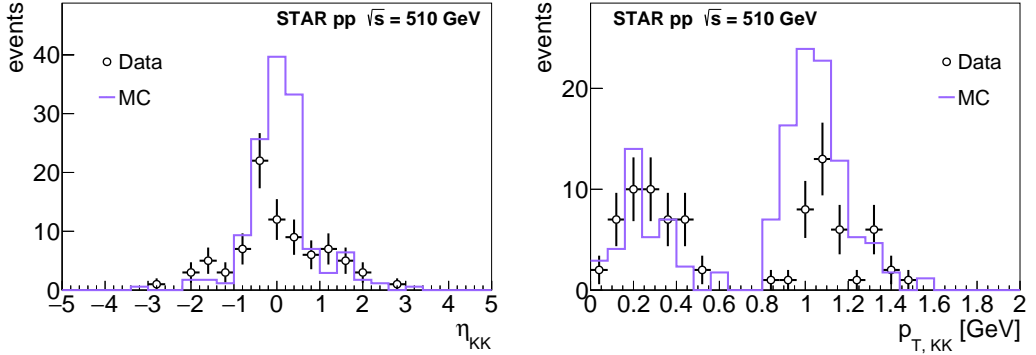


Figure 52: Distributions of pseudorapidity (left) and transverse momentum (right) of $K_S^0 \bar{K}_S^0$ pairs. The MC is normalized to the data with the same factor as in Fig. 51.

the y -components of momenta, are shown in Fig. 53. The distribution shows a two-peak structure coming from the events with the protons of the same and the opposite sign of the y component of the momentum. For the data, the peak for the protons with the same sign of the y -component of the momentum is around the $p_T = 1.3$ GeV, while for the protons with the opposite sign of the y -component of the momentum, it is around 0.3 GeV. The MC is normalized to the data with the same factor as in Fig. 51. The MC distributions follow the shape of the data, but the values of the peaks are shifted toward the lower values. After all selection criteria are applied, the distributions for individual K_S^0 mesons forming the centrally produced pairs are presented in Fig. 54. The invariant mass distribution fit indicates that the mean values lie close to the actual values of the K_S^0 meson. The relative difference between fitted mass $m_K = 497.553 \pm 3.877$ MeV, and the PDG mass $m_{K,\text{PDG}} = 497.614 \pm 0.024$ MeV equal $(m_K - m_{K,\text{PDG}})/m_K = -0.0001 \pm 0.0078$. The maximum in the distribution of the transverse momentum is attained for around $p_T = 0.8$ MeV, and the distribution

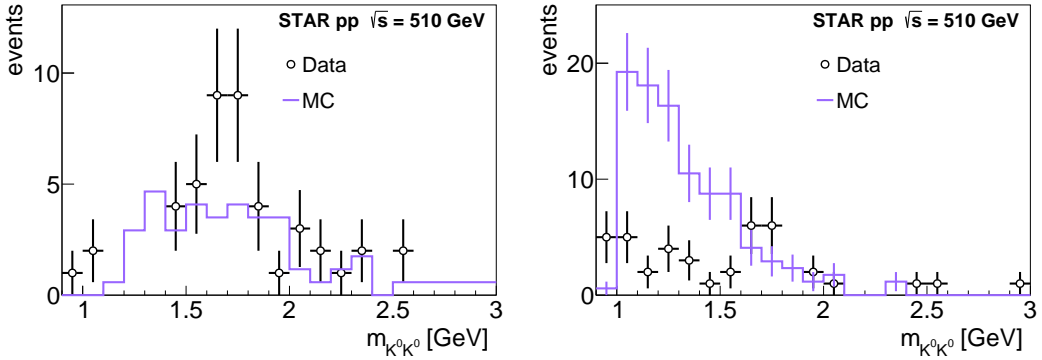


Figure 53: Distributions of the invariant mass of $K_S^0 \bar{K}_S^0$ pairs: events with protons with the opposite signs of the y -component of the momentum (left), and events with the same sign of the y -component of the momentum (right). The MC is normalized to the data with the same factor as in Fig. 51.

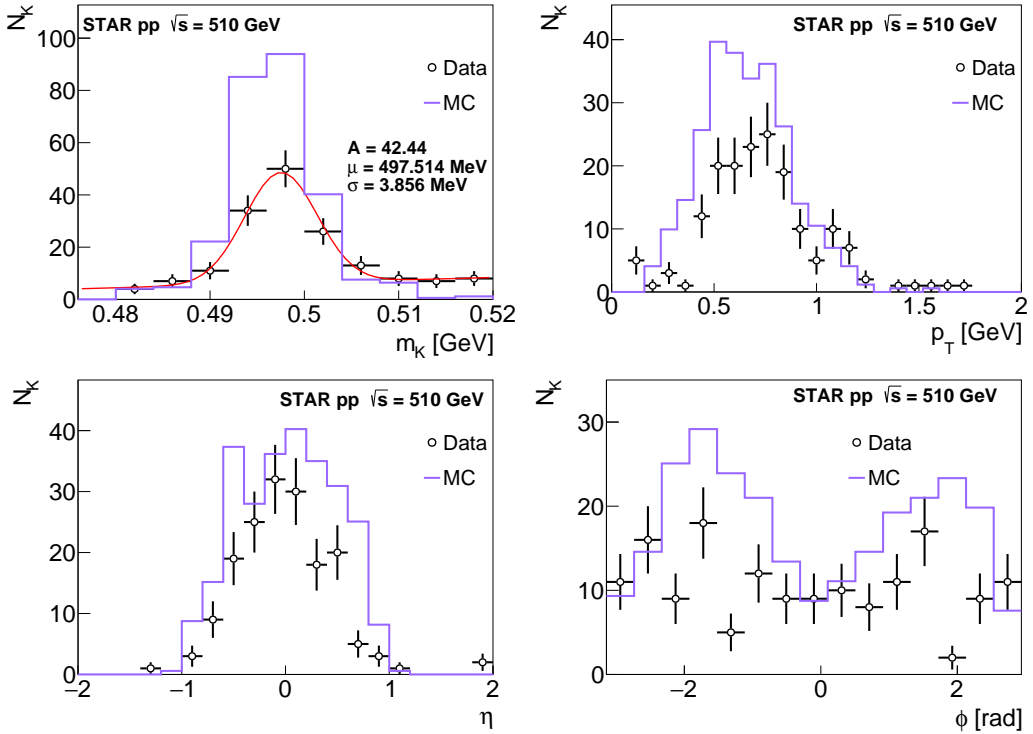


Figure 54: Invariant mass (top left), transverse momentum (top right), pseudorapidity (bottom left), and azimuthal angle (bottom right) of the K_S^0 . The MC predictions are normalized to the data with the same factor as in Fig. 51.

of the MC follows the data shape. The same normalization factor as above is used in all plots in Fig. 54. The pseudorapidity lies mostly within the range $|\eta| < 1.0$. The azimuthal angle ϕ reveals that we detect fewer events around the $\phi = 0$ relates to the detector acceptance.

3.5 The $\Lambda^0\bar{\Lambda}^0$ pair production

A similar analysis was conducted for the $\Lambda^0\bar{\Lambda}^0$ pair production. Due to a more demanding environment, only events with $N_{\text{TOF}}^{\text{tracks}} = 4$ and 3 were considered. Information on the particle ID was included, which increased the complexity of the analysis code. As for the $K_S^0\bar{K}_S^0$ pairs, the tracks should hold a total charge equal to zero or ± 1 , respectively, for $N_{\text{TOF}}^{\text{tracks}} = 4$ and 3. The primarily divided tracks into matched and not matched with a TOF hit were further subdivided into protons, potential pions (protons that might be pions), and pions using the information on the ionization energy losses, dE/dx in TPC. For the particle identification we use the quantity $n\sigma_x$, given by the formula:

$$n\sigma_x = \ln \left[\frac{(dE/dx)}{(dE/dx)_X^{\text{exp}}} \right] / \sigma_{dE/dx} \quad (37)$$

where (dE/dx) is the ionization energy loss of the TPC track, $(dE/dx)_X^{\text{exp}}$ is the Bichsel [56] expectation for a given particle type ($X = \pi, K, p, \dots$), and $\sigma_{dE/dx}$ is the relative statistical uncertainty of reconstructed (dE/dx) . In this analysis, as a proton, we understand a track with $n\sigma_p < 2.0$. If that track additionally fulfils the cut $n\sigma_\pi < 3.0$, it can also be considered as a pion. If the tracks do not fulfil the proton hypothesis and has $n\sigma_\pi < 3.0$, the track is classified as a pion. If a track with the TOF hit does not qualify to be a proton or a pion, the event is dismissed.

Let us sketch the process of finding appropriate TPC tracks for the $N_{\text{TOF}}^{\text{tracks}} = 4$. In the first place, we demand that at least two tracks should pass the proton hypothesis. If the number of the protons $N_{\text{protons}} = 2$, the protons tracks should be of the opposite sign, and the remaining TOF-matched tracks should be classified as pions. If the $N_{\text{protons}} = 3$, at least one of those protons must also be classified as a pion, while for the $N_{\text{protons}} = 4$, at least two protons need to be consistent with the pion hypothesis. If multiple combinations are present, the ambiguity is resolved by finding the lowest distance to the mass of the Λ^0 baryon from the PDG. A similar approach was taken for the $N_{\text{TOF}}^{\text{tracks}} = 3$, where more combinations needed to be considered due to the necessity of taking a track not matched with the TOF detector.

The first attempt to extract the $\Lambda^0\bar{\Lambda}^0$ pairs resulted in finding only eight events that had low values of the missing transverse momentum $p_T^{\text{miss}} \leq 0.15$ GeV, see Fig. 55(right). In the search for $\Lambda^0\bar{\Lambda}^0$ pairs, the selection criteria SC 1-3 used in the $K_S^0\bar{K}_S^0$ pairs analysis remain the same. The remaining cuts need to be adjusted, and they are listed below:

4. Exclusive event selection:

- 4.1 Narrow mass window: $1.1 \leq m_{p^\pm\pi^\mp} \leq 1.23$ GeV.
- 4.2 Missing transverse momentum $p_T^{\text{miss}} \leq 0.15$ GeV
- 4.3 Number of TOF clusters: $N_{\text{TOF}}^{\text{cluster}} \leq 2 \cdot N_{\text{TOF}}^{\text{tracks}} + 1$.

5. Topological selection:

- 5.1 $\text{DCA}_{\text{beamline}} < 5.0$ cm
- 5.2 $\text{DCA}_{\text{daughters}} < 5.0$ cm
- 5.3 $\cos(\alpha_p) \geq 0.925$

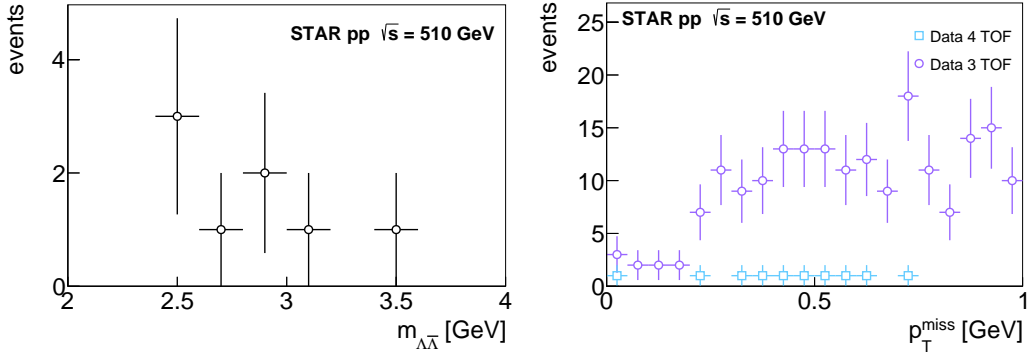


Figure 55: Distributions of the invariant mass (left) and the missing momentum p_T^{miss} (right) of the $\Lambda^0\bar{\Lambda}^0$ pairs.

6. Anti-elastic cuts (no change with respect to the $K_S^0\bar{K}_S^0$ analysis)
7. Kinematic correlation between centrally produced system and intact protons:
 - 7.1 $|m_{\Lambda\Lambda}/\sqrt{s} - \sqrt{\xi^W\xi^E}| \leq 0.01$
 - 7.2 $|y_{\Lambda\Lambda} - 1/2\ln(\xi^E/\xi^W)| \leq 1.0$
 - 7.3 $|m_{\Lambda\Lambda}/\sqrt{s}e^{y_{\Lambda\Lambda}} - \xi^W| \leq 0.01$ and $|m_{\Lambda\Lambda}/\sqrt{s}e^{-y_{\Lambda\Lambda}} - \xi^E| \leq 0.01$.
8. Decay vertex position of the lambda candidate:
 - 8.1 $(\text{vtx}_z^{\text{leading}} + \text{vtx}_z^{\text{subleading}})/2 \leq 80.0$ cm
 - 8.2 $|\text{vtx}_z^{\text{leading}} - \text{vtx}_z^{\text{subleading}}| \leq 50.0$ cm.
9. Angle between p and π momenta in the rest frame of Λ^0 : $|\cos(\theta^*)| \leq 0.8$.

The invariant mass of the $\Lambda^0\bar{\Lambda}^0$ pairs is presented in Fig. 55(left). The distributions of invariant mass, transverse momentum, pseudorapidity, and azimuthal angle of individual Λ^0 baryons constituting the $\Lambda^0\bar{\Lambda}^0$ pairs are shown in Fig. 56.

The $\Lambda^0\bar{\Lambda}^0$ pairs analysis requires further study - the initial code for the analysis has been written that can be further developed to preserve more events, e.g., for $N_{\text{TOF}}^{\text{tracks}} = 4$ preserve the event if one of the tracks is not qualified as a pion or proton and search for an appropriate one among the tracks not matched with the TOF detector.

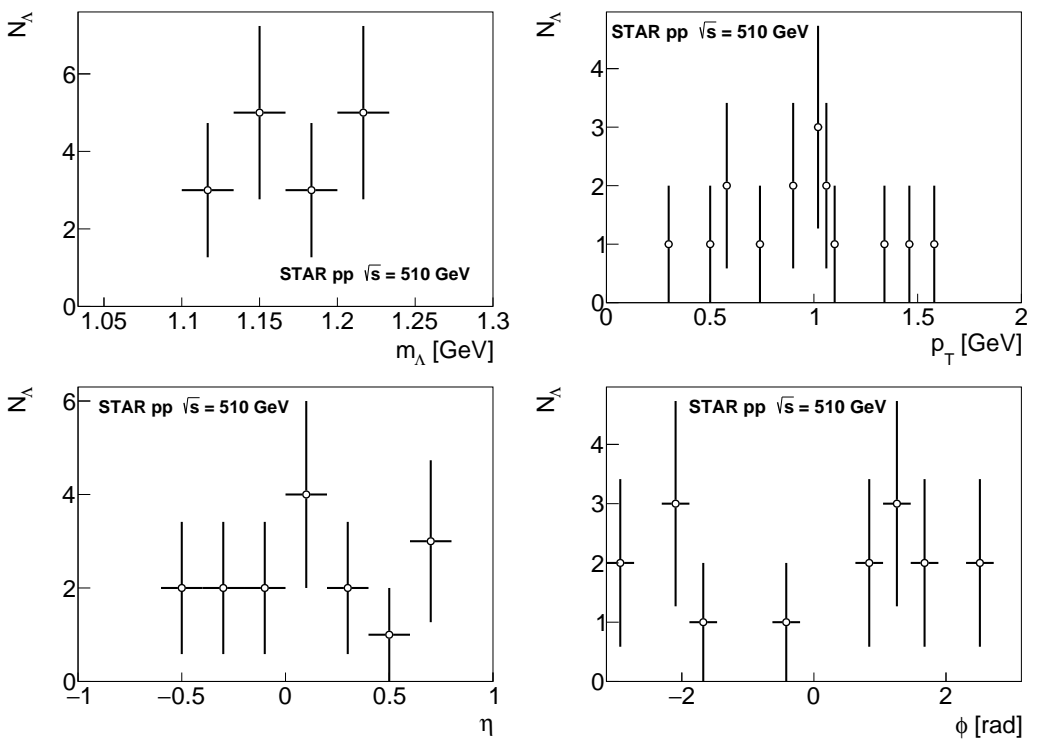


Figure 56: Invariant mass (top left), transverse momentum (top right), pseudorapidity (bottom left), and azimuthal angle (bottom right) of the Λ^0 baryons.

4 Summary

This master thesis was focused on the investigation of the CEP of the $K_S^0\bar{K}_S^0$ or $\Lambda^0\bar{\Lambda}^0$ pairs produced via the DPE mechanism in proton-proton collisions at the centre-of-mass energy $\sqrt{s} = 510$ GeV with the STAR detector at RHIC.

The invariant mass of the $K_S^0\bar{K}_S^0$ pairs clearly shows the presence of resonant and non-resonant production. The observed resonance has the mass nearest to the $f(1710)$, for which $J^{PC} = 0^{++}$ is in agreement with the quantum numbers of the $K_S^0\bar{K}_S^0$ state, and the relative distance between their masses equals $(m_{KK} - m_f)/m_f = -0.008 \pm 0.047$. Other resonances are also possible. However, destructive interference could lead to a lack of experimental observation. Another possible resonance could be $f(980)$, but due to the minimum mass of the $K_S^0\bar{K}_S^0$ pair equal to ~ 1 GeV it cannot be confirmed. For the $\Lambda^0\bar{\Lambda}^0$ pairs production, the number of events is very small in the current analysis. For the low values of the missing momentum, we are left with only eight events, i.e. sixteen lambda particles with mass distribution presented in Fig. 56. The analysis code for either $K_S^0\bar{K}_S^0$ and $\Lambda^0\bar{\Lambda}^0$ pairs production can be used again and further developed to refine the analysis.

The important step was to determine the efficiencies of the selection criteria. The events with four matched TPC tracks with the true level were used in the study. The matching was based on the smallest distance in the $\eta - \phi$ space. In the future, these efficiencies will be used in estimating the differential cross-sections of the exclusive production of the $K_S^0\bar{K}_S^0$ pairs.

Another essential part of that work was related to determining the TOF detector efficiency based on the tag-and-probe method for the data and detector-level MC. The obtained results were compared with the true-level detector efficiency.

Reference

- [1] A. Bettini, Introduction to Elementary Particle Physics, Cambridge University Press, 2014.
- [2] M. Thomson, Modern Particle Physics, Cambridge University Press, 2013.
- [3] https://tikz.net/sm_particles/
- [4] D. H. Perkins, Introduction to High Energy Physics, Cambridge University Press, 2000.
- [5] J. Campbell, J. Huston, F. Krauss, The Black Book of Quantum Chromodynamics, Oxford University Press, 2018.
- [6] Particle Data Group, R.L. Workman et al., Review of Particle Physics, **PTEP** (2022) 083C01.
- [7] S. Donnachie, G. Dosch, P. Landshoff and O. Nachtmann, Pomeron Physics and QCD, Cambridge University Press, 2002.
- [8] V. Barone and E. Predazzi, High Energy Particle Diffraction, Springer, 2002.
- [9] Dime Monte Carlo website <https://dimemc.hepforge.org/>
- [10] L.A. Harland-Lang, V.A. Khoze, M.G. Ryskin, Modeling exclusive meson pair production at hadron colliders, **Eur. Phys. J. C** 74 (2014) 2848, arXiv:1312.4553 [hep-ph].
- [11] R. Brun, F. Bruyant, M. Maire, A.C. McPherson, P. Zanarini, GEANT3, CERN-DD-EE-84-1, 1987.
- [12] OPAL Collaboration, K. Ackerstaff et al., Production of K_S^0 and Λ in quark and gluon jets from Z^0 decay, **Eur. Phys. J. C** 8 (1999) 241, arXiv:hep-ex/9805025.
- [13] OPAL Collaboration, K. Ackerstaff et al., Inclusive production of charged hadrons and K_S^0 mesons in photon-photon collisions, **Eur. Phys. J. C** 6 (1999) 253, arXiv:hep-ex/9808009.
- [14] L3 Collaboration, M. Acciarri et al., $K_S^0 K_S^0$ final state in two-photon collisions and implications for glueballs, **Phys. Lett. B** 501 (2001) 173, arXiv:hep-ex/0011037.
- [15] L3 Collaboration, P. Achard et al., Inclusive π^0 and K_S^0 production in two-photon collisions at LEP, **Phys. Lett. B** 524 (2002) 44, arXiv:hep-ex/0109037.
- [16] ALEPH Collaboration, D. Buskulic et al., Production of K^0 and Λ in hadronic Z decays, **Z. Phys. C** 64 (1994) 361.
- [17] ZEUS Collaboration, S. Chekanov et al., Inclusive $K_S^0 K_S^0$ resonance production in ep collisions at HERA, **Phys. Rev. Lett.** 91 (2008) 112003, arXiv:0806.0807 [hep-ex].

- [18] ZEUS Collaboration, S. Chekanov et al., Measurement of K_S^0 , Λ , $\bar{\Lambda}$ production at HERA, *Eur. Phys. J. C* **51** (2007) 1, arXiv:hep-ex/0612023.
- [19] ZEUS Collaboration, H. Abramowicz et al., Scaled momentum distributions for K_S^0 and $\Lambda/\bar{\Lambda}$ in DIS at HERA, *JHEP* **03** (2012) 020, arXiv:1111.3526 [hep-ex].
- [20] H1 Collaboration, C. Adloff et al., Photoproduction of K^0 and Λ at HERA and a comparison with deep inelastic scattering, *Z. Phys. C* **76** (1997) 213, arXiv:hep-ex/9705018.
- [21] CDF Collaboration, D. Acosta et al., K_S^0 and Λ^0 production studies in $p\bar{p}$ collisions at $\sqrt{s} = 1800$ GeV and 630 GeV, *Phys. Rev. D* **72** (2005) 052001, arXiv:hep-ex/0504048.
- [22] STAR Collaboration, C. Adler et al., Midrapidity Λ and $\bar{\Lambda}$ production in Au+Au collisions at $\sqrt{s_{NN}} = 130$ GeV, *Phys. Rev. Lett.* **89** (2002) 092301, arXiv:nucl-ex/0203016.
- [23] STAR Collaboration, J. Adam et al., Strange hadron production in Au+Au collisions at $\sqrt{s_{NN}} = 7.7, 11.5, 19.6, 27$, and 39 GeV, *Phys. Rev. C* **102** (2020) 034909, arXiv:1906.03732 [nucl-ex].
- [24] PHENIX Collaboration, K. Adcox et al., Measurement of the Λ and $\bar{\Lambda}$ particles in Au+Au collisions at $\sqrt{s_{NN}} = 130$ GeV, *Phys. Rev. Lett.* **89** (2002) 092302, arXiv:nucl-ex/0204007.
- [25] ATLAS Collaboration, G. Aad et al., K_S^0 and Λ production in pp interactions at $\sqrt{s} = 0.9$ and 7 TeV measured with the ATLAS detector at the LHC, *Phys. Rev. D* **85** (2012) 012001, arXiv:1111.1297 [hep-ex].
- [26] ALICE Collaboration, B. Abelev et al., K_S^0 and Λ production in Pb-Pb collisions at $\sqrt{s_{NN}} = 2.76$ TeV, *Phys. Rev. Lett.* **111** (2013) 222301, arXiv:1307.5530 [nucl-ex].
- [27] ALICE Collaboration, S. Acharya et al., Multiplicity dependence of (multi-) strange hadron production in pp collisions at $\sqrt{s} = 13$ TeV, *Eur. Phys. J. C* **80** (2020) 167, arXiv:1908.01861 [nucl-ex].
- [28] ALICE Collaboration, J. Adam et al., Enhanced production of multi-strange hadrons in high-multiplicity pp collisions, *Nature Phys.* **13** (2017) 535, arXiv:1606.07424 [nucl-ex].
- [29] CMS Collaboration, A.M. Sirunyan et al., Strange hadron production in pp and pPb collisions at $\sqrt{s_{NN}} = 5.02$ TeV, *Phys. Rev. C* **101** (2020) 064906, arXiv:1910.04812 [hep-ex].
- [30] CMS Collaboration, V. Khachatryan et al., Multiplicity and rapidity dependence of strange hadron production in pp, pPb, and PbPb collisions at the LHC, *Phys. Lett. B* **768** (2017) 103, arXiv:1605.06699 [nucl-ex].
- [31] NA61/SHINE Collaboration, N. Abgrall et al., Measurements of production properties of K_S^0 mesons and Λ hyperons in proton-carbon interactions at 31 GeV/c, *Phys. Rev. C* **89** (2014) 025205, arXiv:1309.1997 [physics.acc-ph].

- [32] The RHIC accelerator website, <https://www.bnl.gov/rhic/>
- [33] M. Harrison, T. Ludlam, S. Ozaki, RHIC Project Overview, *Nucl. Instrum. Meth. A* 499 (2003) 235–244.
- [34] H. Hahn et al., The RHIC design overview, *Nucl. Instrum. Meth. A* 499 (2003) 245–263.
- [35] A. Zelenski et al., The RHIC polarized source upgrade, 19th International Symposium, SPIN 2010, Juelich, Germany, September 27 – October 2, 2010, *J. Phys. Conf. Ser.* 295 (2011) 012147.
- [36] The STAR detector website <https://www.bnl.gov/rhic/star.php>
- [37] STAR Collaboration, K.H. Ackermann et al., STAR detector overview, *Nucl. Instrum. Meth. A* 499 (2003) 624-632.
- [38] sPHENIX experiments website <https://www.bnl.gov/rhic/phobos-brahms.php>
- [39] The STAR experiment website <https://www.star.bnl.gov/>
- [40] M. Anderson et al., The Star time projection chamber: A Unique tool for studying high multiplicity events at RHIC, *Nucl. Instrum. Meth. A* 499 (2003) 679-691, arXiv: [nucl-ex/0301015](#).
- [41] A. Rose, STAR Integrated Tracker, 13th International Conference on Computing in High-Energy and Nuclear Physics (CHEP 2003), La Jolla, California, March 24-28, 2003, [arXiv:nucl-ex/0307015](#).
- [42] W. J. Llope et al., The TOFp / pVPD time-of-flight system for STAR, *Nucl. Instrum. Meth. A* 522 (2004) 252-273, [arXiv:nucl-ex/0308022](#).
- [43] W. J. Llope, The large-area time-of-flight upgrade for STAR, *Nucl. Instrum. Meth. B* 241 (2005) 306-310.
- [44] F. Geurts et al., Performance of the prototype MRPC detector for STAR, *Nucl. Instrum. Meth. A* 533 (2004) 60-64.
- [45] W. J. Llope et al., The STAR Vertex Position Detector, *Nucl. Instrum. Meth. A* 759 (2014) 23-28.
- [46] M. Shao et al., Extensive particle identification with TPC and TOF at the STAR experiment, *Nucl. Instrum. Meth. A* 558 (2006) 419-429
- [47] E.G. Judd et al., The evolution of the STAR Trigger System, *Nucl. Instrum. Meth. A* 902 (2018) 228-237.
- [48] PP2PP experiment website <https://www.racf.bnl.gov/Facility/pp2pp/>
- [49] S. Bültmann, W. Chen, I.H. Chiang, R.E. Chrien, A. Drees et al., The PP2PP experiment at RHIC: silicon detectors installed in Roman Pots for forward proton detection close to the beam, *Nucl. Instrum. Meth. A* 535 (2004) 415–420.

- [50] STAR Collaboration, J. Adam et al., Results on Total and Elastic Cross Sections in Proton-Proton Collisions at $\sqrt{s} = 200$ GeV, *Phys. Lett. B* **808** (2020) 135663, arXiv:2003.12136 [hep-ex].
- [51] STAR Collaboration, M. Abdallah et al., Results on Elastic Cross Sections in Proton-Proton Collisions at $\sqrt{s} = 510$ GeV with the STAR Detector at RHIC, *Phys. Lett. B* **852** (2024) 138601, arXiv:2309.16622 [hep-ex].
- [52] STAR Collaboration, J. Adam et al., Measurement of the central exclusive production of charged particle pairs in proton-proton collisions at $\sqrt{s} = 200$ GeV with the STAR detector at RHIC, *JHEP* **07** (2020) 178, arXiv:2004.11078 [hep-ex].
- [53] R. Sikora, *Study of elastic proton-proton scattering with the STAR detector at RHIC*, MSc Thesis: AGH-UST, Krakow, 2014.
- [54] L. Fulek, *Charged particle production in diffractive proton-proton scattering at the RHIC and LHC energies*, PhD Thesis: AGH-UST, Krakow, 2020.
- [55] R. Sikora, *Measurement of the diffractive central exclusive production in the STAR experiment at RHIC and the ATLAS experiment at LHC*, PhD Thesis: AGH-UST, Kraków, 2020.
- [56] H. Bichsel, A method to improve tracking and particle identification in TPCs and silicon detectors, *Nucl. Instrum. Meth. A* **562** (2006) 154.